Synchrotron radiation spectroscopy studies of the initial interaction of Chromium and Cobalt with the surface of Titanium Dioxide

Von der Fakultät für Mathematik, Naturwissenschaften und Informatik

der Brandenburgischen Technischen Universität Cottbus

zur Erlangung des akademischen Grades eines

Doktors der Naturwissenschaften
(Dr. rer. nat.)

genehmigte Dissertation

vorgelegt von

Dipl.-Phys.

Sebastian Müller

geboren am 02. August 1980 in Altdöbern

Gutachter: Prof. Dr. rer. nat. habil. Dieter Schmeißer

Gutachter: Prof. Dr. rer. nat. habil. Christian Pettenkofer

Gutachter: Prof. Dr. rer. nat. habil. Andreas Klein

Tag der mündlichen Prüfung: 25. Februar 2010

Abstract

In the framework of this thesis, synchrotron radiation based spectroscopy methods are applied to study the electronic structures of stoichiometric Rutile single crystals and TiO_2 thin films, and the initial stage of chromium and cobalt growth on TiO_2 thin films.
Resonance photoemission spectroscopy of clean TiO_2 at the Ti $L_{2,3}$ edges led to Auger-like features, with kinetic energies corresponding to the Ti $L_{2,3}M_{4,5}M_{4,5}$ Auger decay channels. The presence of these features is assigned to origin from a $d^2\underline{L}^2$ charge transfer state. The resonance of the Ti $L_3M_{2,3}V$ Auger channel at the Ti L_2 edge is assigned to the L_2L_3V Coster-Kronig Auger, followed by the normal $L_3M_{2,3}V$ Auger decay.
The deposition of chromium on the TiO_2 film causes a strong interaction at the interface, in which TiO_{2-x} is formed together with chromium in the Cr^{3+} state. Besides the oxidized component, contribution of metallic chromium is found as well. In the ultra-low coverage regime, post-deposition oxidation is observed, in which metallic chromium is oxidized to Cr_2O_3, accompanied by re-oxidation of the substrate to TiO_2. The interface reaction is also reflected by the appearance of two defect states in the band gap. Resonant photoemission at the Cr 2p and Ti 2p edges shows well distinguishable Cr 3d respectively Ti 3d character of the respective states. Indications for self-cleaning properties are found by removal of surface carbon during storage in UHV, but the influence of chromium on these properties is not studied in detail.
The interaction between cobalt and TiO_2 is weaker than that of chromium and TiO_2. Nevertheless, an interface reaction is found, in which some of the deposited cobalt is oxidized, while the oxide support is partly reduced. The particular oxidation state of Cobalt is identified by means of multiplet calculation including charge transfer and crystal field effects. The calculated XAS and XPS spectra indicate Co^{2+} in a tetrahedral coordination with four oxygen atoms. The metallic component of cobalt gives rise to a broad resonance in the valence band down to -20 eV, with a pronounced satellite feature that reflects the oxidized component.

Zusammenfassung

Im Rahmen der vorliegenden Arbeit wurde Synchrotron-Strahlung zur spektroskopischen Charakterisierung von stöchiometrischen Rutil-Einkristallen und dünnen TiO_2-Filmen, sowie der Untersuchung der Anfangsphasen des Wachstums von Chrom und Cobalt auf der Oberfläche von dünnen TiO_2-Filmen, eingesetzt.
Resonante Photoemission am sauberen Einkristall und am TiO_2 Film zeigt Auger-ähnliche Emissionen an der Ti 2p Kante, deren kinetische Energien denen eines Ti $L_{2,3}M_{4,5}M_{4,5}$ Auger-Zerfallskanals entsprechen, was auf die Existenz des $d^2\underline{L}^2$ Ladungstransferzustandes zurückgeführt wird. Die Resonanz des Ti $L_3M_{2,3}V$ Auger-Kanals an der Ti L_2-Kante läßt auf einen L_2L_3V Coster-Kronig Auger-Kanal schließen, der vom normalen $L_3M_{2,3}V$ Auger gefolgt wird.
Das Abscheiden von Chrom auf dem TiO_2-Film führt zu einer Redox-Reaktion an der Grenzfläche, wobei TiO_{2-x} durch Oxidation von Cr^0 zu Cr^{3+} gebildet wird. Daneben tritt metallisches Chrom an der Oberfläche auf. In der Anfangsphase wird bei ultradünnen Bedeckungen eine weitergehende Oxidation der metallischen Komponente zu Cr_2O_3 beobachtet, die von einer Re-Oxidation des Substrates zu TiO_2 begleitet wird. Die Reaktion an der Grenzfläche lässt sich auch im Valenzbandbereich verfolgen, wobei zwei Defektzustände in der Bandlücke auftreten. Resonante Photoemission an den Cr 2p und Ti 2p Kanten zeigt, dass beide Zustände einen voneinander unterscheidbaren Charakter als Cr 3d bzw. Ti 3d-artig aufweisen. Weiterhin gibt es Hinweise auf die Fähigkeit zur Selbstreinigung, was sich durch Verringerung der Oberflächenkontamination mit Kohlenstoff äußert, jedoch wurde der Einfluss des abgeschiedenen Chroms auf diese Eigenschaften nicht eingehend untersucht.
Die Wechselwirkung zwischen Cobalt und TiO_2 ist weniger stark als zwischen Chrom und TiO_2. Dennoch wurde eine oxidierte Cobalt-Komponente neben der metallischen Komponente nachgewiesen, wobei der Oxidationszustand des Cobalt mittels Multiplett-Rechnung, die Ladungstransfer- und Ligandenfeldeffekte berücksichtigt, identifiziert wird. Die berechneten XAS und XPS-Spektren weisen dabei auf Co^{2+} in einer tetraedrischen Koordinierung mit vier Sauerstoffatomen hin. Die metallische Cobalt-Komponente führt zu einer breiten Resonanz am Valenzband, die sich bis etwa -20 eV erstreckt, wobei ein deutlicher Satellit die oxidierte Komponente widerspiegelt.

Contents

Chapter 1

Introduction and motivation

Titanium dioxide attracts a lot of interest for many reasons. On one side, its nominal d^0 configuration makes it an excellent model compound [1] for theoretical and experimental studies of electronic structure without "disturbing" d-electrons. As an example, atomic multiplet calculations including crystal field and charge transfer effects of titanium dioxide and related compounds, such as strontium titanate ($SrTiO_3$), have proven as excellent approach to understand the influences of the local coordination geometry on the complex fine structures and satellites of x-ray absorption spectra of the 3d transition metals [2].
It has also turned out that TiO_2 is a well-suited material for photoemission experiments, as the bulk can be easily reduced, and thus a single crystal shows sufficient conductivity to avoid charging effects in electron spectroscopy. The stoichiometry of the surface can be restored by annealing procedures in an oxidizing atmosphere.
Besides the fundamental research, titanium dioxide is also of great interest due to its unique properties that offer a wide range of applications. On one side, TiO_2 is used in everyday applications such as white pigment or sun protection. On the other side, it is also used as a heterogeneous catalyst in Fischer-Tropsch synthesis [3], and it is also known to have sensoric activity e.g. as sensor for oxygen [4]. In dye sensitized solar cells, also known as Grätzel cells [1, Ref. 29], porous TiO_2 is applied as well.
These applications have one thing in common, that is, the promising properties are not realized by pure TiO_2 alone. The properties are result of complex interaction between the TiO_2 as an oxide support material and an adsorbate, which can be a metal, an oxide, or complex organic molecules.
Pure TiO_2 is also of interest, as it can be used for the fabrication of self-cleaning walls, which is directly connected to the decomposition of organic molecules [5], and it also has a promising ability for the decomposition of water into O_2 and H_2 [6].
Throughout this thesis, the interest is especially on the interaction between the oxide and a metallic overlayer, as it is the case for example in the TiO_2 based catalysts. The metal-TiO_2 compound can be applied to realize properties that cannot be achieved by the

constituents alone. For example, gold can be catalytically activated when it is deposited on TiO_2, where it forms small clusters. In contrast to this, bulk-like gold is inert and does not show catalytic activity [7, 8].
The interaction between chromium and TiO_2 is of interest, as chromium is highly reactive towards oxygen, and thus tends to wetting the substrate rather than forming small clusters as it is the case for non-reactive metals [9].
The system Co-TiO_2 is applied in Fischer-Tropsch synthesis, thus it is desirable to understand the detailed interactions at the interface that turn cobalt into the active material. It is somewhat striking that TiO_2 supported cobalt has not drawn as much interest as TiO_2 supported chromium did. Thus, it is one of the main scopes of this thesis, to study the initial interaction between cobalt and titanium dioxide in the sub-monolayer regime. The initial growth steps of chromium and cobalt on titanium dioxide films are investigated. In contrast to earlier studies of metal growth on well defined, single crystalline TiO_2 surfaces, an alternative approach is chosen. The choice of a TiO_2 thin film rather than a single crystal, is a step towards the so-called material gap, which describes the gap between fundamental research on well-defined materials on one side, and the application, for which easy to handle materials under more realistic conditions are desirable.
The materials that are of interest throughout this thesis will be briefly introduced in Chapter 2. The introduction will focus on bulk and surface structures of the Rutile and Anatase polymorphs of TiO_2, as well as a brief introduction of the different models of the electronic structures, and the application of these models in case of the CTM calculations. In Section 2.4, a summary of the literature on the interaction between chromium respectively cobalt with single crystalline TiO_2 surfaces will be given. This is followed by a description of the experimental setup in Chapter 3, which includes also the fundamental aspects of photoemission spectroscopy, x-ray absorption spectroscopy and resonant photoemission, and the realization of the experiments at the storage ring. Additionally, the charge transfer calculations are introduced together with some advanced aspects of XAS, including the effects of crystal fields. The preparation of the Rutile single crystal, the TiO_2 film, and the evaporation of chromium and cobalt are described in Chapter 4. In Chapter 5, the results from the experiment as well as from the theory with the CTM program, will be described in detail. The discussion of the results then follows in Chapter 6.

Chapter 2

The materials

In this chapter, the relevant materials, TiO_2 as Rutile and Anatase polymorphs, chromium and its oxides, and cobalt and its oxides will be briefly introduced. The focus will be on the description of electronic and geometric properties of TiO_2, as well as on the coordination geometries in the oxides of chromium and cobalt. This also serves as an introduction into the basics of the CTM calculations. The images of the crystal structures shown in this chapter are created with the Mercury software [10, 11, 12].

2.1 Titanium Dioxide

Titanium dioxide exhibits numerous polymorphs, of which only Anatase and Rutile are of significant importance for research and application. Besides these two, Brookite should additionally be mentioned. In these polymorphs, the crystal is built from more or less distorted $[TiO_6]$ octahedra that are connected to each other. The titanium atoms are 6-fold coordinated, while the oxygen atoms are 3-fold coordinated. The 3+ oxidation state of titanium is also known, but its stability is lower than that of the 4+ state. Besides the oxides Ti_2O_3 and TiO_2, there exist the so called Magnéli phases [13] of the composition Ti_nO_{2n-1}, with stoichiometry between Ti_2O_3 and TiO_2. The existence and stability of these phases give rise to the reducibility of TiO_2.
In the following parts, the focus will be on the bulk and surface properties of Rutile and Anatase, the bulk structures will be introduced and the most important surfaces of both polymorphs will be described. As surface relaxations and reconstructions are not in the focus of this thesis, they will be briefly mentioned only.

2.1.1 Rutile

Rutile is the thermodynamically most stable polymorph of TiO_2. The other polymorphs undergo an irreversible phase transition to Rutile at elevated temperatures between 700°C and 1000°C [14]. The basic element of the geometric structure is the slightly distorted

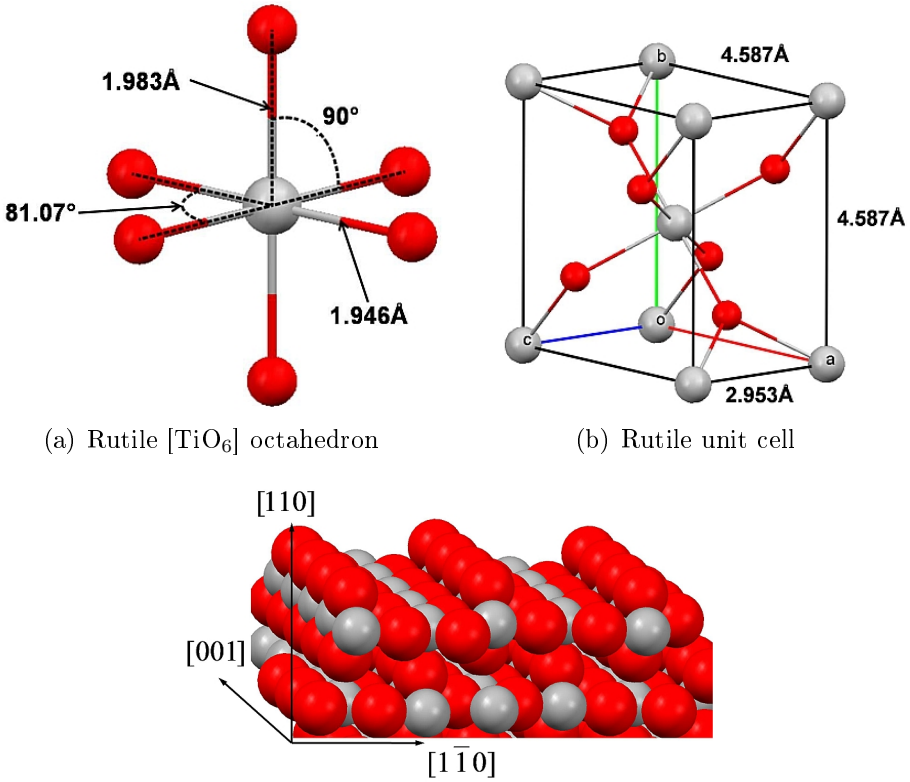

(a) Rutile [TiO_6] octahedron

(b) Rutile unit cell

(c) The unreconstructed Rutile (110) surface

Figure 2.1: Ball and stick models of the basic [TiO_6] octahedron (a) and the tetragonal unit cell (b) of Rutile, with a = b = 4.587 Å, c = 2.953 Å. In the model of the unreconstructed (110) surface (c), the typical rows of bridging oxygen along the [001] direction are clearly visible. (Crystallographic data is taken from [1, Sec. 2.1])

[TiO_6] octahedron, which is shown in Fig. 2.1(a) (red = oxygen, grey = titanium). It has to be pointed out that the coordination octahedron and the relation to Ti 3d orbitals are described with respect to Cartesian x, y, and z-coordinates, while the bulk crystal structure is described in terms of the a, b, and c axes. The ligands in the equatorial x-y-plane do not form a square, as it would be the case in a regular octahedron. The O–Ti–O angles in this plane are not 90° but 98.93° respectively 81.07°, while the bond lengths are equal with a Ti–O distance of 1.946 Å. The two bonds along the z-axis, corresponding to the direction of the $3d_{z^2}$ orbital, are longer with 1.983 Å.

The tetragonal unit cell of Rutile is shown in Fig. 2.1(b) as a ball and stick model with the [TiO_6] octahedron in the center. This representation also shows that the z-axis of the [TiO_6] octahedron is not parallel to any of the crystal main axes. The cell parameters are a = b = 4.587 Å, c = 2.953 Å. In the bulk crystal, the octahedra have alternating orientation along the [110] direction i.e. alternating orientation of the long bond. Every oxygen has a long Ti–O bond in one octahedron and in the same time to shorter Ti–O bonds to two adjacent octahedra.

The formation of the most stable (110) surface can be understood as a bulk truncation. In

this surface orientation, the tetragonal unit cell is tilted by 45° with respect to the surface, in such a way that the a and b axes include an angle of 45° with the surface normal. The long Ti–O bonds are alternating in-plane and out-of-plane. In this model, every out-of-plane long bond is cut, resulting in the clearly visible oxygen bridges along the [001] direction on the (110) surface (Fig. 2.1(c)). The opposing surface has the same properties, as the long Ti–O bonds of the "upper" half are cut, and the respective oxygen is part of the bridging row of the "lower" half, and vice versa. The titanium atoms underneath the oxygen rows in [001] direction are 6-fold coordinated, as it is the case in the bulk material, while the titanium atoms underneath the missing oxygen rows are 5-fold coordinated with a dangling bond in the direction of the long Ti–O. Corresponding to this, there are bulk-like oxygen atoms that are 3-fold coordinated, while the bridging oxygen atoms along the [001] direction are only 2-fold coordinated, due to the broken bond towards the missing titanium atom.

On the relaxed surfaces, the bridging oxygen atoms move downward to the bulk, while the 6-fold coordinated titanium atoms move upwards. In contrast to this, the 5-fold titanium atoms move downwards while the 3-fold coordinated in-plane oxygen atoms move upwards. The displacement is in the range of 0.1 Å, and can be quantified by means of SXRD measurements, as shown by Charlton et al. in [15]. The under-coordinated oxygen atoms can be easily removed during annealing procedure, which gives rise to point defects [1].

In order to prepare such a crystal for electron spectroscopy, which basically means that a stoichiometric surface is prepared on a crystal that is (semi)-conducting due to high concentration of defects. The bulk-reduction can be easily achieved by various treatment in reducing UHV conditions, such as electron bombardment, sputtering [16] or heating [17, 18, 19]. During such treatments, oxygen vacancies are created, and the bulk material becomes n-doped [1, Fig. 35], and consequently conductive enough to prevent charging effects in PES experiments. Subsequently, the stoichiometry of the surface is restored by annealing in oxidizing conditions, which is realized by applying oxygen pressures from 10^{-7} mbar [1, 20] to around 10^{-6} mbar [21].

For this thesis, oxidizing conditions are of interest, as there is only one annealing step in ambient air providing oxidizing conditions. Henderson also described the bulk-assisted re-oxidation [22, 23], which restores a stoichiometric surface without exposure to additional oxygen, by depletion of titanium in the surface region due to its diffusion into the bulk.

2.1.2 Anatase

Anatase is one metastable polymorph of TiO_2, which shows an exothermic phase transition to Rutile. For the transition temperature, values from around 670 K to above 1400 K are reported [24]. The particular transition temperatures and rates depend on various

factors, such as crystal sizes, specific surface area, or impurities [25].

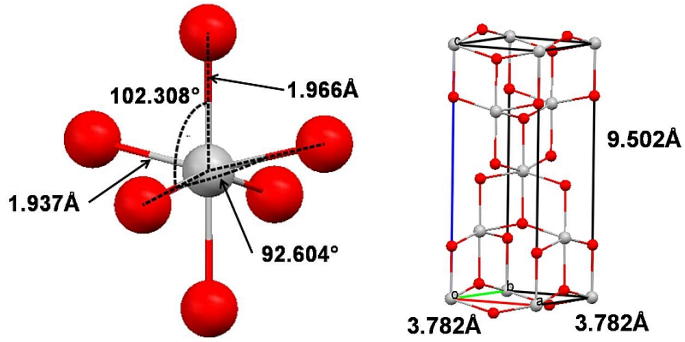

(a) Anatase [TiO_6] octahedron (b) Anatase unit cell

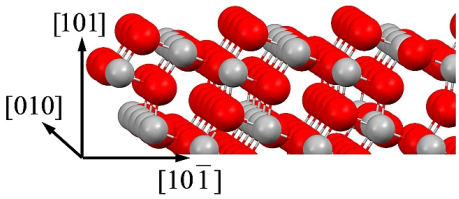

(c) The unreconstructed Anatase (101) surface

Figure 2.2: Ball and stick models of the basic [TiO_6] octahedron (a) and the tetragonal unit cell (b) of Anatase, with a = b = 3.782 Å, c = 9.502 Å. In the model of the unreconstructed (101) surface, the typical rows of 2-fold coordinated oxygen along the [010] direction and its zig-zag structure along the [10$\bar{1}$] direction are clearly visible. (Crystallographic data is taken from [1, Sec. 2.1], respectively from [26])

The basic [TiO_6] octahedron of Anatase is shown in Fig. 2.2(a). The distortion from octahedral symmetry is stronger than in Rutile. The first effect is again elongation in the z-direction, where the bond lengths are 1.966 Å, while the four shorter bonds have a length of 1.937 Å. In contrast to the [TiO_6] octahedron of Rutile (Fig. 2.1(a)), the four oxygen atoms with shorter bonds are not located in the equatorial x-y-plane, but two opposing oxygen atoms are shifted above the equatorial plane, while the other two are shifted below this plane. This results in O–Ti–O angles of 102.308° between the short and long bond, respectively 92.604° between two short bonds. Anatase has a tetragonal unit cell as well, it is shown in Fig. 2.2(b). The lattice parameters are a = b = 3.782 Å, c = 9.502 Å.

From the application point of view, Anatase is the more promising polymorph, as the activity is higher than in case of Rutile [27, 28, 29], for example in case of catalysis, photo-catalysis and dye-sensitized solar cells. In contrast to the well characterized Rutile surfaces, such detailed studies on Anatase surfaces are difficult, as the growth of large Anatase single crystals is connected with several problems. However, first principle studies on in-situ grown Anatase samples have been carried out. This is achieved by e.g. growing an epitaxial layer of TiO_2 on the (101) face of an equilibrium-shaped natural crystal [30].

This epitaxial layer is necessary in order to get rid of the impurities from the natural crystal.
The most stable Anatase surface is the (101) surface [1, 28, 31], which is shown as a ball and stick model in Fig. 2.2(c). The typical features of this surface are the rows of 2-fold coordinated oxygen atoms along the [010] direction, which results in a zig-zag structure along the $[10\bar{1}]$ direction. As in case of Rutile, the under-coordinated oxygen rows give rise to reconstructions and defect formation on the surface.
Calculations of the surface energies indicate that an Anatase crystal in equilibrium shape (shown in [28, Fig. 2], using a Wulff construction with the calculated surface energies) has a lower total surface energy than a Rutile crystal in equilibrium shape. This gives rise to the higher stability of small Anatase crystallites in comparison to the corresponding Rutile crystallites. Thus, a large surface-to-bulk ratio stabilizes the Anatase structure [32, 33].

2.1.3 Electronic structure of titanium dioxide

In a zero order approach, the electronic structure of TiO_2 can be described from the ionic point of view. According to this, the valence configuration is O $2p^6$ Ti $3d^0 4s^0$, leading to a pure O 2p derived valence band and a pure Ti 3d and 4s derived conduction band [34]. In combination with the crystal field theory, where the anions are treated as point charges that are coordinating the cation, basic conclusions on structures, energy states and electronic configuration, can be drawn. In the frame work of the CTM calculations, this model is realized by the nominal configuration of the transition metal ion, while the strength of the crystal field is represented by the parameter of 10 Dq in case of an O_h field.
In the more advanced cluster models, the $[TiO_6]$ octahedron is used to derive molecular orbitals. In this model, significant covalent admixture of the metal 3d, 4s and 4p states to the O 2p character of the bonding molecular orbitals is considered. Corresponding to this, the O 2p orbitals contribute to the anti-bonding orbitals that have mainly metal 3d, 4s and 4p character. When this molecular approach is extended to a band model, the admixture of the metal states to the valence band remains. In principle, the CTM calculations are capable to use the ionic picture (point charges, electrostatic interaction, no charge transfer) as well as the cluster model for one single cluster, where covalent contributions to the bonding and non-bonding states can be considered, although the CTM program is not capable to treat the metal 4s and 4p states.
Density functional theory is used for the calculation of electronic structures of surfaces, as well as the adsorption of molecules or clusters on such surfaces. Additionally, the calculation of the partial density of states (pDOS) also indicates covalent admixture of the metal states to the valence band, which can be experimentally probed by resonant

photoemission of the valence band at the Ti 2p edge.
The covalent bonding character causes discrepancy between the formal oxidation states (Ti^{4+} and O^{2-}) and the average charges of $Ti^{1.7+}$ and $O^{0.85-}$ [35].
Experimental studies of the band structure have been carried out by Hardman et al. [36]. In agreement with the theory, flat bands without significant dispersion are found, which indicates localized electrons.
On a slightly reduced surface, oxygen atoms from the bridging rows are missing, of which each leaves two electrons. These electrons are distributed in Ti 3d states, resulting in a d^1 configuration [1], which gives rise to the observation of a band gap state in photoelectron spectroscopy. The gap state can be quenched by exposure to O_2, which dissociates at the surface and fills the vacancies [37].

2.2 Chromium and chromium oxides

Chromium belongs to the group of the 3d transition metals. It crystallizes in body-centred cubic structure. Similar to several other metals, such as aluminium or titanium, chromium forms a protective oxide layer in air, which prevents the oxidation of the material underneath this layer. The atomic configuration is $3d^54s^1$, which means that in comparison with the neighbours vanadium ($3d^34s^2$) on the left side and manganese ($3d^54s^2$) on the right side, one 4s electron is shifted into a 3d orbital leading to a more stable half filled 3d subshell [13, Sec. 4] with a high spin state. Chromium also shows remarkable ability of heterogeneous catalysis [13], which is one of the driving factors to study its interaction with a TiO_2 surface.
The oxidation states Cr^+ to Cr^{6+} are known, although the 1+, 4+ and 5+ states are rare. The most stable oxidation state is Cr^{3+}, which forms green compounds such as the oxide or chloride. The compound Cr_2O_3 crystallizes in trigonal corundum structure, with lattice parameters a = 4.961 Å, c = 13.597 Å and $\gamma = 120°$ [38].
The reason for the high stability of the Cr^{3+} state is the half-filled t_{2g} derived subshell in O_h symmetry, leading to high crystal field stabilization energy [39, Ch. 14]. This is also valid for slight distortions from O_h symmetry, in which the degeneracy of the t_{2g} subshell is partly removed.
In Fig. 2.3(a), the basic [CrO_6] octahedron of Cr_2O_3 is shown. It is clearly visible that it exhibits significant distortion from O_h symmetry with three long bonds (2.016 Å) and three short bonds (1.965 Å). The angles between two opposing oxygen ions to the central Cr^{3+} (e.g. the angles O_1–Cr–O_6) are always 167.06°. Besides this, there are four different O–Cr–O angles. The value of 81.42° applies for O_2–Cr–O_4, O_2–Cr–O_6 and O_4–Cr–O_6. The angles between O_1–Cr–O_4, O_2–Cr–O_3 and O_5–Cr–O_6 are 86.91°. Between O_1–Cr–O_2, O_3–Cr–O_6 and O_4–Cr–O_5 there is an angle of 91.37°. The angle of 98.99° occurs between

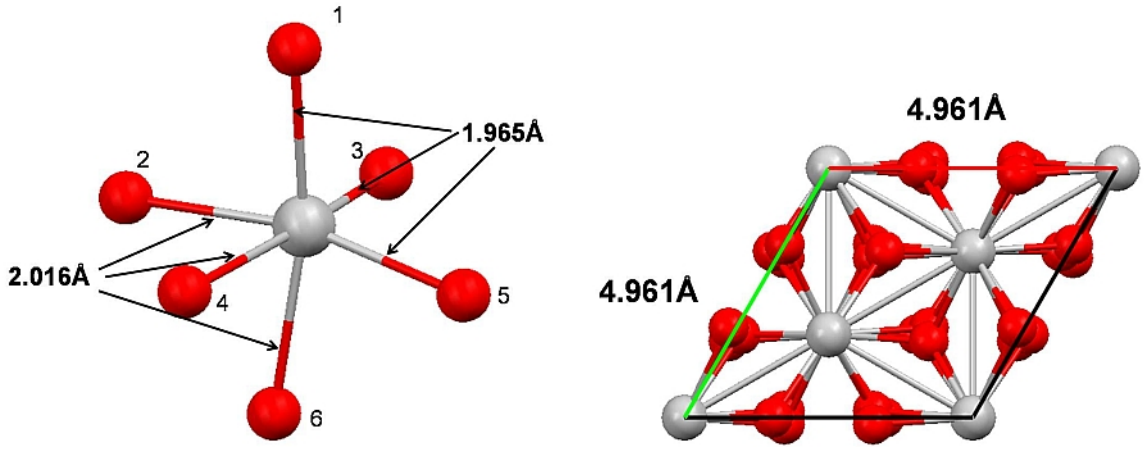

(a) The basic CrO_6 octahedron of Cr_2O_3

(b) The trigonal Cr_2O_3 unit cell with view along the c-axis

Figure 2.3: Ball and stick models of the basic $[CrO_6]$ octahedron in Cr_2O_3(a), and the trigonal unit cell with a = 4.961 Å and c = 13.597 Å in (b). The view is along the c-axis. (Crystal structure data from [38])

O_1–Cr–O_3, O_1–Cr–O_5 and O_3–Cr–O_5. In the bulk structure of Cr_2O_3, the O^{2-} ions form a hexagonal close-packed sublattice with Cr^{3+} ions filling 2/3 of the octahedral interstitial sites. The representation of the unit cell is shown in Fig. 2.3(b).
The second stable oxidation state is 6+, which is present in the yellow chromates ($[CrO_4]^{2-}$) and orange dichromates ($[Cr_2O_7]^{2-}$), which both are strong oxidizing agents. The corresponding acids have the hypothetical structures H_2CrO_4 respectively $H_2Cr_2O_7$, but only the anions exist in nature.
The 4+ state is of interest for the application of CrO_2, which is a half-metallic ferromagnet [40, 41]. It crystallizes in rutile structure with lattice parameters a = b = 4.421 Å and c = 2.917 Å [42]. The small mismatch allows epitaxial growth on Rutile–TiO_2 [40]. CrO_2 is not stable in ambient conditions i.e. a Cr_2O_3 layer is formed on top of the surface [40]. The importance of this material has significantly declined since optical data storage media were widely introduced to the consumer's market. However, this material may be of interest in future for spintronics application.
The other oxidation states of chromium are of low relevance as they are only stable under extreme conditions. Thus, they will not be further described in detail.

2.3 Cobalt and cobalt oxides

Cobalt belongs to the late transition metals, with a more than half-filled 3d subshell with the ground state configuration $3d^74s^2$. The ferromagnetic metal crystallizes in hcp lattice, with a transition to fcc at temperatures above 420°C [13, Sec. 4]. This transition is not sharp, but random intergrowth of both components occurs. The possible oxidation states

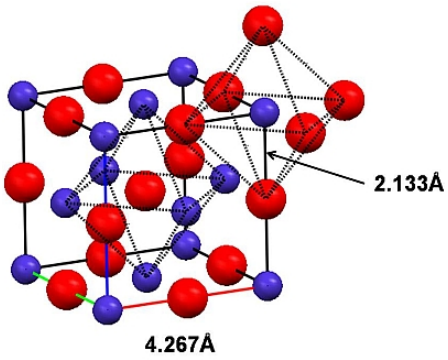

(a) The cubic unit cell of CoO

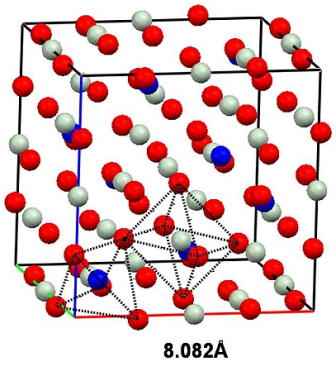

(b) The cubic unit cell of Co_3O_4

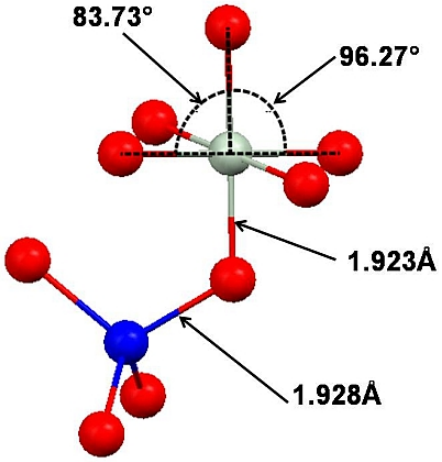

(c) Two adjacent 4-fold and 6-fold coordination polyhedra

Figure 2.4: Models of the unit cells of CoO (a) with the regular [CoO_6] octahedron emphasized, and Co_3O_4 with a tetrahedron of 4-fold coordinated Co^{2+} and the octahedron of 6-fold coordinated Co^{3+} (red = oxygen, grey = Co^{3+}, blue = Co^{2+}). For better visibility, two adjacent polyhedra of Co_3O_4 are shown in (c). (Crystal structure data of Co_3O_4 is from [43], the data of CoO is taken from [26])

of cobalt range from Co^{2+} to Co^{4+}.

The oxide CoO crystallizes in the rock-salt structure with cubic symmetry, where the O^{2-} sublattice has fcc (or ccp) structure and Co^{2+} fills the octahedral sites; see Fig. 2.4(a) for a model of the unit cell. For symmetry reasons, this can be described vice versa as well. The lattice parameter is 4.267 Å [26]. In this structure, the Co^{2+} ions are 6-fold coordinated by O^{2-} forming a regular octahedron. The same symmetry is found for O^{2-}. The two coordination octahedra are emphasized in Fig. 2.4(a).

In the mixed valency oxide Co_3O_4 with spinel structure, Co^{2+} is 4-fold coordinated in T_d symmetry and Co^{3+} is 6-fold coordinated with O_h symmetry. In this compound, O^{2-} ions form hcp structure, with the Co^{2+} ions filling 1/8 of the tetrahedral interstitial sites, and Co^{3+} filling 1/2 of the octahedral interstitial sites. The cubic unit cell of Co_3O_4

with lattice parameter of 8.082 Å is shown in Fig. 2.4(b). In Fig. 2.4(c), two adjacent coordination polyhedra are shown. While the $[Co^{(2+)}O_4]$ tetrahedron is regular with O–O distance of 3.148 Å and Co–O bond length of 1.928 Å, the $[Co^{(3+)}O_6]$ octahedron is distorted from regular O_h symmetry. The Co–O bond lengths are 1.923 Å, with two different O–Co–O angles. If two opposing oxygen atoms are considered to be located on the z-axis, forming O_z–Co–O_z chain, the two other $O_{x,y}$–Co–$O_{x,y}$ chains are tilted with respect to this z-axis, resulting in an $O_{x,y}$–Co–O_z angle of 83.73°. (Crystal structure data from [43]).
The pure three-valent cobalt oxide Co_2O_3 has to be considered as well, although this state alone is not as stable as Co^{2+} and the mixed valence compounds. Nevertheless, the Co^{3+} state is of significant importance in lithium ion batteries, where the anode is composed of an intercalation compound $Li_xCo_{1-x}O_2$. During charging, the Co^{3+} is oxidized to Co^{4+}, while Li is removed from the anode. Overcharging then finally leads to synthesis of CoO_2. The additional focus of interest is the usefulness of cobalt in heterogeneous catalysis, as already mentioned in the introduction.

2.4 Metal growth on titanium dioxide surfaces

The well characterized Rutile (110) surface has been used as a substrate for numerous metal overlayer growth experiments to study properties of the interactions at metal/metal-oxide interfaces. An overview on such experiments is found in [1, Section 4] and [44, Table 1], where the interaction of a wide range of metals with the TiO_2 surface is summarized.
As described by C.T. Campbell [45, Section 3], the reactivity respectively the affinity for oxygen of the deposited metal A in comparison to the metal B in the oxide BO respectively B_xO_y has a crucial influence on the character of the interaction. From thermodynamic considerations, the reaction

$$A(s) + BO(s) \rightarrow AO(s) + B(s)$$

is favourable if the oxide AO is more stable than the oxide BO i.e. its standard enthalpy $\Delta H^0_{f,AO}$ is more negative than $\Delta H^0_{f,BO}$ of oxide BO. In case of more complex formula, like in dioxides, a partial reaction like

$$2BO_2(s) \rightarrow B_2O_3(s) + \frac{1}{2}O_2(g)$$

has to be considered as well. This implies that if the oxide of metal A is more stable than the oxide of metal B, a reaction at the interface will occur. This is only valid for the bulk materials, but the standard enthalpies do not include contributions from the surface

energies.
More complex reactions, like formation of ternary compounds or intercalation of the deposited metal into the oxide can also take place.
Across the periodic table, a clear trend is visible. The reactive metals on the left side, like from the lithium and magnesium groups as well as the early transition metals, show a pronounced interaction at the interface. Growth studies have been carried out with highly reactive metals, like potassium [46], caesium [47], calcium [48] or barium [49]. Although the position of aluminium is on the right side of the periodic table, the reactivity is comparable to the metals from the left side, like magnesium. This has also been shown in growth studies in [19]. These metals grow at first in an oxidized form, accompanied by reduction of Ti^{4+} to Ti^{3+}. In case of molybdenum deposition on Rutile (110), the Ti^{2+} state is reported as well [50]. Corresponding to the reduction of Ti^{4+} to lower oxidation states, the deposited reactive metal becomes oxidized. Depending on the particular reaction, the growth mode is two-dimensional layer-by-layer growth (van-der-Merwe), or quasi-two-dimensional (Stranski-Krastanov).
In contrast to this, the late and more inert transition metals like gold [8], palladium [51] or platinum [52] do not show a reaction at the interface. Corresponding to this, cluster growth (Volmer-Weber) is observed for these metals.
The strength of the reaction gradually decreases with a line connecting rhenium, ruthenium, and cobalt marking the border between interface reaction and growth without reaction. Additionally, numerous theoretical studies on metal growth on TiO_2 are carried out as well. Asaduzzaman et al. [53] focus on the growth of 3d transition metals on Rutile (110). According to the authors, the stable adsorption site for most of the ad-atoms is the case in which it bonds to one 3-fold and two 2-fold coordinated oxygen atoms. This does not apply for the case of chromium growth, but this will be further explained in the following section.

2.4.1 Chromium growth on titanium dioxide

Detailed studies of chromium growth on titanium dioxide have been carried out by the Diebold group [9, 44, 54] with various methods, including spectroscopic tools as such XPS and UPS, imaging methods such as LEED, and STM, and others such as LEIS. These studies already revealed some of the complex interactions that occur at the Cr-TiO_2 interface. Core level XPS at Ti 2p and Cr 2p [9, Fig. 4] show the reduction of Ti^{4+} to Ti^{3+} and the occurrence of chromium in the Cr^{3+} state. For layer thickness above 2 Å of chromium, a component with a binding energy below that of Ti^{3+} is found in the Ti 2p spectrum, which is assigned to Ti^{2+}, although this assignment is connected with some uncertainty. Up to an overlayer thickness of 7 Å, no metallic component Ti^0 is found. The Cr 2p spectra of thickness below 4 Å only show an oxidized component, with a binding energy

difference to the Cr metal reference of 1.7 eV.
In these studies, the influence of the reactivity of the deposited metal on the growth mode was investigated as well. In the order copper, iron, chromium, hafnium, the reactivity increases together with the tendency of overlayer spreading across the surface. Copper forms three-dimensional clusters, iron forms flat islands, chromium forms quasi-two-dimensional islands, and hafnium forms a closed two-dimensional overlayer.
Using a Rutile surface in which the ^{16}O was replaced by labelled oxygen ^{18}O, it was shown that the reaction at the interface is more complex than a simple charge transfer from chromium to titanium. The authors assigned the ^{18}O LEIS signal found in the chromium overlayer to oxygen, which is incorporated in the growing chromium layer due to a dynamic atom exchange process. Detailed analysis of the LEIS data indicate that chromium only grows in quasi-two-dimensional mode in the initial stage, up to a total surface coverage of around 80%. Subsequently, the growth of three-dimensional chromium clusters on top of the oxidized islands starts.
In the work of Christian Winde [55], the focus was in particular on this initial stage. The main tool was high resolution TEM-EELS together with Auger electron spectroscopy. Additionally, high resolution STM and STS were applied. The STM studies revealed that chromium at first bonds on top of the five-fold coordinated titanium atoms in between the oxygen rows in [001] direction. The incorporation of bridging oxygen atoms into the forming oxidized chromium overlayer was shown as well. It was found that the oxidized chromium layer is not completely closed, in agreement with the LEIS studies by the Diebold group. The growth of metallic chromium starts on top of the oxidized islands. The LEED studies performed in this work indicated that a defined crystallographic orientation between the substrate and the overlayer exists. The defect-rich interface was studied by TEM-EELS, where an interface layer with a thickness of around 20 Å was found. This layer is dominated by structural defects, but it is not completely amorphous. This indicates that it is not justified to speak of THE interface, as the chromium and titanium contents vary gradually across the interface. The excellent lateral resolution of the TEM-EELS does not deliver as precise information on oxidation state and local symmetry of the transition metal ions as x-ray absorption spectroscopy at a synchrotron radiation source does, which is a motivation to continue studies on chromium growth on TiO_2.
The studies carried out by Nakajima et al. [56], were done on a Rutile (001) surface rather than on a (110) surface, as it was the case in the previous studies. The Rutile (001) surface is non-polar with a larger number of broken bond in comparison to the low-energy (110) surface. There are only four-fold coordinated titanium atoms respectively two-fold coordinated oxygen atoms [1, Section 2.4].
The valence band photoemission experiments of the Cr-deposited Rutile (001) surface revealed two well separated in-gap emissions that are assigned to the formation of Ti^{3+} (d^1)

and Cr^{3+} (d^3). The character of both in-gap emission was investigated by 3p resonant photoemission at the Ti 3p and Cr 3p edges. The emission intensities of both gap states were measured as a function of the excitation energy i.e. according to the definitions of this thesis, the term CIS spectra should be preferred rather than resonance photoemission. The distinct Ti 3d respectively Cr 3d character is derived from the resonance profile of the CIS spectra, where a typical minimum at around 40 eV is found for Ti 3d, and a minimum at 42 eV for Cr 3d. The small separation of the 3p edges, which is only a few eV in this case, causes difficulties for a direct conclusion, as several cross-talk mechanisms can appear. Additionally, the resonance maxima are also separated by only a few eV.
As it will be shown by means of multiplet calculation in Section 5.2.4, it is not straightforward to derive information on oxidation state and local structure from the 3p x-ray absorption spectra respectively excitation spectra.
Nakajima et al. also showed that higher coverage (2 ML) leads to development of metallic-like chromium on the surface. Upon exposure to 20 L of oxygen (1 L = 10^{-6} torr·s), both in-gap emissions vanish, and a new, Cr_2O_3-like feature appears. The authors concluded that the Cr-deposited TiO_2 (001) surface has a similar ability of adsorbing oxygen like the metallic chromium surface, but the missing Fermi-edge indicated small clusters rather than bulk-like metal.
The theoretical studies of Asaduzzaman et al. [53] indicate that a substitutional site rather than surface adsorption is preferred in case of chromium. The substitutional site is a 6-fold coordinated subsurface titanium atom. This is also true for vanadium and manganese, as they form stable dioxides. These theoretical results are in contrast to the findings of Ch. Winde, where the preferred adsorption site of chromium is in between the oxygen bridging rows on top of the 5-fold coordinated titanium atoms.

2.4.2 Cobalt growth on titanium dioxide

In contrast to chromium growth on TiO_2, there is much less contribution to this field in case of cobalt growth on TiO_2, although this system has high potential as Fischer-Tropsch catalyst. Shao et al. [57] studied the interaction between cobalt respectively cobalt oxide (CoO), with stoichiometric and reduced TiO_2 respectively TiO_{2-x}, in the ML and multi-ML regime, without focussing on the initial steps of growth.
The deposition of 1 ML cobalt causes a reduction of the substrate, as is monitored by the changes in the Ti 2p spectra. The dominating component of cobalt is metallic as derived from the Co 2p core level and from the valence band, where the high DOS of Co 3d is found at the Fermi-energy. Corresponding to the reduction of Ti^{4+} to Ti^{3+}, an oxidized cobalt component is present as well. For very low amount of cobalt deposited on TiO_2, the Co^{2+} oxidation state is concluded by the authors. In comparison to the interaction between chromium and the TiO_2 surface, the interaction between cobalt and TiO_2 is less

intense. In return, this is in excellent agreement with the findings from the Diebold group, where the strength of interaction decreases from chromium via iron to copper, where no interface reaction takes places. According to Diebold [1, p. 114], cobalt represents the border in the series of 3d metals, as iron still shows a reaction with TiO_2, but nickel does not.

Chai et al. [58] performed similar studies with 30 Å cobalt deposited onto Rutile (100) surface. In contrast to cobalt on Rutile (110), the authors found no evidence for an interface reaction at room temperature. The reaction was activated only when the temperature was raised to 400°C and above by the so-called SMSI effect [59, 60]. This effect is observed for the group VIII elements supported on reducible oxides. SMSI can strongly influence the properties of the metal-TiO_2 system, such as gas adsorption or catalytic activity.

In summary, no such detailed knowledge of the initial interaction steps between cobalt and TiO_2 exists in comparison to the properties of the r-TiO_2 system, where even the preferred adsorption sites are could be identified in an experiment.

Chapter 3

Experimental methods

In this Chapter, the experimental details are described, beginning with a brief description of the beamlines U49/2-PGM2 and TGM7 at BESSY II in Berlin. This is followed by description of the applied methods, i.e. PES, XAS, ResPES and CTM, together with the realization of the experimental methods at the beamline.
It is not intended to describe the generation and application of synchrotron radiation in detail. This can be found in literature [61, Section 13.2] or [62]. The focus is on the realization of the experiments instead.

3.1 Experimental Setup

The beamline U49/2–PGM2 is based on an undulator insertion device with a period length of 49.4 mm and 84 periods, equipped with a plane grating monochromator with 1000 lines per mm. The accessible photon energy covers the range from 85 eV to 1890 eV by three odd harmonics (1st, 3rd, and 5th harmonic). Manual switching between the harmonics is not necessary, as this is done by a drive table, which automatically chooses the correct harmonic. The accuracy of the photon energy settings is better than 0.1 eV. The resolution of the photon energy depends on the energy and the exit slit settings. The monochromator control allows remote setting of the exit slit while directly displaying the energy resolution of the beam line. This FWHM value does not include the experimental resolution determined by the analyser settings. Table 3.1 gives an overview on the dependence of the energy resolution from the exit slit settings at some relevant photon energies.

During the experiments in multi-bunch hybrid mode, the exit slit was set to 50 µm, while it was opened to 100 µm in low α mode, which increases the FWHM to roughly two times the values of multi-bunch mode. A possible influence of the adapted electron optics in the storage ring on the energy resolution of the beamline is not included in this assumption. The desired excitation energy is directly selected within the measurement software

Photon energy [eV]	Exit slit setting [µm]	FWHM [meV]
900	50	191
900	20	76.5
565	50	95
565	20	38
450	50	67
450	20	27
150	50	13
150	20	5.2

Table 3.1: Overview of the resolution at selected excitation energies depending on the exit slit settings. The values only represent the resolution of the beamline.

(SpecsLab 2). This is also done in the measurement of the excitation spectra i.e. x-ray absorption and constant initial state, where scanning of the photon energy is also realized by the connection between measurement computer and beamline computer. This setup allows the reduction to one single data format, and additionally allows parallel measurement of for example CIS spectra and TEY spectra. This is possible due to the connection of an ARM Interface Controller (SPECS ARMIN 10) to the measurement computer. This interface records the signals of up to three analogue channels parallel to the measurement. The analogue signals are fed from two Keithley pico-ampere meters that measure I_0 and TEY. The experiments are carried out at the ASAM system, which is equipped with a SPECS PHOIBOS 150 hemispherical electron energy analyser with a 2D CCD detector. The active area of the channel plates is divided into ten virtual energy channels.
The TGM 7 is a dipole bending magnet beamline with a toroidal grating monochromator. This beamline covers the energy range from 8 eV to 120 eV, which allows ResPES measurements at e.g. the Ti 3p edge. The monochromator control has a different design, which means that manual setting of the excitation energies is necessary.

3.2 Photoelectron spectroscopy

Basically, photoelectron spectroscopy means that a sample is illuminated with monochromatic light, which causes emission of electrons by the photoelectric effect. The monochromatic light can be generated by either gas discharge lamps (UV region), laboratory (soft) x-ray sources (e.g. Mg-K_α or Al-K_α), or by a synchrotron radiation facility, which in principal provides tunable light from the infra-red to the hard x-ray regime.

PES is very surface sensitive due to the low inelastic mean free path of electrons in solid matter. Typically, an information depth in the nm range is achieved.
One advantage of a synchrotron light source, besides the high photon flux, is that it allows switching between more surface and more bulk sensitive measurements. Bulk sensitive measurement is achieved if one chooses a high excitation energy, resulting in high kinetic energy (some 100 eV) of the emitted photoelectrons. Additionally, x-ray absorption and resonant photoemission experiments also require a wide range of possible excitation energies.
Additionally, the possibility of HIKE-XPS should be mentioned as well, which requires laboratory or synchrotron light sources in the hard x-ray regime, and is very bulk-sensitive method in comparison to standard PES in the soft x-ray regime.

3.2.1 Physical background of photoelectron spectroscopy

When the sample is irradiated with light of sufficiently high photon energy, an electron can be excited from a core or valence state into the vacuum, where it can be described as a free electron. Photoemission is a tool to probe the occupied DOS, although final state effects are of importance as well. When a PES spectrum is interpreted as the occupied DOS, it is assumed that the ejection of one electron does not induce changes of the energies of the remaining electrons. This is known as Koopmans' theorem. The kinetic energy of the photoelectron can be measured, and its binding energy is calculated by the following equation:

$$E_{kin} = h\nu + E_{bind} - \Phi$$

where E_{kin} is the kinetic energy, $h\nu$ is the energy of the incoming photons, E_{bind} is the binding energy of the electron, and Φ is the work function. In case of solid state PES, the Fermi-Energy E_F is used as a Zero energy rather than the Vacuum energy E_{Vac}. The latter one is suitable as reference in case of spectroscopy of atoms and molecules. With E_F as a reference, the calculation of the binding energy simplifies to

$$E_{kin} = h\nu + E_{bind}$$

Usually, the energy of the occupied states is negative, as the energy is below E_F.
The photoelectron leaves a core or valence hole behind, which is partially screened by the remaining electrons. When valence electrons are missing due to a partial transfer to a more electronegative atom, for example from metal atom to an oxygen atom, the core hole screening is less effective and the attractive force of the positive potential on the photoelectron is larger. This leads to reduced kinetic energy respectively higher binding energy, according to the equation above. This is known as chemical shift and allows determination of the chemical bonding properties between the different atoms, for

example if a metal is present as element or in an oxidized form.
Final state effects can play an important role, as they can cause complex line shapes. The most obvious final state effect is the splitting of the core lines with a non-zero angular momentum quantum number i.e. p, d, and f subshells, into two components due to the spin-orbit coupling. In the initial state, the 2p core level of e.g. a titanium atom is filled with six electrons and thus has Zero electronic angular momentum and Zero total spin. Only upon the creation of a core hole by photoemission, resulting spin and angular momentum in the final state are non-zero, which gives rise to the split into two components with $J = L \pm S$, corresponding to parallel respectively anti-parallel alignment of electronic spin and angular momentum. In case of a photo hole in a p-orbital, the electronic angular momentum L is 1, while the total spin S is 1/2, regardless the symmetry of the orbital. This leads to the well known $2p_{3/2,1/2}$ doublet, with total angular momentum J of 3/2 respectively 1/2. The branching ratios of the final states correspond to the statistical weight, according to their multiplicity of $2J + 1$, which leads to a branching ratio of 2:1 in case of p orbitals.
The photoemission process is followed by two competing relaxation processes. On one side, the core hole can be filled by an electron from a higher subshell, while the energy difference is released by a photon. Such a process has to follow the dipole selection rules, as fluorescence is an optical process. The second process is the Auger decay, in which the energy difference between the initial core hole and the filling electron is not released as a photon, but is transferred to another electron, which is subsequently ejected from the atom. The final state is a two hole final state, but with lower energy than the initial state with one hole in a deep core level. An Auger process, in which a hole in the 1s shell is filled by a 2p electron, and another 2p electron is released, is shortly described as $KL_{2,3}L_{2,3}$ Auger. In contrast to the photoelectrons, the kinetic energy of an Auger electron is independent from the excitation energy, as well as from the particular process, which has created the initial core hole. As the Auger decay is modulated by the coulomb operator rather than the dipole operator, transitions like $L_{2,3}M_{2,3}M_{2,3}$ are not forbidden. In addition to the previously described normal Auger, the Coster-Kronig (CK) and super-Coster-Kronig (sCK) Augers are of importance as well. This effect has been described in 1935 [63]. The fundamental difference to the normal Auger is the fact that the initial hole and the filling electron have the same principal quantum number, for example if the initial L_2 hole is filled by an L_3 electron, and the small (in comparison to the difference between L and M shell) energy difference is transferred to an electron with low binding energy. The effect has been described in photoemission experiments of gases as well as of solids. This effect is the reason for the absence of the L_2 auger lines in the series of the early 3d transition metals. In the previously introduced notation, the CK process can be written as $L_2L_3M_{45}$, if the spin-orbit split between the L_2 and L_3 hole is larger than the ionization energy of the M_{45} subshell, which is in case of a 3d metal $\approx \Phi$. The CK

process is faster than the normal Auger, and it is the dominating de-excitation process for the L_2 hole in case of the 3d metals [64] if it is allowed. Due to the small kinetic energy of the emitted electron, it cannot be detected in a photoemission experiment, as it is vanishing in the background of inelastically scattered electrons. In case of a solid, additional relaxations such as thermalisation have to be considered as well.
It is also known that the absence of the L_2 Augers in the early 3d transition metals is not caused by a fluorescence process that is filling the L_2 hole, which was shown by Kurmaev et al. in [64] by means of x-ray emission spectroscopy.
In the sCK decay, all participating electrons have the same principal quantum number, for example an $M_{23}M_{45}M_{45}$ decay is an sCK transition.

3.2.2 Experimental realization of PES

The PES measurements are carried out at the ASAM end station at beamlines U49/2-PGM2 and TGM7 at BESSY II, with a base pressure in the analysis chamber in the 10^{-10} mbar range. The energy reference was provided by a clean gold sample, and the Au $4f_{7/2}$ line is calibrated to -84.0 eV. Due to the high accuracy of the photon energy settings, this procedure did not need to be repeated for every single measurement. The binding energy positions of Ti $2p_{3/2}$ and Ti 3p are then used as an internal reference instead.
The optimization of the sample position for the measurement is realized by two steps. At first, the position of the sample is aligned by finding the maximum intensity of a photoelectron peak of the sample e.g. Ti 2p in TiO_2. Subsequently, the image of the CCD camera is used for fine adjustment.
For the quantitative analysis, the time dependence of the photon flux at a synchrotron light source has to be taken into account, as the total photoemission intensity depends on the intensity of the incoming x-rays. This is done by monitoring the incoming photon flux by a tungsten wire (diameter 75 µm), which is positioned in the path of the synchrotron radiation beam behind the exit slit. The intensity is monitored by measuring the current versus ground, which directly depends on the incoming intensity, with a pico-ampere meter. At the TGM7, the intensity is measured by recording the current versus ground on the last mirror. The analogue output voltage of the pico-ampere meter serves as measure for I_0. It is of great importance that the analogue output is only a relative signal rather than an absolute measure.
In order to calculate the overlayer thickness in a substrate-overlayer experiment, the photoemission spectra have to be normalized by dividing them by the measured I_0 value respectively the recorded output voltage of the pico-ampere meter. In order to avoid additional noise in the measured and to-be-normalized spectra, a mean value of I_0 respectively of the recorded signal was applied for the normalization of each spectrum rather

than a point-by-point division.
The equivalent overlayer thickness is calculated by the following equation:

$$I_s(d) = I_{s,0}\left(\exp\frac{-d}{\lambda_{el}\cdot\cos(\theta)}\right)$$

where $I_s(d)$ is the intensity of the substrate photoemission line, when it is covered by an over layer of thickness d, $I_{s,0}$ is the intensity of the clean substrate, θ is the angle between surface normal and optical axis of the analyser, and λ_{el} is the effective attenuation length of the substrate photoelectrons in the overlayer. The EAL is a function of the kinetic energy and determines the information depth. The EAL is calculated with the model from Cumpson and Seah [65]. Before analysis of the spectra, the inelastic background due to inelastic scattering has to be removed.

3.3 X-ray absorption spectroscopy

3.3.1 Fundamentals of x-ray absorption spectroscopy

In principle, x-ray absorption spectroscopy probes the x-ray absorption cross section σ as a function of the excitation energy. The absorption coefficient can be written according to the Lambert-Beer law:

$$I(d) = I_0\exp\left(-\frac{d}{\lambda_{ph}}\right)$$

where I_0 is the incoming intensity, $I(d)$ is the light intensity after passing through the medium of thickness d, and λ_{ph} is the penetration depth of the photons, which defines the distance after which I_0 has decreased to $\frac{I_0}{e}$. The penetration depth is the inverse of the absorption coefficient of the material, which has a linear dependence from the absorption cross section σ.
Finite absorption occurs if one initial state Ψ_i and one final state Ψ_f are coupled by the dipole operator to result in Fermi's Golden Rule:

$$I_{XAS} \propto \left|\langle\Psi_f\left|e\cdot\vec{r}\right|\Psi_i\rangle\right|^2\delta(E_f - E_i - h\nu)$$

where the delta function ensures energy conservation. If more than one final state is possible, which will be usually the case, one has to sum up over all final states. This equation implies when choosing a core state as Ψ_i and an empty state as Ψ_f, I_{XAS} is a measure for the empty states. If the continuum is chosen as Ψ_f i.e. a transition into the vacuum, the absorption cross section of Ψ_i will be Zero if $h\nu < E_f - E_i$, and it will have a finite value if $h\nu \geq E_f - E_i$. Consequently, the cross section σ will show a step. Additionally, there are unoccupied states below E_{vac} that give rise to additional finite values of I_{XAS} every time

the energy conservation is fulfilled, causing the fine structures in the near edge region. The origin of the complex fine structures will be described in more detail in Section 3.5. Fermi's Golden rule only describes the absorption of the incoming photon by a transition from an occupied state into an empty state, but it does not consider the following de-excitation processes. The excited state will not be stable but it will subsequently decay. Any radiative process will be excluded from the description, as this is not of relevance for this thesis.
In principle, the presence of the core hole is not too different to the situation that is described in the PES Section 3.2. The role of the additional electron in a state below E_{vac} will be described in Section 3.4. As already described, the core hole enables the relaxation via Auger processes, which gives rise to significantly enhanced number of emitted electrons, when a transition from an occupied state to an empty state is allowed with respect to conservation of energy.

3.3.2 Experimental realization of XAS

In order to measure the absorption coefficient respectively the absorption cross section in a transmission experiment based on the Lambert-Beer law, accurate measurement of I_0, $I(d)$ and d would be necessary. This is connected with serious problems, as in soft x-ray energy range, the penetration depth λ_{ph} is in the range of a few µm, which directly implies that the sample thickness needs to be in this range as well. This can only be achieved by additional ex-situ preparation, which means that in-situ studies of growth processes are not possible. In contrast to this, one can measure the total number of all emitted electrons, which is also a measure for the absorption coefficient.
The number of emitted electrons directly corresponds to a current, which flows from the ground to the sample, as both are connected. This current can be measured by one pico-ampere meter and the analogue output is fed to the measurement computer.
Besides the measurement in TEY mode, additional possibilities for XAS exist that are briefly mentioned for the sake of completeness. It is also possible to measure the intensity of background electrons with a fixed low kinetic energy (selected yield), Auger electrons (Auger yield) or partial yield, which allows to suppress the contribution of very low kinetic energy electrons. In the experiments shown here, XAS is measured in TEY mode.
As it is the case for the photoelectron spectra, the XAS spectra normally need to be normalized to the respective I_0 values as well, in order to include the time dependence of the synchrotron. Additionally, the intensity distribution as a function of the chosen energy has to be taken into account, which is very important for energy ranges with rapidly varying photon intensities like around the carbon 1s edge, where intensity variations of around 90% occur [66]. This is not an effect of the storage ring, or the properties of the undulator or monochromator, but is due to the presence of carbon contaminations on the

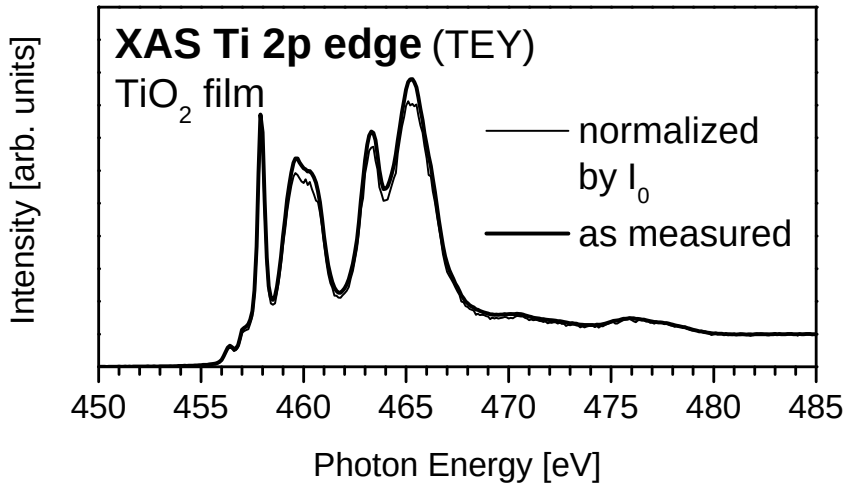

(a) XAS at Ti 2p edge, TiO_2 film

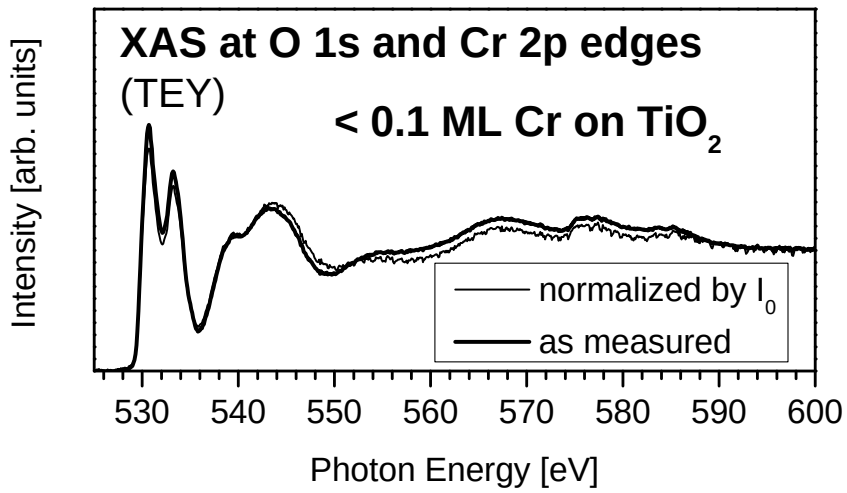

(b) XAS at O 1s and Cr 2p edges, <0.1 ML Cr on TiO_2

Figure 3.1: Comparison of I_0 normalized XAS spectra (thin lines) and as-measured XAS spectra (bold lines). Both datasets are normalized to an edge jump from Zero to One.

optical elements. In contrast to this, there is virtually no dependence of the photon flux from the excitation energy in the energy that are relevant throughout this thesis.

In Fig. 3.1, this is shown as an example. The top panel shows two XAS spectra of an as-prepared TiO_2 thin film at the Ti 2p edge, measured in TEY mode. Both spectra are normalized to absorption per atom, i.e. to an edge jump from Zero to One. The thin curve is divided by the measured I_0 curve before this procedure, the bold line is normalized without dividing it by I_0 before. As it can be clearly seen, the additional normalization procedure affects the intensity of the main features only in a minor way. It is visible as well that the I_0-divided spectrum exhibits additional noise, which is introduced by the noise of the I_0 curve. As a consequence of the fact that the spectral shape is not influenced by I_0 normalization, this procedure is skipped, and the Ti 2p XAS spectra are not divided by I_0.

The bottom panel of Fig. 3.1 shows the XAS spectra of less than 0.1 ML of chromium

on TiO_2 at the O 1s and Cr 2p edges. For the sake of simplicity, these spectra are set to Zero before the O 1s edge at 525 eV, and set to One behind the Cr 2p edge at 600 eV. As it is the case in the Ti 2p region, the main effect of I_0 division is introduction of increased noise into the spectrum, while the shape of the main spectral features is not influenced significantly. The intention is to avoid additional noise, especially in the energy region of the Cr 2p edge (from 570 eV to 600 eV), where low signal intensity is evident. Consequently, the O 1s and Cr 2p XAS spectra are also not divided by I_0.
The Cr 2p spectrum reveals another problem of the analysis of the XAS spectra. In the as-measured spectrum as well as in the normalized spectrum, the background intensity before the edge is higher than behind, which makes the absorption per atom ansatz impossible. This effect is not caused by a varying beam intensity, as it occurs in both spectra. It is more likely that this is background contribution from the O 1s XAS signal of the substrate.
Stöhr [67, Ch. 5] describes additional possibilities of background correction for XAS spectra, with focus on overlayer-substrate experiments, which is important for Section 5.3.2. One procedure involves subtraction of an XAS spectrum of the clean substrate from the XAS spectrum of the overlayer-substrate system. Due to the absence of a TEY spectrum of clean TiO_2 in the energy region above 565 eV, the background can only be approximated in first order by a linear function. Thus, the Cr 2p XAS spectra are scaled to the same intensity before the edge, and a linear fit of the pre-edge region is applied. This linear function is then subtracted from the spectra. In order to include the character of overlayer-substrate experiments with increasing overlayer thickness, the individual spectra are then normalized to the edge jump of the maximum achieved layer thickness i.e. the maximum layer thickness has an edge jump from Zero to One, while the lower thickness are normalized to this edge jump. For the normalization of the O 1s and Ti 2p XAS spectra a similar approach is applied, except the fact that additional subtraction of a background is not necessary. Here, the XAS spectra are normalized to the edge jump of the clean substrate.
It should be noted that with advanced experience with the integrated setup, significant advances with noise reduction have been made, which is of great interest for future experiments in the field of ultra-thin films.

3.4 Resonant photoelectron spectroscopy and constant initial state spectroscopy

In general, resonant photoelectron spectroscopy can be considered as energy resolved XAS spectroscopy. While in XAS the integral over all possible transitions is probed, ResPES delivers more detailed information as the emitted electrons are used to record valence

band or core level spectra when the excitation energy is scanned across an absorption edge.

3.4.1 Fundamentals of resonant photoemission spectroscopy

As it is the case in x-ray absorption spectroscopy, a tunable light source is necessary in order to set the excitation energies to values that correspond to the specific absorption edges of an element in the sample. The excitation and de-excitation processes are the same as in XAS spectroscopy, but in contrast to this, the kinetic energy of the emitted electrons is measured in order to record sets of valence band spectra. Moreover, the energy resolution in the ResPES experiment allows to distinguish between the different decay processes. For the sake of clarity, the description of the processes will be limited to the 2p and 3d subshells, but it has to be pointed out that allowed decay channels are not only limited to the 2p and 3d shells, but also involve the 3s, 3p and 4s subshells.
The excitation process in a 3d transition metal can be written as follows:

$$\left[2p^6 3d^n\right] + h\nu \rightarrow \left[2p^5 3d^{(n+1)^*}\right]$$

This excited state now can decay via two distinct processes (fluorescence is excluded), which only involve the electrons. In the so-called spectator process the excited electron does not take part in the decay process:

$$\left[2p^5 3d^{(n+1)^*}\right] \rightarrow \left[2p^6 3d^{((n-2)+1)^*}\right] + e^-$$

The notation $((n-2)+1)^*$ is chosen to emphasize the fact that the decay process is carried out by two valence electrons, which are then consequently missing in the 3d shell (n-2), but the excited electron is still present. This results in a two hole final state with an excited electron in an empty state. This is an Auger-like final state (two holes) and the time scale for this process is in the fs range (1 fs = 10^{-15} s). The related features develop from resonant to normal Auger when the excitation energy is far from the absorption edge. Due to the Auger-like nature, these features will appear with constant kinetic energies.
The other process is the participator, in which the excited electron takes part in the decay. It can be written as follows:

$$\left[2p^5 3d^{(n+1)^*}\right] \rightarrow \left[2p^6 3d^{(n-1)}\right] + e^-$$

In terms of energy it does not make a difference if the excited electron recombines directly and a valence electron is emitted, or if this is vice versa. The final state is equivalent to

that of a direct photoemission channel:

$$\left[2p^6 3d^n\right] + h\nu \rightarrow \left[2p^6 3d^{n-1}\right] + e^-$$

This process is faster than the spectator decay with a typical time scale of 500 as (1 as $= 10^{-18}$ s). The equivalence of the direct photoemission and participator channels gives rise to an interference of both channels.

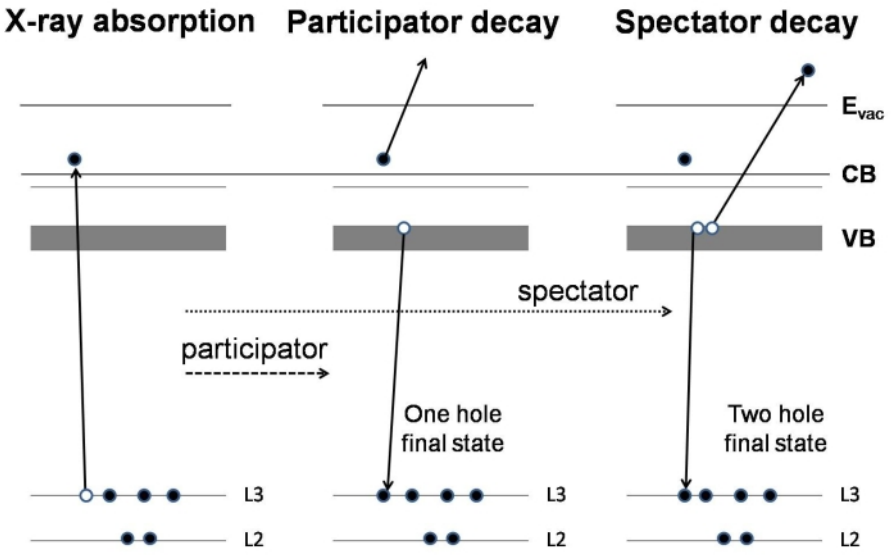

Figure 3.2: Schematic representation of the x-ray absorption (left) process and the following decay channels. In the participator channel (middle), the excited electron takes part in the decay process, which leads to a one hole final state, which is equivalent to a photoemission final state. In the spectator decay, the excited electron is not involved in the decay process leading to an Auger like two hole final state.

The description of the x-ray absorption process indicates that absorption occurs at one atom only, which consequently means that the following de-excitation process occur at the same atom. This will be of particular interest in sections 5.3.3 and 5.4.3, where this method is applied to distinguish the Ti 3d pDOS from the Cr 3d respectively Co 3d derived pDOS.

When one measures the intensity of a photoemission line as a function of the excitation energy across a resonance, a Fano line shape is observed in case of atomic excitation [68], which is the consequence of interaction between the bound states and the continuum [68, 62]. This method is also sometimes referred to as resonant photoemission, but throughout this thesis, the term ResPES means measurement of photoelectron spectra at resonant excitations, as described above. The measurement of the intensity of a particular line as a function of the excitation energy is better described as CIS (Constant Initial State) spectroscopy.

In the first order, a CIS spectrum probes the photo ionization cross section (PIX) as a function of the excitation energy. Close to the absorption edge, the intensity is modulated by an Auger matrix element rather than a dipole matrix element as it is the case in the XAS spectra [69], although it was shown by Prince et al. [69], that the CIS spectrum of the occupied states follows closely that of the XAS spectrum. Consequently, CIS spectroscopy can be described as site specific XAS.

3.4.2 Experimental realization of ResPES

In resonant photoemission experiments at the 2p ([69, 70, 71, 72]) and 3p ([27, 73, 74, 75, 76, 77, 78, 79]) edges, usually only special excitation energies are chosen. The selected energies mark special features in x-ray absorption spectra with high intensity and are thus considered to lead to corresponding high intensities in the photoelectron spectra. This method allows to put the focus on special properties like the resonant Auger regime, as shown by Ruus et al. in [71] or the valence band regime (Prince et al., [69]). By covering a broader excitation and binding energy range, a more detailed analysis of the resonant processes is possible.

As already mentioned, a tunable light source like a synchrotron is necessary for the realization of resonance photoemission experiments. Basically, the experimental procedure is the same as in the normal photoemission experiments, in which excitation energy, kinetic respectively binding energy, exit slit and the analyser parameters are chosen. In order to measure a full set of valence band spectra around the absorption edges, as shown in sections 5.1.3 and 5.2.3, all parameters are defined in the control software, before the sets of valence band spectra are recorded. The monochromator control of the integrated setup automatically switches the photon energy before each individual spectrum is recorded. For such a measurement, which covers the excitation energy around the Ti 2p edge from 450 eV to 485 eV with a step width of 0.4 eV, and the binding energy range from 2 eV above E_F down to -75 eV with a step width of 0.2 eV, a time span of roughly two hours is necessary. Similar to the normal photoemission spectra, a normalization by I_0 should be applied, in order to consider the decreasing light intensity over time.

In Fig. 3.4.2, the realization of a two-dimensional representation of such a ResPES dataset is shown. The horizontal axis is the excitation energy axis, the vertical axis is the binding energy axis, the color code of the intensity is logarithmic, where blue means low intensity and red means high intensity. The white spot marks a cut-off of the intensity. If the scale of both energy axes is chosen properly, the Auger lines appear under an angle of 45°, corresponding to their constant kinetic energies. In case of the 3p resonance dataset of titanium and titanium dioxide, the color code is linear instead.

The CIS spectra can be extracted along a horizontal line of the ResPES dataset, but due to the high step width of the excitation energy of 0.4 eV, individually recorded CIS spec-

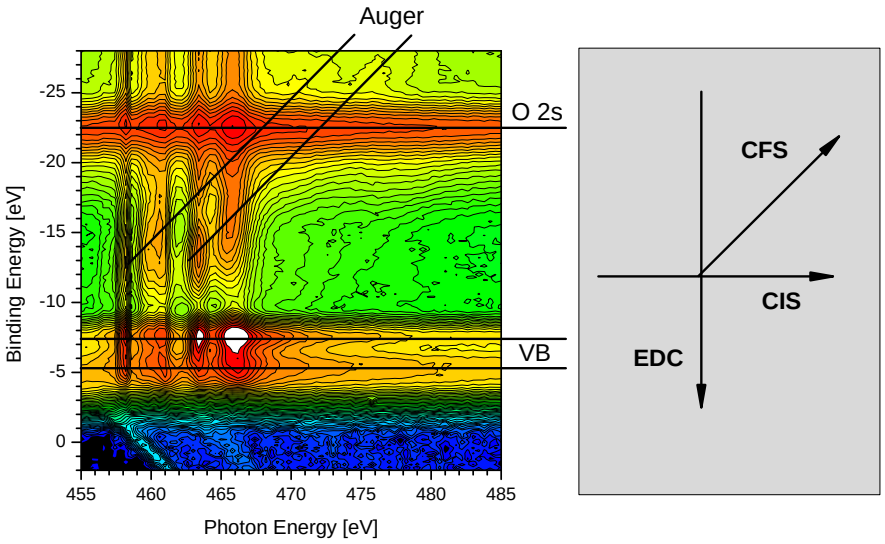

Figure 3.3: Two-dimensional representation of a ResPES dataset. Photoemission lines appear at constant binding energies (horizontal), along such a line, a CIS spectrum can be extracted. EDC spectra appear at constant photon energies, while Auger lines appear under an angle of 45°, if the energy scales are chosen properly with the same increment. The term CFS refers to the constant kinetic energy of an Auger line.

tra with smaller steps are recorded instead. The combined monochromator and analyser control software synchronizes the excitation energy $h\nu$ and the analyser settings E_{kin} in such a way that

$$E_{kin} - h\nu = E_{initial} = const.$$

with $E_{initial}$ being equal to the binding energy, and, according to the previous section, being negative for the occupied states.

One additional problem connected with the ResPES measurements is the second order light from the monochromator, which can be seen in Fig. 3.4.2 as a line crossing the band gap region under 90° with respect to the CFS lines. The second order light has twice the photon energy that is set by the monochromator control. In normal photoemission experiments, this contribution can be neglected as well as in resonance experiments of the shallow core levels. This can no longer be neglected when resonance photoemission is applied to study the valence band and band gap region. The second order gives rise to off-resonance excitation of the core levels that are subsequently measured at kinetic energies corresponding to the first order resonant excitations of valence band or band gap features. Assuming photoemission from the Fermi-Energy with $E_{bind,Fermi} = 0eV$, the kinetic energy of a photoelectron is, according to

$$E_{kin,Fermi} = h\nu + E_{bind,Fermi} = h\nu$$

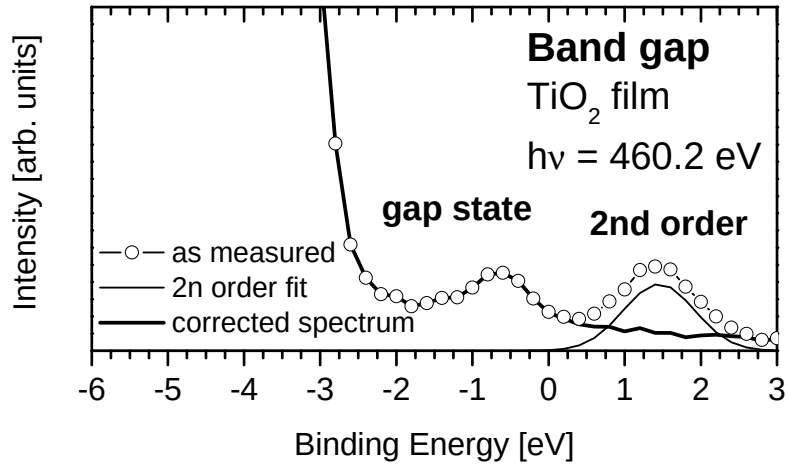

(a) 460.2 eV

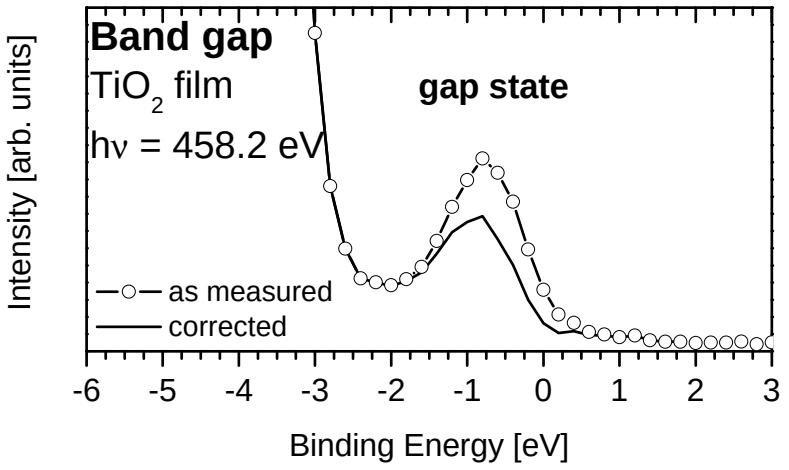

(b) 458.2 eV

Figure 3.4: Effect of the second order correction at the Ti 2p edge. In (a), the second order is well above the gap state resonance. In (b), the Gauss fit of the second order is shifted corresponding to the difference of the excitation energy, and subtracted.

The second order excitation of the core level is as follows:

$$E_{kin,core} = 2 \cdot h\nu + E_{Bind,core} = h\nu_{2nd\,order} + E_{Bind,core}$$

By definition, the binding energy of the core level is the same as the resonance energy i.e. the energy that is necessary to excite a core electron to an empty state above the valence band. Thus, the energy relation for the core electron is

$$E_{kin,core} = h\nu_{2nd\,order} + E_{Bind,core} \approx h\nu = E_{kin,Fermi}$$

The second order features can be easily recognized as their kinetic energy increases by two times the step width of the excitation energy, while the kinetic energies of first order

excitations of e.g. the valence state increase by the amount of step width of the excitation energy, and Auger lines have constant kinetic energies.
In case of the resonant spectra at the Cr 2p and Co 2p edges, the second order contributions can be neglected due to the very high resonance intensities of the Cr 3d and Co 3d states close to E_F. This is not the case for the Ti 2p edges, where the intensity of the second order is of the same order of magnitude as the intensity of the defect states, as seen in Fig. 3.4(a). The representations of the full resonance maps clearly show that the contributions of the defect states can be distinguished from the second order. For this reason, these datasets are shown as measured without additional correction. In order to compare the resonant valence band spectra in Sections 5.3.3 and 5.4.3, the second order contribution is subtracted from the Ti 2p resonant spectra. This procedure becomes necessary, as the resonance of the Ti 3d defect state coincides with the second order at the photon energies of interest.
In order to subtract the second order contribution, one has to assume that the measured intensity of the second order does not change significantly with photon and kinetic energy. Subsequently, a spectrum in which the second order is well separated from the gap state, e.g. where it is found above E_F is chosen, and the second order is background subtracted and fit by a Gauss function with a FWHM of 1.1 eV. According to the relations from above, the position of the second order at the resonance is calculated and the corresponding Gauss function is shifted and subsequently subtracted from the measured spectrum.
In case of the CIS spectra of the band gap states, an adapted procedure needs to be applied. Instead of fitting the second order of a valence band spectrum, the second order contribution of a CIS spectrum from above E_F is used. This spectrum needs to be extracted from the full dataset of the thin film. As the photoemission intensity of the Ti 2p core levels depends on the chromium coverage, consequently the contribution of the second order has the same dependence. In order to include this, the calculated second order contribution is scaled with the same factors as the Ti 2p core levels, before the contribution is subtracted.
The effect of both procedures is briefly shown in Figs. 3.4(a) and 3.4(b). The dotted spectrum in panel (a) shows the band gap region with the defect state at -0.7 eV, and the second order contribution at around +1.5 eV. In the corrected spectrum (bold line), this contribution is eliminated without showing an effect on the defect state, which indicates the validity of this procedure as it is additionally shown in panel (b).

3.5 Atomic multiplets and crystal field effects

The calculation of atomic multiplets is a very useful supplement for x-ray absorption spectroscopy and photoemission spectroscopy. The CTM4XAS program, which is applied

here, is based on the Cowan code [80], which is essentially a program code for the calculation of atomic spectra. This basic program was extended and finally features the calculation of atomic multiplets including crystal field effects and charge transfer effects [81, 82, 83, 84, 85]. The CTM4XAS program by Frank de Groot and Eli Stavitski from Utrecht University is an easy-to-use GUI for the Cowan code. Additionally, it is capable of calculating XPS spectra.
The reason for the usefulness of calculating atomic spectra rather than band structures is the fact that atomic effect in the transition metal compounds can be very large. This is related to the strong overlap of 2p and 3d wave functions of the final states, which is of the same order of magnitude in the atom and in the solid state. This consequently means that in a 2p $\rightarrow$ 3d XAS experiment the atomic-like effects are dominating, and such an experiment will not probe the density of empty states of the conduction band.
Soft x-ray absorption is an optical transition that follows the dipole selection rules. The electronic states are usefully described by the term symbols ${}^{2S+1}L_{L+S}$, where $2S+1$ is the spin multiplicity (S is the spin quantum number), L is the total electronic angular momentum (the symbols S, P, D, F, G ... are used for $L = 0, 1, 2, 3, 4 \ldots$) and $L + S = J$ is the total angular momentum, which is the sum of electronic angular momentum and spin.
In the XAS experiments, the following dipole selection rules apply:

- The selection rules for single electron transitions:
  - The angular momentum quantum number l: $\Delta l = \pm 1$, e.g. 2p $\rightarrow$ 3d or 3p $\rightarrow$ 3d
  - The magnetic quantum number m: $\Delta m = 0, \pm 1$
  - The spin quantum number s: $\Delta s = 0$
- The selection rules for multi-electron systems:
  - The total angular momentum J: $\Delta J = 0, \pm 1$, but $J = 0 \nrightarrow J = 0$
  - The electronic angular momentum L in case of L-S coupling: $\Delta L = 0, \pm 1$, $L = 0 \nrightarrow L = 0$
  - If $\Delta S = \pm 1$ in case of intermediate coupling, then $\Delta L = 0, \pm 1, \pm 2$

The selection rules show that in case of intermediate coupling, which is good approximation for the transition metals, the fundamental rule $\Delta s = 0$ is no longer valid, which will give rise to additional allowed dipole transitions.
The CTM4XAS program calculates the energies of atomic-like configurations for initial and final states, which means that all allowed ${}^{2S+1}L_J$ terms are determined. According to the selection rules, not all possible final states can be reached by a dipole transition from the ground state. This will be briefly described with the Ti^{4+} ion as an example.

In TiO_2, titanium can be described as Ti^{4+} ion with a $3d^0 4s^0$ configuration. All other shells (from 1s to 3p) are filled, which means that all spins are paired, resulting in a total spin of Zero. As all shells are either full or empty, the electronic angular momentum is Zero as well, which also leads to total angular momentum of $J = 0$. The term symbol of the ground state is $^1S_0$. When one electron is excited from the full 2p shell to the empty 3d shell, the configuration can be written as $2p^5 3d^1$ with $l_1 = 1$ (p-shell) and $l_2 = 2$ (d-shell). The possible electronic angular momenta are now $L = |l_2 - l_1|; |l_2 - l_1| + 1 \ldots l_2 + l_1$, which is in this case $L = 1; 2; 3$, corresponding to P, D, F term symbols. For the total spin, two values are possible (parallel or anti-parallel) with $S = 0; 1$, which leads to $J = |L-S| \ldots L+S$ (negative values of J are not allowed). The possible J values are now for P: $J = 0; 1; 2$ for D: $J = 1; 2; 3$ and for F: $J = 2; 3; 4$. In particular, transition to the F state could only be reached by a violation of the J-rule, and is thus a dipole-forbidden transition. For P, the spin can be $S = 0; 1$ to reach $J = 1$, and for D with $L = 2$, $J = 1$ can only be reached via $|L-S|$ when the spin is $S = 1$. This gives rise to three final states with $^{1,3}P$ and ^3D term symbols. Reduction of the symmetry from SO_3 to O_h branches this three states into 7 states.

These results indicate that the number of lines in a 2p XAS spectrum is not a measure for the number of nominally empty d-orbitals, while the total intensity is [86, Sec. 5.1.3], according to Fermi's Golden rule.

In the model, the ligands are treated as point charges and their influence on the energy of the final states is the result of pure electrostatic interaction. In O_h symmetry, the metal ion is in octahedral coordination by six ligands, e.g. oxygen, as it is the case in TiO_2. This reduced symmetry breaks the five-fold degeneracy of the 3d-orbitals (d_{z^2}, $d_{x^2-y^2}$, d_{xy}, d_{xz}, d_{yz}) into the two-fold degenerate high energy e_g states, with the orbital lobes pointing towards the ligands, and the three-fold degenerate low energy t_{2g} states with the lobes pointing between the ligands. This is shown in Figs. 3.5(a) and 3.5(b) as an example.

The t_{2g} orbitals have small overlap with the ligand orbitals, and are lowered in energy by 4 Dq with respect to the energy of the d orbitals in spherical symmetry, while the e_g orbitals have increased energy by 6 Dq. Thus, the difference between these two sub-levels is 10 Dq, with the energy of the ion in spherical symmetry being the barycentre. In a tetrahedral field, the ordering of the orbitals is opposite to the case of O_h symmetry. Now, the e orbitals have decreased energy, while the energy of the t_2 orbitals has increased. The index g is not necessary in tetrahedral field, as the tetrahedron does not have an inversion center [39, Ch. 11].

In the CTM calculation, the T_d symmetry is realized by choosing O_h symmetry with negative 10 Dq.

Calculation of tetragonal distortion (D_{4h}) also starts with O_h symmetry. The example shows the effect of z-axis elongation for tetragonal distortion, in which the ligands in z-direction are shifted away from the central atom. This lowers the energy of the 3d orbitals

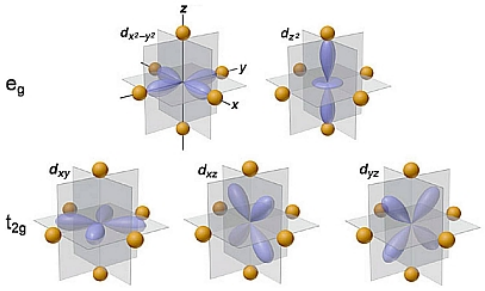

(a) 3d orbitals

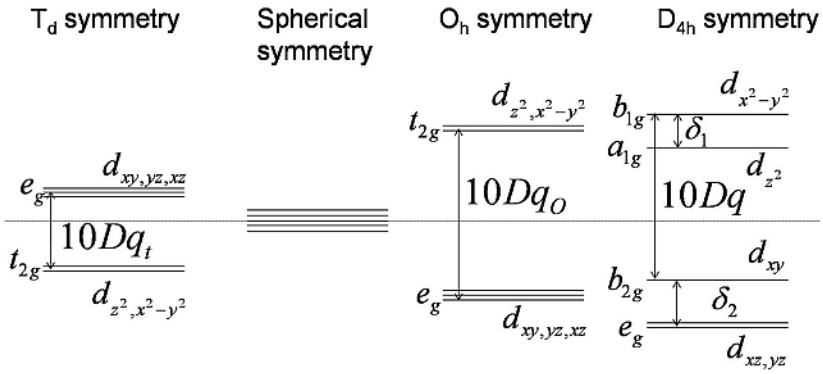

(b) Crystal field effect on the 3d orbitals

Figure 3.5: Representation of the 3d orbitals in octahedral symmetry, and the crystal field effect from spherical to O_h to D_{4h} symmetry (reproduced from [85])

with a z-component, removing the degeneracy of the e_g levels and splitting them into two b_{1g} and a_{1g} levels, while the degeneracy of the t_{2g} states is not fully removed as one state now has b_{2g} symmetry ($3d_{xy}$). ,The remaining two levels have lower energy due to their z-components and form an e_g state. The crystal field parameter 10 Dq is now defined as the energy difference between $3d_{x^2-y^2}$ and $3d_{xy}$, while the difference between $3d_{x^2-y^2}$ and $3d_{z^2}$ is δ_1 and the difference between $3d_{xy}$ and $3d_{xz}$ respectively $3d_{yz}$ is δ_2. For the CTM4XAS program, the optical parameters Dq and Ds have to be used instead, but the relation between the three parameters and the energy positions of the d-orbitals is shown in table 3.2.

Level	Energy in D terms	Orbital
b_{1g}	6 Dq + 2 Ds - 1 Dt	$3d_{x^2-y^2}$
a_{1g}	6 Dq - 2 Ds - 6 Dt	$3d_{z^2}$
b_{2g}	-4 Dq + 2 Ds - 1 Dt	$3d_{xy}$
e_g	-4 Dq - 1 Ds + 4 Dt	$3d_{xz,yz}$

Table 3.2: Energy of the d-levels in D_{4h} symmetry (from [85])

From this table, the energies δ_1 and δ_2 are calculated to $\delta_1 = 4Ds + 5Dt$, $\delta_2 = 3Ds - 5Dt$, which also suggests that in pure D_{4h} distortion (axial elongation or compression), the parameters Dt and Ds cannot be chosen arbitrarily. This table also includes the opposite case of axial compression, in which the order of the orbital energies is reversed i.e. orbitals with z-components have increased energies while the orbitals with only x- and y-components have lowered energy.

As it is shown in the previous Chapter 2, the local structure of the $[MO_6]$ octahedra in the introduced transition metal oxides is more complex, i.e. additional distortions occur. Nevertheless, D_{4h} symmetry is applied in the multiplet calculations throughout this thesis, as the distortions are rather small.

The covalent bonding character in the transition metal oxides is taken into account by the charge transfer states. This is realized by mixing $d^n\underline{L}^0$ and $d^{n+1}\underline{L}^1$ in the ground state, and subsequently performing the CTM calculation. The electrons are described as $2p^63d^nd^{10}$, where d^{10} means $\underline{L}^0$. The CT state is described as $2p^63d^{(n+1)}d^9$, which respects the correlation and the d-character of the electron when it is transferred from the ligand into the metal d-shell. The excited states $2p^53d^{n+1}d^{10}$ and $2p^53d^{(n+1)+1}d^9$ are then also mixed, resulting in a more complex fine structure of the spectra.

The calculation of XPS spectra starts with the same initial states, but the description of the final states is different. Rather than describing the excited electron in a correlated d-state as in case of 2p-3d XAS, the excited electron is described as s-state with a high principal quantum number ($n = 99$), without correlation. This realizes the description as a free electron.

It has to be mentioned that the program only calculates the energies of initial and final states, as well as the matrix elements of the dipole transitions, but it is not capable to include the dynamics of the XAS process and the subsequently occurring decay- respectively de-excitation processes that are described above.

Chapter 4

Sample preparation

4.1 Rutile (110)

The Rutile single crystals with a size of 5 mm × 10 mm × 0.5 mm are purchased from SurfaceNet company in Rheine, Germany. The crystals with a pale yellow color are in the (110) orientation, with one side polished. Although in XPS measurements neither charging nor significant contaminations are detected, this is different at the high intensity and high sensitivity synchrotron radiation facility. In this case, strong charging effects due to the high flux density occur. Besides this, measurements with high surface sensitivity revealed presence of sodium and potassium.
For this reason, the crystals have to undergo a preparation procedure for the synchrotron radiation measurements, in order to prevent charging on one side, as well as removal of the surface contaminations on the other side. Charging can be avoided by reducing the insulating crystal to TiO_{2-x}. This is achieved by heating the crystal in UHV conditions at a base pressure of about 10^{-8} mbar to a temperature of more than 900°C for 3 hours with a halogen lamp. This step also removes carbon contamination. After this heating procedure the color of the crystal has changed from pale yellow to dark blue, which indicates reduced TiO_{2-x} bulk material. This is seen in Fig. 4.1.
Sodium and potassium contaminations are then removed by cleaning cycles, in which 10% HNO_3 and 10% $C_2H_2O_4$ (oxalic acid) are applied alternately. The crystal is rinsed with de-ionized water after each etching step. These cleaning steps are repeated, until no contaminations (sodium and potassium) are detected.
In order to restore a stoichiometric surface of the reduced crystal, this crystal is finally heated in ambient air to about 800°C with a halogen lamp for 20 minutes. The temperature is measured by placing a thermocouple onto the sample holder close to the sample. Despite the preparation step in ambient air, the presence of carbon on the surface is negligible, as can be seen in the overview spectrum in Fig. 5.1. A similar procedure of annealing in ambient air at high temperature is described by Taverner et al. in [87]. Ad-

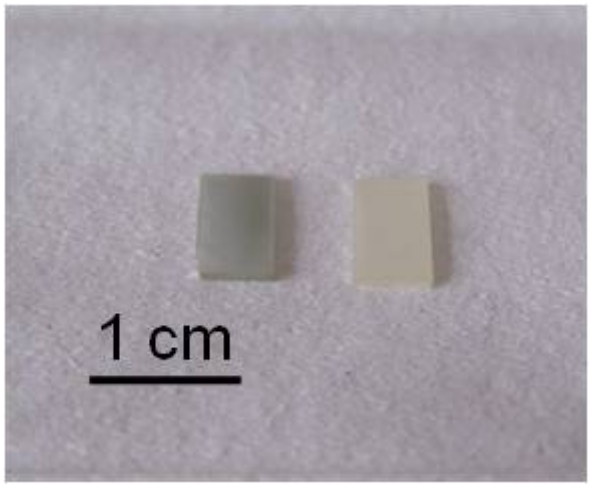

Figure 4.1: Picture of Rutile (110) crystals, taken from the box (right) and upon heating in UHV to above 900°C for 3 hours (left). The color turns from pale yellow to light grey, which indicates increased amount of oxygen vacancies

ditionally, the oxygen excess in ambient air also provides oxidizing conditions, which are crucial for the preparation of a stoichiometric oxide. This leads to a faster sample preparation than described by other authors, who oxidise the previously reduced and cleaned sample in vacuum conditions with oxygen background pressure in the 10^{-6} mbar range (for example as described in [21, 49, 56, 69, 76, 88, 89]).

4.2 Preparation of the Titanium Dioxide thin film

The preparation of the TiO_2 thin film involves a combined process, which consists of an in-situ metal deposition and an ex-situ oxidation step. Chemically stable silicon carbide is used as a substrate. The substrate is cleaned by heating in UHV conditions for a few minutes, in order to remove volatile contaminations. Subsequently, metallic titanium is evaporated onto the SiC by heating a titanium filament with a diameter of 1 mm to approximately 1000°C. The typical current to achieve this temperature is around 13 A. The base pressure of 10^{-9} mbar in the preparation chamber rises by more than two orders of magnitude, but quickly drops down to the low 10^{-7} mbar range. Only in this pressure range, the substrate is placed in front of the source to avoid deposition of contaminations. This deposition step takes around one hour until an approximated layer thickness of up to 10 nm is reached. The layer thickness is estimated by the vanished photoemission signals from the substrate.
The oxidation step in ambient air is done in the same way as the annealing procedure of the Rutile crystal. The idea behind the preparation step in ambient air is the same as in case of the single crystal.

4.3 Chromium and cobalt deposition

When the as-prepared thin film is characterized and stoichiometry and absence of pronounced band gap emission is determined, chromium respectively cobalt is deposited onto the thin film. The chromium source is a self-made evaporator, which consists of an electrical feedthrough, a small basket made of tungsten wire (diameter 0.5 mm), which is filled by small pieces of chromium. The typical size of these pieces is a few mm. The wire basket is heated electrically until it shows a bright yellow-white glow, which corresponds to a roughly estimated temperature of 1300°C. Typical currents of 16–18 A are necessary for this. The pressure in the UHV system is in the same range as it is in case of titanium evaporation. It is important to carefully out-gas the source after bake out of the system, as well as an additional out-gassing prior to deposition of the material. The deposition rate is roughly 1 nm per 10 minutes, with typical duration of a deposition step being as short as 10 seconds up to 30 seconds, leading to ultra-low chromium thickness in the sub-ML-regime.

Cobalt is available in form of high purity wires. For this reason, a similar setup as in case of the titanium source is chosen. The diameter of the filament is 1 mm as well, in contrast to the titanium wire the applied current has to be significantly higher due to the higher conductivity of cobalt. The typical current values are around 17–18 A. The deposition rate is approximately 2–3 nm per 10 minutes.

Chapter 5

Results

In this chapter, the experimental and theoretical results will be described in detail. Beginning with the SR-PES results of the Rutile (110) single crystal, followed by the results obtained from the thin film of TiO_2. This will be followed by the description of the results of chromium deposition on the TiO_2 thin film and the cobalt growth on such films. In addition to the experimental XAS spectra, CTM calculations are applied to obtain additional information.

5.1 Rutile (110)

In this section, the SR-PES results, including core level (2p and 3p lines) and valence band photoemission, x-ray absorption and resonant photoemission at the Ti 2p edge, are presented.

5.1.1 SR-PES Results

In the overview spectrum of the prepared single crystal with hν = 900 eV, shown in Fig. 5.1, the most intense lines are the O 1s and Ti 2p emissions at around -530 eV and -460 eV respectively. Less prominent features are the oxygen KLL-Augers, that appear at binding energies of around 400 eV, corresponding to kinetic energies of around 500 eV. The titanium LMM-Augers appear at binding energies of around 500 eV. The shallow core levels (Ti 3s and 3p, O 2s) and the valence band are the minor features at the low binding energy side from -75 eV to 0 eV.
The inset magnifies the C 1s region by a factor of 10 to emphasize the fact that despite the preparation step in ambient air, only negligible amounts of carbon are present at the surface. The Ti 2p core level emission, excited with photon energy of 900 eV, is shown in Fig. 5.2(a). It splits into the $2p_{3/2}$ and $2p_{1/2}$ doublet, the lines appear at binding energies of -459.3 eV and -465 eV, resulting in a spin orbit split of 5.7 eV. The FWHM of the $2p_{3/2}$ line is 1.1 eV, while the $2p_{1/2}$ line exhibits significantly larger width of 1.8 eV. The

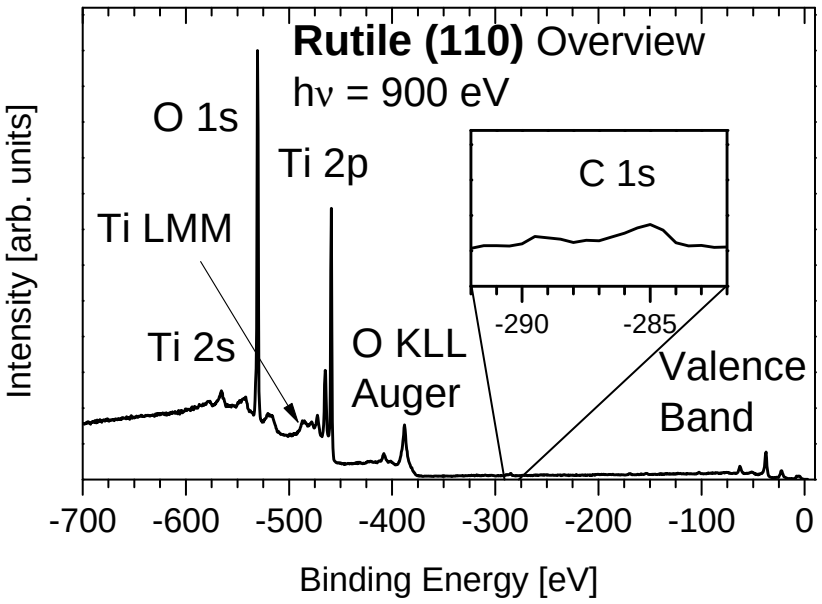

Figure 5.1: Overview spectrum of the prepared Rutile (110) single crystal, excited with 900 eV. The C 1s region is magnified by a factor of 10

absence of features at the low binding energy side of the $2p_{3/2}$ line indicates that there are no detectable Ti^{3+} or lower oxidation states present in the sample. The calculated branching ratio between the two components is 2.3, which is a difference to the theoretical value of 2. In addition to the main lines, two satellite peaks A and B are observed as well, each separated from its main line by 13.5 eV. The binding energy of -459.3 eV is that of titanium in the Ti^{4+} state, according to [1], although a wide range of binding energies of the Ti $2p_{3/2}$ line is reported in literature. Mayer et al. report binding energy values from -455.5 eV to -461.8 eV in [16].

In Fig. 5.2(b), the O 1s photoelectron spectra, measured in surface (open circles) and bulk (full circles) sensitive mode, are shown. In order to allow a better comparison, both spectra are normalized to a peak height of One. The O 1s peak appears at binding energy of -530.6 eV in the bulk sensitive mode and shifts by 0.1 eV to -530.7 eV in the surface sensitive mode. This shift of 0.1 eV will not be further discussed. The binding energies are different to the value of 530.4 eV given by Diebold in [1], although the Ti 2p line is in agreement.

Both O 1s spectra show an additional component at the high binding energy side at around -532 eV. In the surface sensitive mode the intensity of this shoulder is significantly higher in comparison to the main line than in the bulk sensitive measurement. The shoulder at the high binding energy side of the O 1s line is reported in the literature as well [90, 91, 92]. A detailed peak analysis will be presented later on.

The Ti 3p spectrum excited with 150 eV is shown in Fig. 5.2(c). The peak position is at -37.6 eV and the FWHM of the 3p line is 2 eV, without any visible spin-orbit split. Similar to the properties of the Ti 2p line, the 3p line shows a pronounced satellite peak

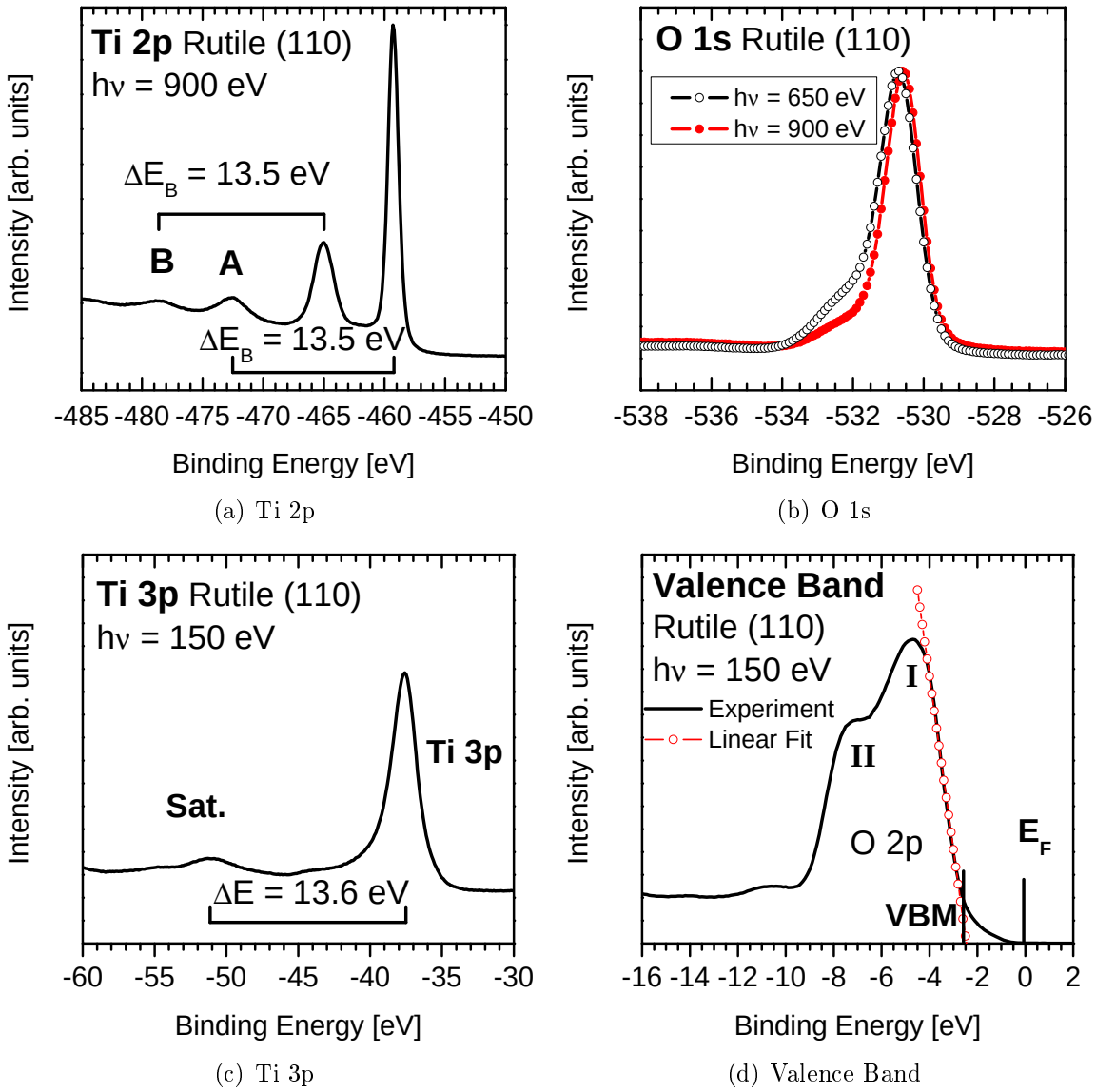

(a) Ti 2p (b) O 1s

(c) Ti 3p (d) Valence Band

Figure 5.2: Photoelectron spectra of Ti 2p, O 1s, Ti 3p and the valence band region of Rutile (110) single crystal

at -51.2 eV, which corresponds to a separation of 13.6 eV. The 3p peak shows additional contribution in the energy region between -42 eV and -45 eV. In [93] a binding energy reference of -37.5 eV for the Ti 3p line is given, with the reference of Ti 2p at -458.8 eV. Thus, the separation between the two lines is 421.3 eV. Oku et al. [94] give a binding energy of the Ti 3p line of -37.5 eV, with the Ti 2p and O 1s lines at -459.3 eV and -530.3 eV respectively, which results in a energy difference of Ti 2p to 3p of 421.8 eV.
The spectrum of the valence band region (Fig. 5.2(d), also excited with 150 eV) is dominated by the 5 eV broad O 2p band, with two pronounced peaks at -4.7 eV and -7.2 eV. The separation between these two prominent emissions is 2.5 eV. The linear fit of the upper valence band edge is used to determine the valence band maximum, which is thus found at -2.6 eV, but there is still significant emission from above the indicated valence band

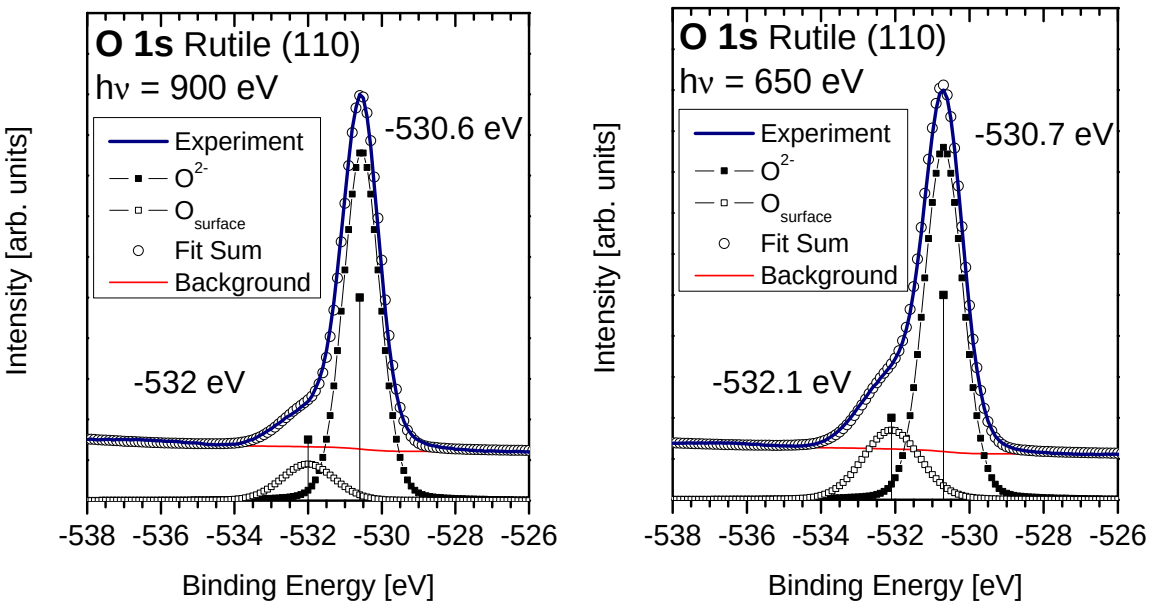

(a) bulk sensitive (b) surface sensitive

Figure 5.3: Peak analysis of bulk and surface sensitive O 1s photoemission peak. The position of each component is marked by vertical bars, and the binding energy values are shown.

maximum. The value of -2.6 eV differs from values from literature ([1, 21, 56, 95, 96]), where values of around -3 eV are given for the valence band maximum. It should be noted, that in [56] Rutile (001) instead of the (110) surface was used, and Fleming et al. [95] used Anatase instead of Rutile.

The detailed peak analysis of the bulk and surface sensitive O 1s spectra is shown in Fig. 5.3. Here, two Gaussian peaks with a Lorentz contribution of 12% are used to fit the photoemission spectrum. In case of the bulk sensitive measurement, the width of the main line, which reflects the O^{2-} state, is 1.2 eV while the width of the surface feature is 1.7 eV. The intensity ratio between the two components is 0.15. In the surface sensitive O 1s spectrum, the widths of both components remain the same, but as mentioned above, the intensity ratios change. Now a ratio of 0.29 between shoulder and main line is observed, corresponding to a change of almost a factor of 2. The authors of [91, 92] assign this feature to the bridging oxygen rows of 2-fold coordinated oxygen at the surface.

In Fig. 5.4, the photoelectron spectra of the two different measurement geometries (standard 45° incidence and grazing incidence) are compared with each other. In order to allow qualitative comparison, all spectra except the valence band spectra are normalized to a peak intensity of One. The latter ones are normalized to a peak height of One of the corresponding 3p spectrum. It can be seen, that the overall appearance of the core level spectra does not depend on the geometry. Only minor differences are observed. In the Ti 2p spectra in Fig. 5.4(a), the only observed difference is the fact, that the background intensity is slightly higher in case of the 45° setup. The main features of the spectrum are

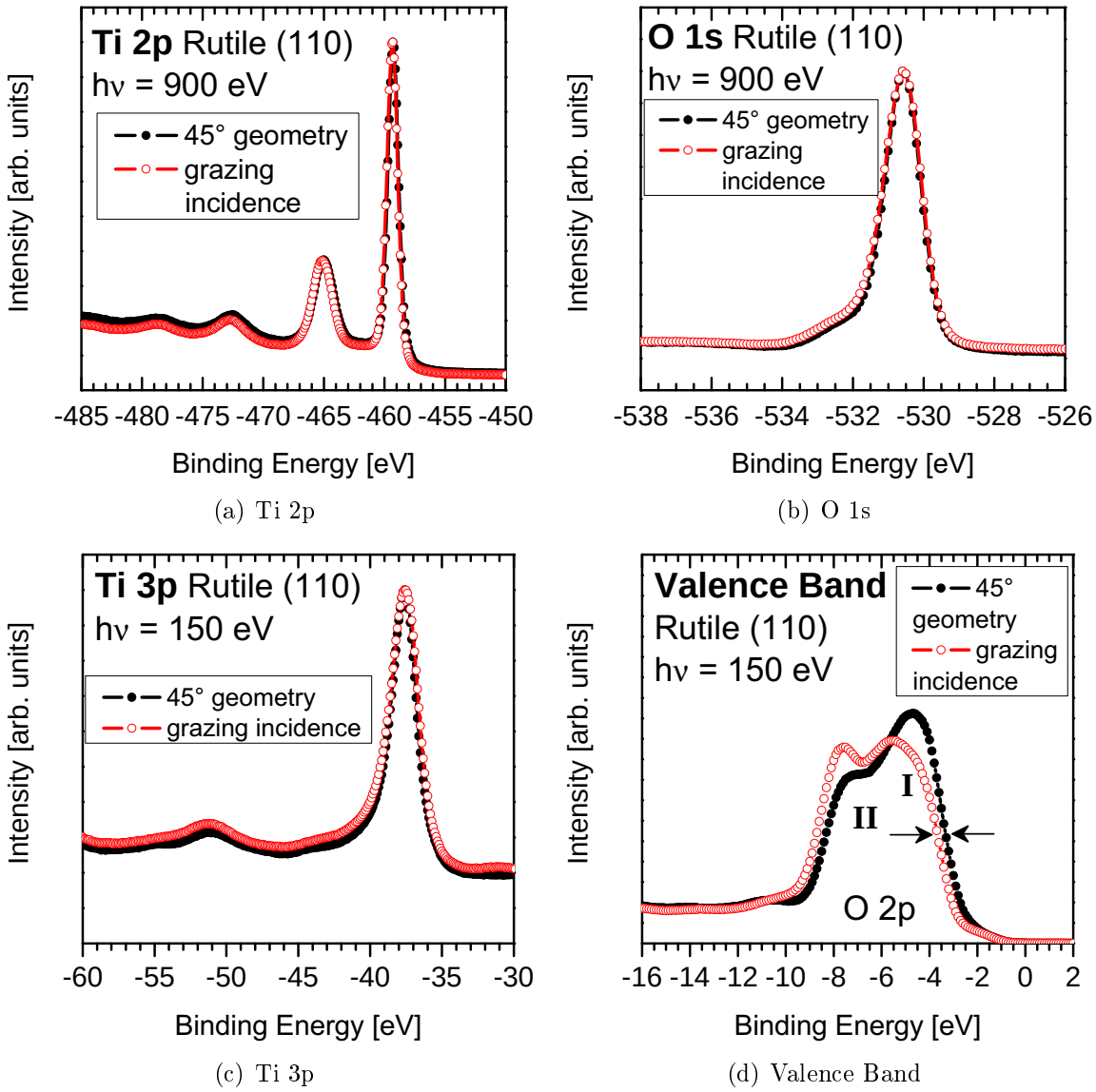

(a) Ti 2p (b) O 1s

(c) Ti 3p (d) Valence Band

Figure 5.4: Photoelectron spectra of Ti 2p, O 1s, Ti 3p and the valence band in 45° incidence angle (full circles) and grazing incidence (open circles).

essentially the same without changes of the FWHM, the spin orbit split and the intensity ratios of the $2p_{3/2}$ and $2p_{1/2}$ components. The difference of the background will not be discussed further. Similar results are found for the bulk sensitive sensitive O 1s spectra in Fig. 5.4(b), and the Ti 3p spectra. As above, these differences do not affect the shape of the photoemission peaks, but are seen in the background.

The only pronounced differences in photoemission are seen in the valence band spectra in Fig. 5.4(d). The spectrum measured in 45° setup (full circles) is described above. When the setup is changed to grazing incidence (open circles), the peak intensities of the two pronounced valence band peaks are almost the same now, while in 45° setup the intensity of the low energy peak is higher than the second one. The arrows mark a shift towards higher binding energy by 0.3 eV in case of grazing incidence i.e. the valence band maxi-

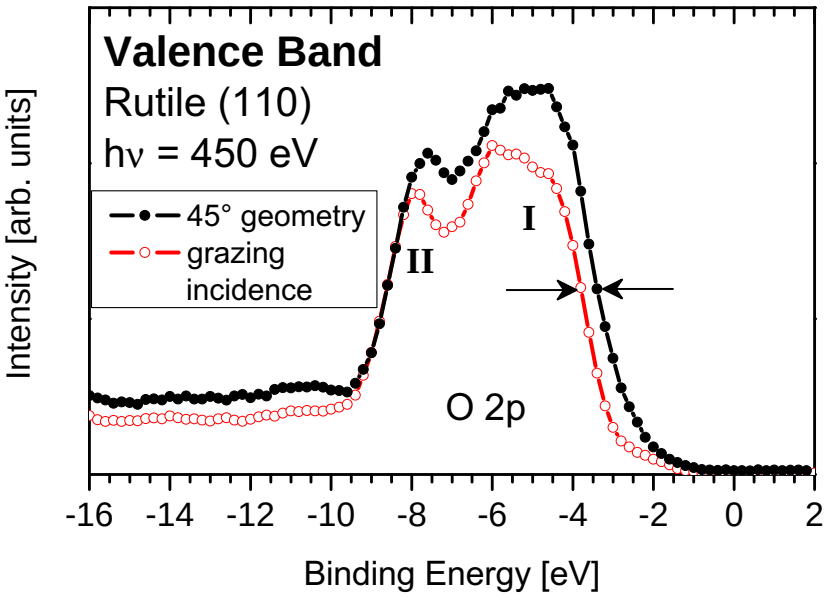

Figure 5.5: Bulk sensitive valence band spectra in 45° incidence angle (full circles) and grazing incidence (open circles).

mum is now found at -2.9 eV instead of -2.6 eV in the standard setup. Charging effects and experimental artefacts can be excluded here, as both spectra are referenced to the same binding energy of the Ti 3p photoelectron peak and this referencing results in a negligible shift of the O 2s lines of 0.1 eV. The valence band spectra in bulk sensitive mode are shown in Fig. 5.5. Again, the spectra are normalized to peak intensity of One of the respective 3p peak (not shown). In contrast to the measurement in which low excitation energy of 150 eV is used, now the intensity ratio of both valence band peaks remain the same when the geometry is changed. Additionally, minor changes of the specific shape are observed, but the reason for this can be the reduced signal to noise ratio. Similar to the results above, the valence band edge shifts downwards when the geometry is changed from an incidence angle of 45° to grazing incidence. This behaviour is indicated by horizontal arrows again. As above, charging is excluded, as both spectra are referenced to the same binding energy of the respective Ti 3p lines.

5.1.2 XAS and XLD Results

The x-ray absorption spectra at the Ti 2p and O 1s edges, measured in TEY mode, are shown in Fig. 5.6. Both spectra are normalized to an edge jump from 0 to 1, corresponding to so called "absorption per atom". Additionally, the O 1s XAS spectrum is magnified by a factor of 4 in comparison to the Ti 2p XAS. Although the assignment of states with e_g and t_{2g} symmetry is only valid for the O_h symmetry, the assignment of the peaks follows according to the description of van der Laan [2].

The x-ray absorption spectrum at the Ti 2p edge (Fig. 5.6(a)) shows two small pre-edge

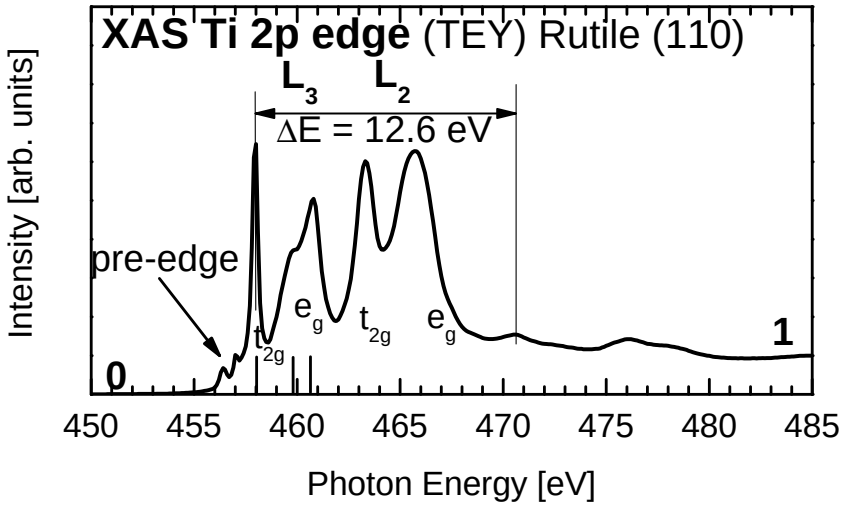

(a) Ti 2p edge

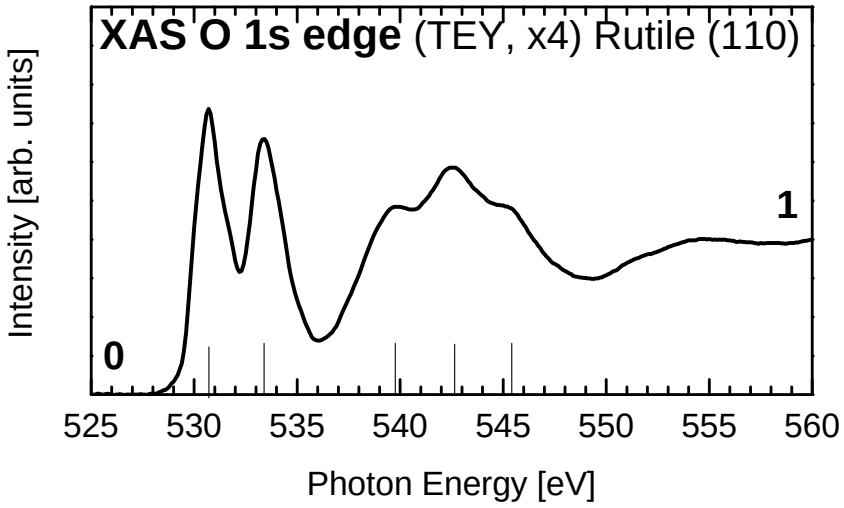

(b) O 1s edge

Figure 5.6: XAS at Ti 2p and O 1s edges; both spectra are normalized to absorption per atom (the O 1s spectrum is additionally magnified by x4)

features, that arise at photon energies of 456.4 eV and 457 eV. The spin orbit interaction splits the spectrum into the L_3 and L_2 components, as indicated in the figure. In the L_3 component of the spectrum, three lines can be identified. The first one arises at 457.9 eV, reflecting the empty Ti 3d states with a t_{2g} symmetry. The width of this peak is around 0.2 eV. This is determined using an absorption spectrum measured with a smaller step widths of the excitation energy, in this case 0.02 eV. The following two lines are overlapping, the peaks are located at 459.8 eV and 460.8 eV. These transitions show the properties of the 3d states with e_g symmetry. The distortion of the $[TiO_6]$ octahedra from perfect O_h symmetry to D_{4h} symmetry, causes the splitting of the e_g transition into two components ([1, 2, 70, 71, 95]).

In the L_2 region, two lines can be identified, being located at 463.3 eV and 465.7 eV. In comparison to the features in the L_3 region, the features are significantly broadened

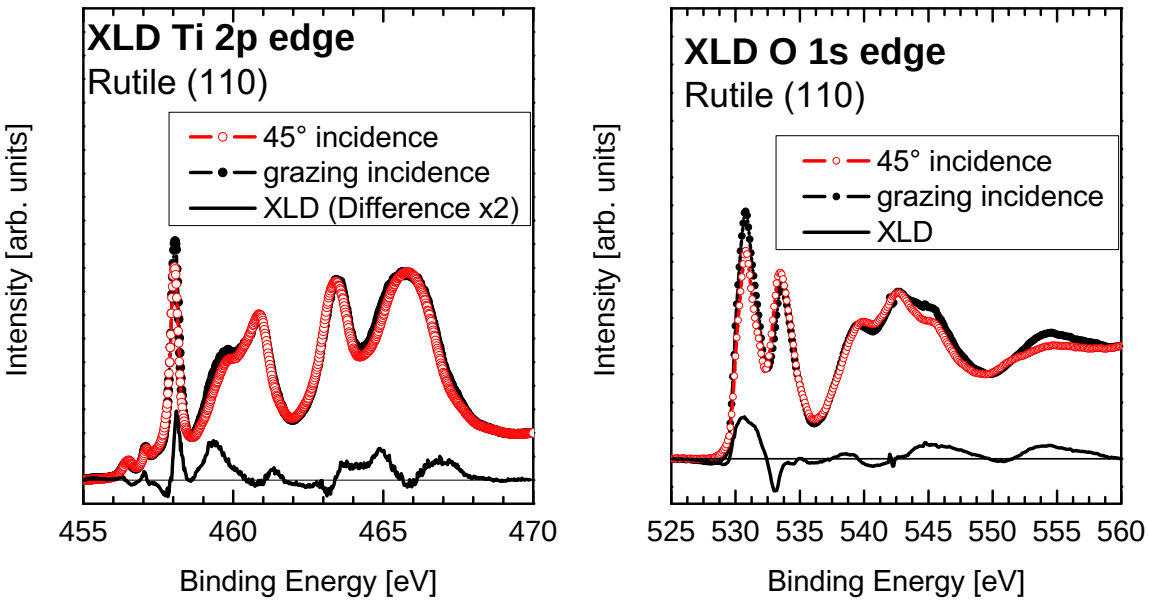

(a) XLD at Ti 2p edge

(b) XLD at O 1s edge

Figure 5.7: XLD at the Ti 2p and O 1s edges.

and the t_{2g} and e_g components exhibit stronger overlap. The XAS spectrum also shows satellite structures, similar to the photoemission lines. Due to the complex fine structure of the XAS spectrum, the separation cannot be quantified exactly, but the indicated lines in the spectrum are separated by 12.6 eV.

The O 1s XAS spectrum is shown in Fig. 5.6(b). The two main peaks arise at photon energies of 530.7 eV and 533.4 eV, resulting in a peak separation of 2.7 eV. When the photon energy is increased to higher values, three additional peaks are observed in the O 1s XAS spectrum at 539.7 eV, 542.5 eV and 545.3 eV, followed by a dip at about 549 eV. In Fig. 5.7 the XAS spectra in 45° geometry (full circles) and grazing incidence (open circles) at the Ti 2p (Fig. 5.7(a)) and the O 1s edges (Fig. 5.7(b)) are shown together with the calculated XLD signals (solid line). The thin line represents Zero. When the geometry is changed, differences in the absorption spectra become evident. The XLD signal at the Ti 2p edge shows a peak at a photon energy of 457.9 eV corresponding to the Ti $L_3 \rightarrow$ Ti 3d(t_{2g}) transitions. When the photon energy reaches 459.8 eV, a second peak in the XLD signal is visible. In the L_2 region, a difference in the t_{2g} peak is visible as well, but its intensity has decreased in comparison to the corresponding peak at the L_3 edge.

The corresponding results from the measurement at the O 1s edge in Fig. 5.7(b), show similar appearances of the spectra. In the 45° geometry, both main features have a comparable intensity i.e. the peak intensity of the second feature is about 89% of that of the first feature. In the grazing incidence geometry, the intensity of the first feature increases while that of the second feature decreases. The ratio is now about 70%. This is

reflected in the XLD signal (solid line) which has a peak at 530.7 eV. In contrast to that, it shows a dip to negative value at around 533 eV, where the intensity is higher in case of 45° geometry and a small shift is observed. In the region between 538 eV and 548 eV, minor differences in the XAS signals are observed. The spike in the XLD signal at 542 eV is an artefact of the measurement without physical meaning.

5.1.3 ResPES Rutile (110)

The ResPES datasets, covering the binding energy range from the band gap region down to binding energies of -70 eV, which also includes the Ti 3s photoemission peak at around -63 eV, are divided into two parts. This allows to focus in detail on the specified energy region. The excitation energy range is from 455 eV to 485 eV.

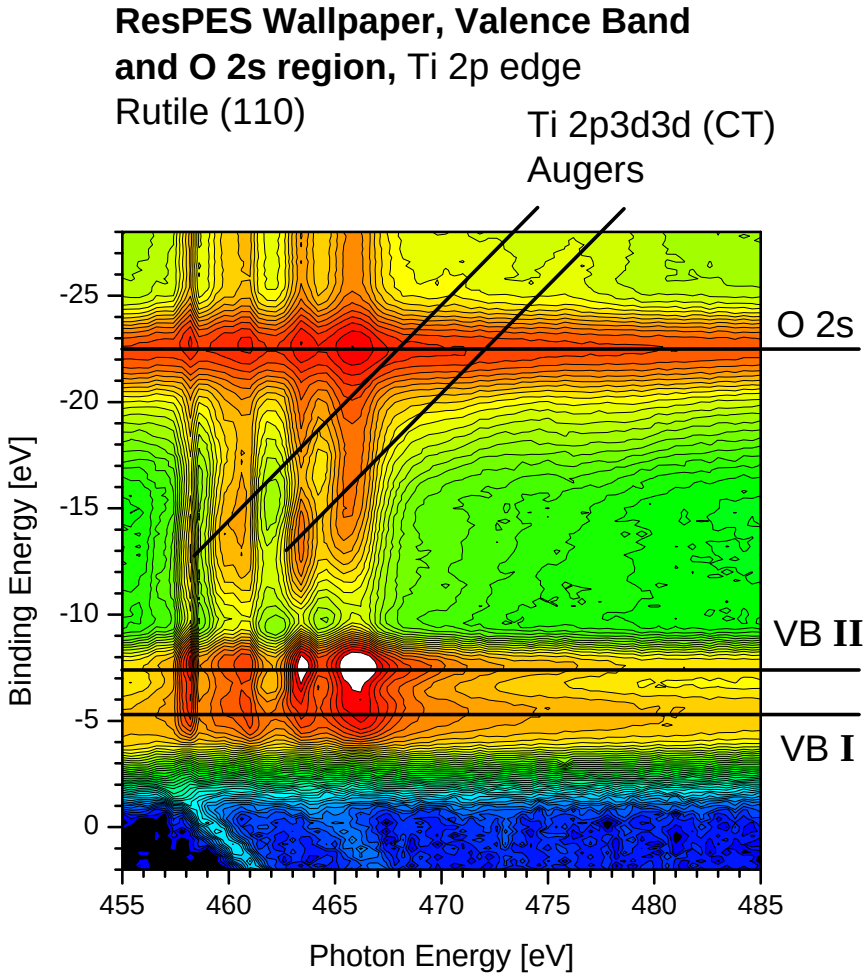

Figure 5.8: ResPES dataset (wallpaper) at the Ti 2p edge, in the energy range from 2 eV to -28 eV, covering the band gap region, the valence band and the O 2. (The two diagonal features in the gap region from top left to bottom right, crossing the Fermi-Energy (0 eV) at photon energies of around 459 eV and 465 eV are the Ti 2p core levels, excited by 2nd order light from the monochromator.)

Increased emission intensity is observed, when a photon energy of 458 eV, corresponding

to the Ti $2p_{3/2} \rightarrow$ Ti $3d(t_{2g})$ transitions is reached. Besides the increasing intensity of the two valence band features and the O 2s line, increased intensity is also observed in the binding energy range of around -13 eV. At photon energies of around 460 eV to 462 eV, reflecting the transitions Ti $2p_{3/2} \rightarrow$ Ti $3d(e_g)$, the intensity of the valence band increases again. Again, the intensity also increases in the binding energy range between the valence band and the O 2s line, but the intensity maximum is shifted to higher binding energy now, which indicates a constant kinetic energy rather than constant binding energy i.e. an Auger-like behaviour with kinetic energy of around 446 eV. The width and the weak intensity of this line only allow rough estimation of its energy. The intensity of the valence band also increases when the L_2 edge is reached. This increase is stronger in the high binding energy feature VB **II**, indicated by the intensity cut-off (white color code), than in the low binding energy feature VB **I**.
Additionally, the Auger-like feature, which is visible at the L_3 edge, also becomes visible at the L_2 edge. The Auger-like character is again proved by the shift to higher binding energy when the excitation energy is increased. The kinetic energy is around 451 eV. It also should be pointed out, that besides the contribution from the 2nd order, no changes in the band gap region are occurring.
The higher binding energy region (O 2s, Ti 3p + satellite, Ti 3s) is shown in Fig. 5.9. The scaling of the intensity is now adjusted to focus on the Ti 3p region. In the region of the absorption edge, increasing intensity is observed for the Ti 3p line. When the horizontal bar, which marks the position of the Ti 3p line, is compared with the profile lines, it can be assumed that the energy shifts to higher values when the absorption edge is reached. This is a slight charging effect as a result of the high absorption coefficient. The maximum observed shift is 0.4 eV, which corresponds to a separation of two steps of the measured energy. This is not observed in the off-resonance spectra, but the results and discussions are not affected by this. An increase of the emission intensity is also observed in the binding energy region of about -42 eV to -47 eV. When the photon energy is increased to 460 eV and 462 eV, this observed feature also shifts to higher binding energy, which indicates again an Auger channel. This line is the $L_3M_{23}V$ Auger with a kinetic energy of around 414 eV. It is not straightforward to exactly determine the kinetic energy and photon energy values, as a step width of 0.2 eV for the measurement of the kinetic energy is chosen, while the step width of the excitation energy is 0.4 eV.
When the L_2 edge at about 463 eV is reached, the $L_2M_{23}V$ Auger line appears at binding energy values between -42 eV and -47 eV, and shifts to higher binding energy values with increasing excitation energy. The kinetic energy of this line is around 420 eV, thus the difference in kinetic energy of the two auger lines is around 6 eV, which is near the value of the spin orbit split of the 2p line. It must be pointed out as well, that the intensity of the first Auger line (which has its onset at the L_3 edge) increases again at the L_2 edge. This can be seen with help of the color code, where the intensity is cut off at around

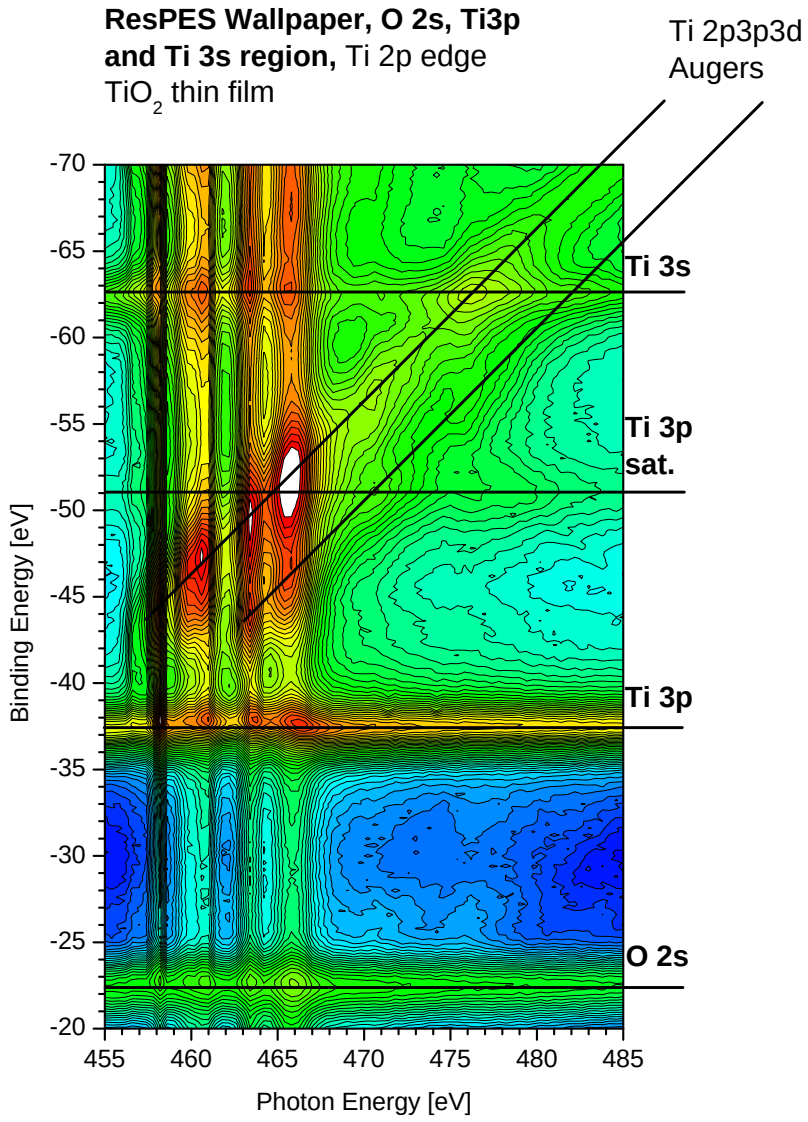

Figure 5.9: ResPES dataset of TiO_2 in the shallow core level region from -20 eV to -70 eV, covering O 2s, Ti 3p and its satellite and Ti 3s

-50 eV in L_2 region. The cut off also indicates, that the intensity is now higher than that at the L_3 edge. When the photon energy reaches 466 eV, similar properties are observed. The broader cut-off intensity indicates significantly higher intensity in this region.
When the energy region of the Ti 3p satellite is examined in detail away from the Auger region, a broad tail of higher intensity appears, similar to that of the 3p photoemission peak. The behaviour of the Ti 3s line follows closely to that of the Ti 3p line, but will not be discussed in detail. At a photon energy of about 475 eV, the L_3 Auger line and the Ti 3s photoemission peak are crossing each other as indicated by the black lines, which leads to higher intensity at this point.
The visibility of the properties of the Auger lines becomes better, when the corresponding Auger spectra are shown in their standard representation, as it is done in Fig. 5.10, to further describe the intensity ratios of the different auger channels at resonance. The

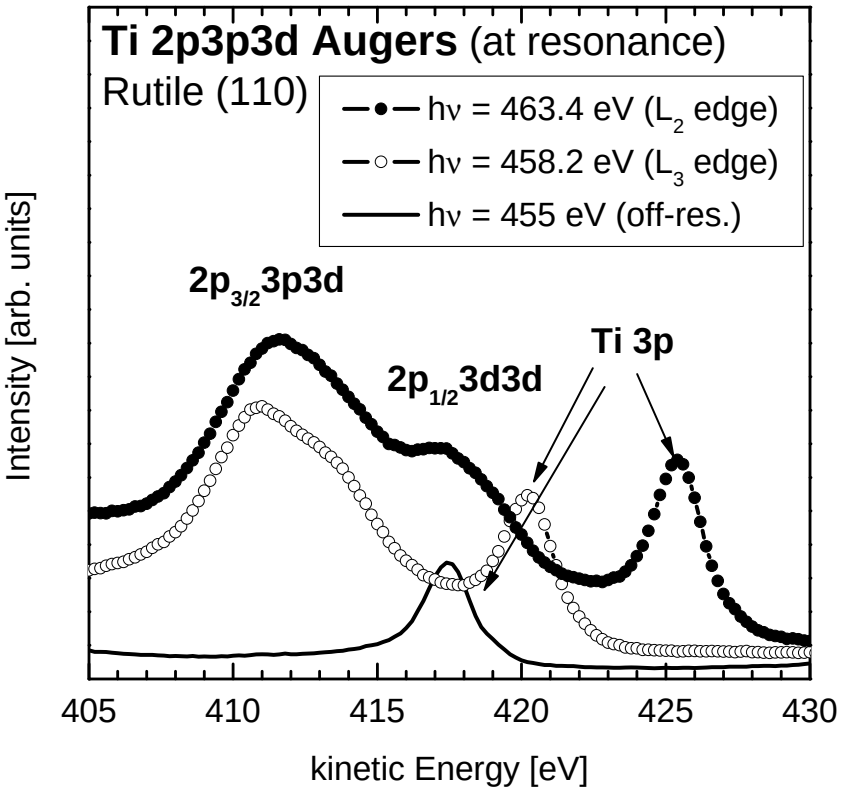

Figure 5.10: Titanium $L_{23}M_{23}M_{45}$ Augers of Rutile (110)at resonant excitations

chosen excitation energies are 455 eV (off-resonance, solid line), 458.2 eV (highest intensity at L_3, open circles), and 463.4 eV (highest intensity at L_2, solid circles). As already described above, the onset of the $L_3M_{23}M_{45}$ Auger channel is observed at around 458 eV, which leads to the appearance of the intense Auger line at kinetic energies from around 411 eV to 415 eV. At the L_2 edge, the corresponding L_2 Auger with a kinetic energy of ≈418 eV becomes visible, accompanied by intensity increase of the L_3 Auger channel. As it is already described by the full dataset, the representation of the data in Fig. 5.10 makes clear that the intensity of the $L_3M_{23}M_{45}$ Auger increases to values higher than at the L_3 edge.

The comparison of the XAS spectrum with the CIS spectra of the valence states and the Ti 3p line is shown in Fig. 5.11. The Ti 3p CIS shows good agreement with the XAS spectrum in the pre-edge region. Additionally, the sharp peak of the XAS spectrum, corresponding to the Ti $2p_{3/2} \rightarrow$ Ti $3d(t_{2g})$ transitions, is visible as well. Differences are then observed in the region of the Ti $2p_{3/2} \rightarrow$ Ti $3d(e_g)$ transitions. While there are two visible peaks in the XAS spectrum, the first one of these peaks is suppressed in the CIS spectrum. In the TEY spectrum, the intensity of the L_2 peaks is comparable to that of the first t_{2g} peak, while in the CIS spectrum the intensity in the L_2 region is significantly lower.

In contrast to this, the CIS spectra of the valence band peaks show better agreement with the TEY spectrum, although differences between both CIS spectra are evident. At first, in

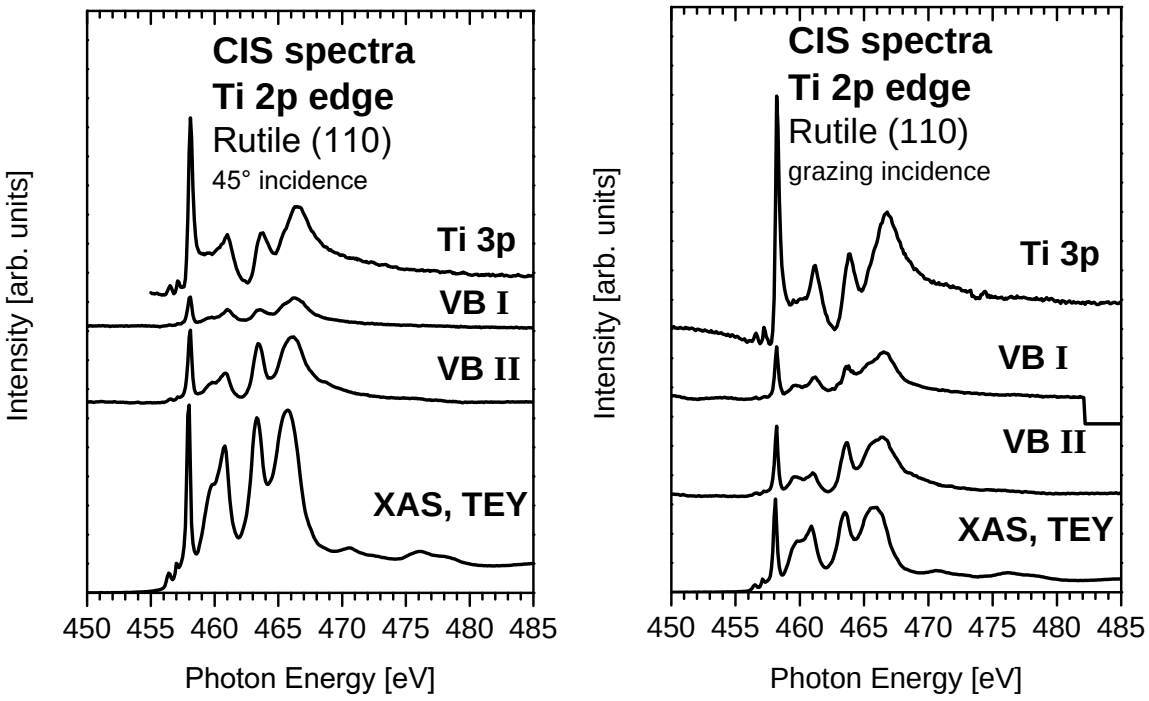

(a) 45° (b) grazing incidence

Figure 5.11: Constant initial state (CIS) spectra of Ti 3p and the valence band peaks at the Ti 2p edge. For comparison, the XAS spectrum in TEY mode is included.

both CIS spectra all features that are already known from the TEY spectrum are visible. From the full ResPES dataset of the valence band region (Fig. 5.8), it is already known that the resonance profile of both valence band features is different. This behaviour is now visible in detail, the plot of the CIS spectra shows much stronger resonance in case of the high binding energy valence band feature VB **II**. It has to be noted that none of the CIS spectra shows the satellite structures that are found in the TEY spectrum.
When the geometry is changed to the grazing incidence mode, the general appearance of the spectra remains similar. In the Ti 3p CIS spectrum, the intensity ratios of the L_2 features compared to the t_{2g} feature in the L_3 region are also different to that in the XAS spectrum. The shape of the valence band CIS spectra is very similar as well. This spectrum shows a dip, which was not seen before. The dip before resonant intensity indicates a Fano line shape. As it is the case in the 45° geometry, the behaviour at the resonance of both peaks is different. Here, the intensity of the high energy valence state is higher as well, although the difference is not as strong as in the 45° geometry. Again it has to be noted, that no satellite structures that correspond to those seen in the XAS spectrum, are visible in the excitation spectra in the grazing incidence setup.

5.1.4 Multiplet Charge Transfer Calculations

The experimental Ti 2p XAS spectrum of Rutile is shown together with three calculated spectra in Fig. 5.12. The energy axis of the calculated spectra is referenced to the energy of the experimental spectrum. The calculated spectrum are convoluted with Gaussian broadening of 0.2 eV, while the Lorentzian broadening increases from 0.2 eV to 2 eV, to allow adaption to the experiment. The bottom curve is the atomic multiplet spectrum of a Ti^{4+} ion in O_h symmetry, with 10 Dq of 1.8 eV. The main features of the experimental

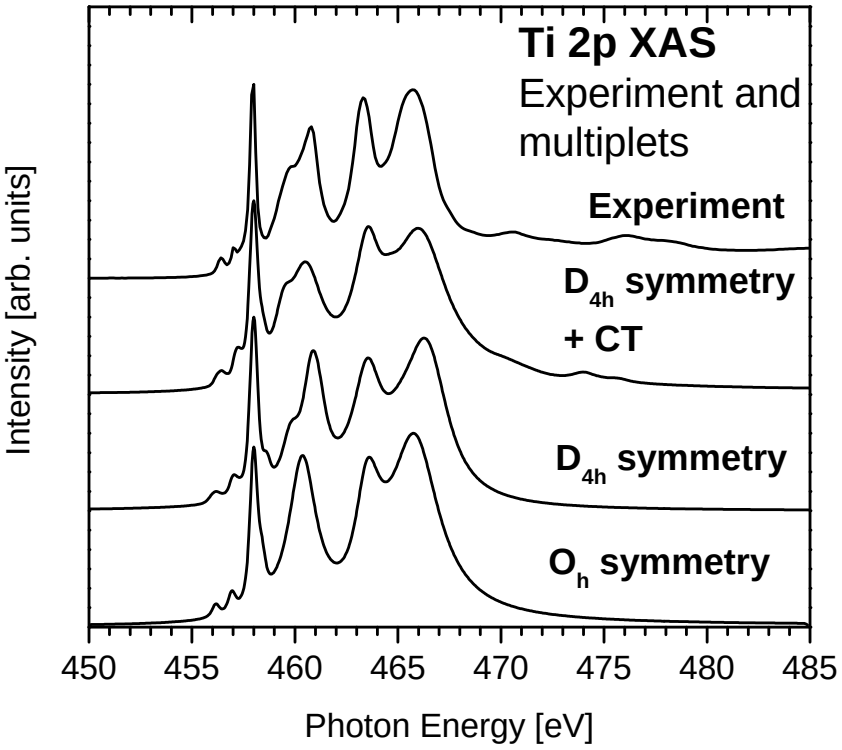

Figure 5.12: Ti 2p XAS spectra with atomic multiplets: Ti^{4+} in O_h symmetry (bottom), D_{4h} symmetry (2nd), D_{4h} symmetry + CT (3rd), experimental spectrum of Rutile (top)

spectrum are already well reproduced, except the high energy satellite structures and the splitting of the e_g component of the L_3 edge into two components.
The second spectrum is that of Ti^{4+} in D_{4h} symmetry, with $10Dq = 1.7eV$, $Dt = -0.15eV$ and $Ds = -0.1eV$. This calculation shows good agreement with the experimental spectrum, as the splitting of the e_g part is now reproduced. In contrast to this, the satellite region does not show agreement. While the experimental spectrum shows two clearly visible satellites, the calculated spectrum does not exhibit any structure in this region.
This changes, when the ligand to metal charge transfer is switched on (third curve). The calculation is carried out with a charge transfer parameter Δ of 3 eV, which leads to a weight of 66.8% $d^0\underline{L}^0$ respectively 33.2% of the $d^1\underline{L}^1$ charge transfer state in the ground state. One consequence of including the charge transfer into the calculations is an adjustment of the ligand field parameters. Now, the following values are used: $10Dq = 1.5eV$,

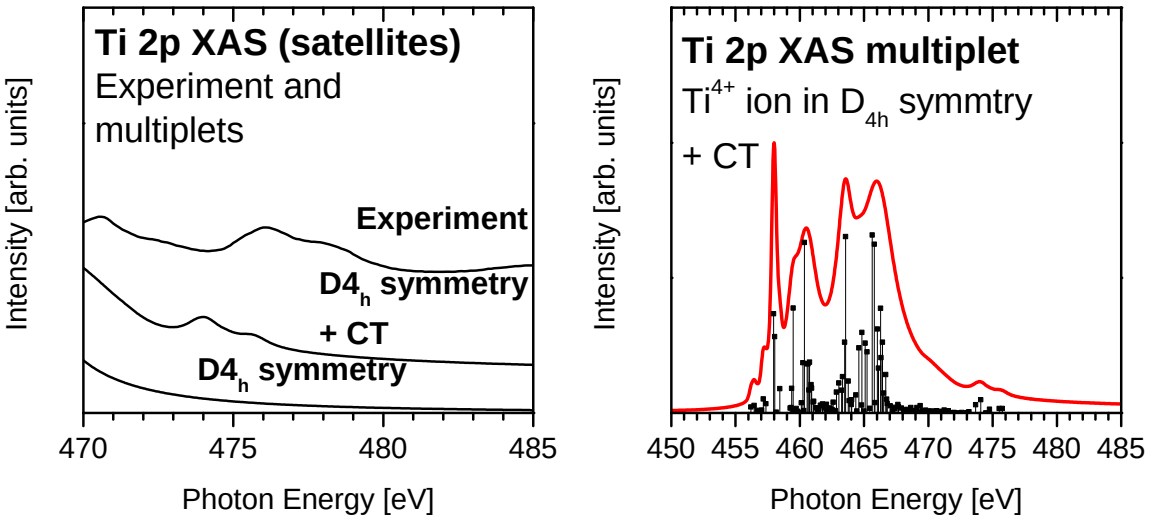

(a) Detailed plot of the satellite region of the Ti 2p XAS

(b) Calculated stick spectrum and broadened spectrum of Ti^{4+} in D_{4h} symmetry with charge transfer

Figure 5.13: Detailed plot of the satellite features. The right panel shows the broadened spectrum together with the stick spectrum.

$Dt = -0.15eV$ and $Ds = -0.15eV$. In addition to the charge transfer parameter Δ, the core hole potential U_{pd} and the d-d repulsion U_{dd} have to be included, but the influence of these parameters is mainly limited to the position of the spectrum rather than the shape. The main spectral features are well reproduced again, and additional structures in the high energy region appear. While in the experiment two well separated satellites are visible, one satellite merges with the main features of the calculated spectrum.

The detailed plot of the satellite region in Fig. 5.13(a) shows that the structure of the satellite can be reproduced as well, although there is still some discrepancy in the energy separation of the satellite feature, as the satellite in the calculated spectrum appears at lower energy in comparison to the experiment.

For completeness, Fig. 5.13(b) shows the single calculated spectrum of Ti^{4+} in D_{4h} symmetry together with the stick spectrum. Every single stick marks one allowed dipole transition. There are as much as 134 sticks.

From the parameters 10 Dq, Ds and Dt, the parameters δ_1 and δ_2 can be calculated, which allows the determination of the relative energy positions of the Ti 3d orbitals. This leads to δ_1 = -1.35 eV, which indicates reverse order of the $3d_{z^2}$ and $3d_{x^2-y^2}$ orbitals. The value of δ_2 is 0.3 eV. Together with 10 Dq, the energy level diagram as shown in Fig. 5.14 can be derived. The relative energy of the lowest subset of orbitals ($3d_{xz,yz}$ respectively e_g) is set to Zero.

The results of XPS calculations for a Ti^{4+} ion are summarized in Fig. 5.15. The spectra are referenced to a relative binding energy of 0 eV of the $2p_{3/2}$ line in order to allow comparison. The stick spectrum is broadened with a Gauss function with a FWHM of

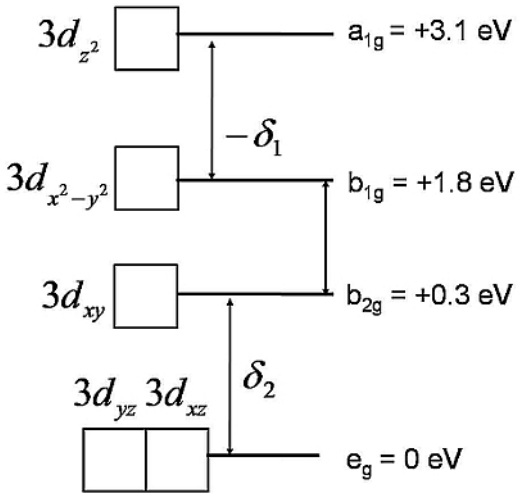

Figure 5.14: Energy level diagram for the Ti 3d states, derived from the CTM parameters 10 Dq, Ds and Dt. According to the listing in Table 3.2, the order of the a_{1g} and b_{1g} is reversed.

1.1 eV, and a Lorentz function with a FWHM of 0.1 eV. This is done with respect to the experimental result, where the observed FWHM of the Ti $2p_{3/2}$ line is 1.1 eV. In contrast to the plot program for the XAS calculations, in the XPS plot program the broadening values have to keep constant and cannot be adjusted for several energy intervals.

The bottom curve shows a calculated Ti 2p XPS spectrum in spherical symmetry with a suppressed ligand to metal charge transfer. This is achieved by choosing the charge transfer energy Δ sufficiently large to prepare an almost pure $d^0\underline{L}^0$ ground state in the calculations. In this case, the purity is better than 99.8%, and the calculation yields two peaks with an intensity ratio of exactly 2:1, and the experimental spin-orbit-split of 5.7 eV is also reproduced by the calculation.

The reduction of the local symmetry from spherical to O_h with $10Dq = 1.8eV$ (second curve) has no effect on the branching ratios between $2p_{3/2}$ and $2p_{1/2}$. The spin orbit split does not change as well.

For the third curve, the symmetry is further reduced to D_{4h} with the same D values that are used for the calculation of the XAS spectrum (Ds = Dt = -0.15 eV, 10Dq = 1.5 eV). Again, reduced symmetry has no effect on the shape of the spectrum, the result is again two lines with a branching ratio of exactly 2:1. The ligand to metal charge transfer with Δ=3 eV, leading to a contribution of 33% of $d^1\underline{L}^1$ in the ground state, is switched on in the third curve. The effect of the enabled charge transfer is only visible in the $2p_{1/2}$ region, where the broadening of the line is increased due to additional contribution of more final states. Detailed analysis of the results shows that the calculation yields 63 distinct final states, of which only four have significant contribution to the total intensity of 2 arb. units. The main peak at 0 eV contributes with 1.3 arb. units, three peaks of the $2p_{1/2}$ component contribute with 0.5 arb. units in total. The remaining intensity is distributed among the other final states. It has to be noted that the whole intensity of the

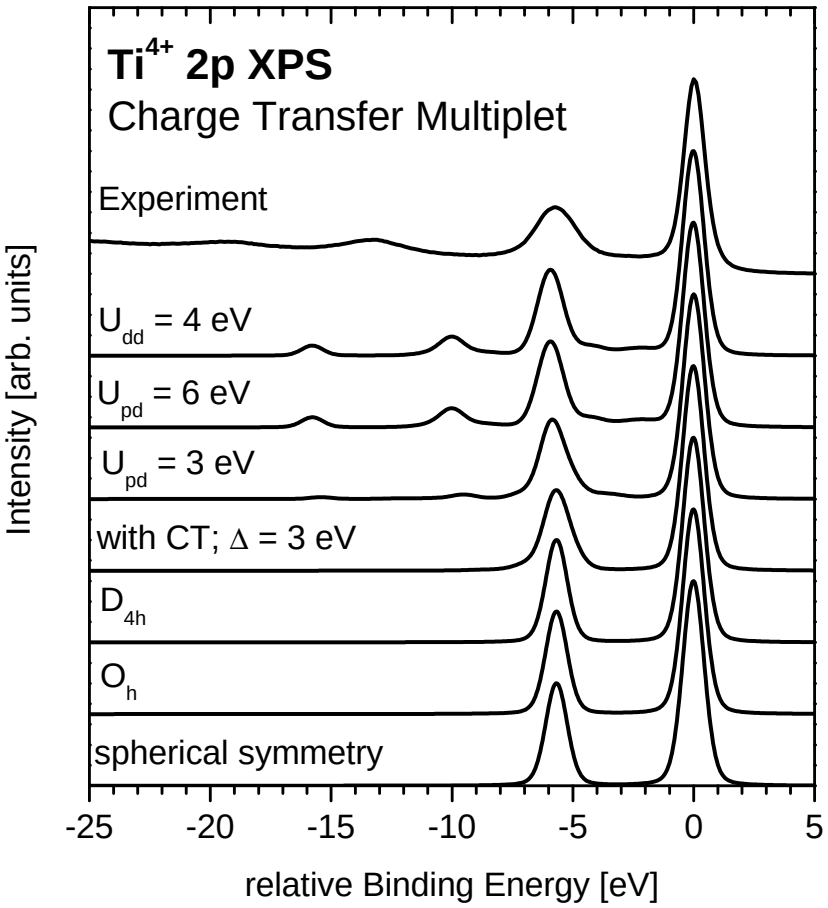

Figure 5.15: 2p core level XPS calculations of Ti^{4+}; From bottom to top: Ti^{4+} in spherical symmetry, O_h symmetry, D_{4h} symmetry, CT with $\Delta = 3$ eV, core hole potential (small), core hole potential (large), d-d repulsion

$2p_{3/2}$ line at 0 eV is caused by a single final state, while the others contribute to the $2p_{1/2}$ line and the higher energy region. The experimental spin orbit split is well reproduced. It has to be noted that the spectrum has to be broadened to achieve this, but none of the $2p_{1/2}$ final states has an energy separation of 5.7 eV to the $2p_{3/2}$ final state.
In the next step, the core hole potential U_{pd} is switched on, with a value of 3 eV. This causes additional contribution in the $2p_{1/2}$ region, visible as an asymmetry, and the appearance of two satellite structures at around -10 eV and -15 eV rel. binding energies.
In the sixth step, U_{pd} is increased to 6 eV, which shifts more intensity to the satellite lines. Additionally, the energy separation to the mainlines is increased. As a final step, the d-d repulsion U_{dd} is enabled, which means that the whole parameter set is now equal to that from the XAS calculations. In contrast to the XAS multiplet, U_{dd} has no effect on the satellite structures. In the broadened spectrum, the width of the $2p_{3/2}$ line is now 1.2 eV, while it is 1.4 eV in case of the $2p_{1/2}$ line. This is a contrast to the experimental result, where the width of the $2p_{1/2}$ is almost twice as large as the width of the $2p_{3/2}$ peak.
Additional differences are found in the satellite region, where the large experimental width is not reproduced by the calculations. The energy separations to the main lines are under-

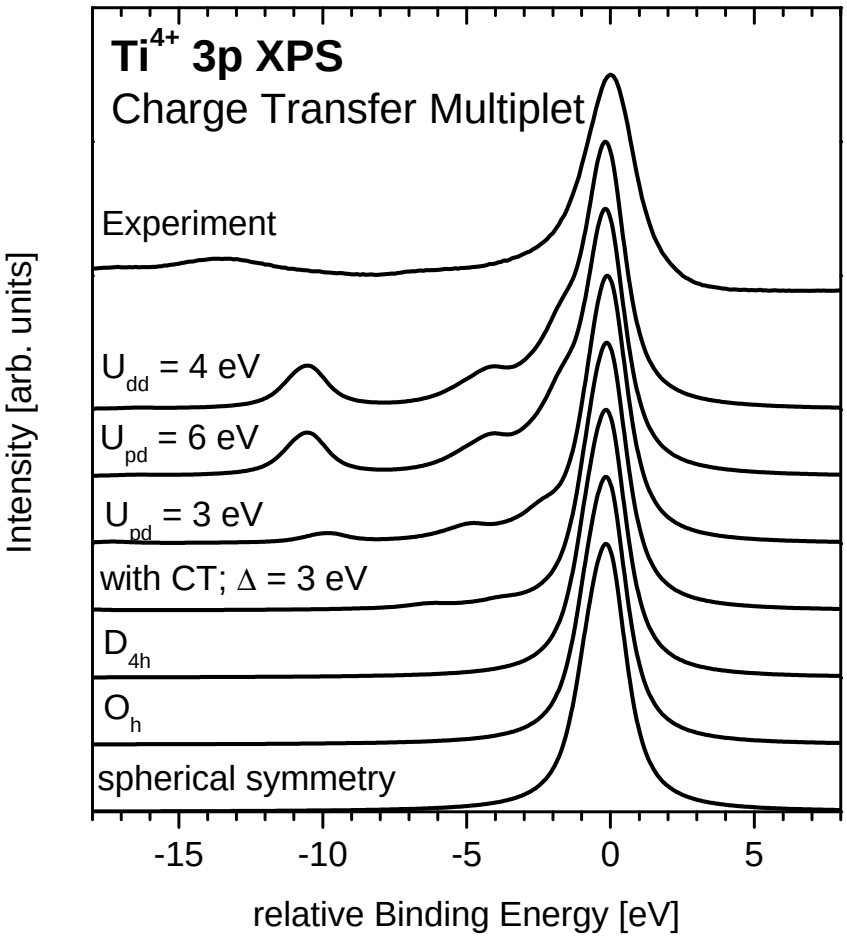

Figure 5.16: Ti 3p XPS spectra, calculated with the same parameters as the Ti 2p spectra

estimated as well. On the first view, the satellite intensities seem to be too large.
For the calculation of the 3p XPS spectra (Fig. 5.16), the same step-by-step approach as above is chosen, but a detailed description will not be carried out, as 3p XPS is equivalent to 2p XPS in the framework of the multiplet model. The calculation without a charge transfer yield the $3p_{3/2}$ and $3p_{1/2}$ final states with a spin orbit split of 0.68 eV and a branching ratio of 2:1. In contrast to this, the experimental spectrum does not exhibit any visible splitting of the main line, although the resolution is sufficient to resolve such small energy differences. Thus, the absence of a visible spin-orbit split in the Ti 3p line is an intrinsic effect of the system. When charge transfer and U_{pd} are switched on, satellite structures appear. In a first order approach, one could expect the appearance of one satellite line, as the experiment shows only one main line. In contrast to this, the results are now more complex, as the fifth curve (with charge transfer and U_{pd}) shows three visible satellite structures, at around -3 eV, -5 eV and -10 eV rel. binding energy. From the results of 2p XPS calculation it can be deduced that the last one is of the same character as the satellites observed above. This is also seen in the next step, where increased U_{pd} causes higher energy separation from the main line. In contrast to this, the low rel. binding

energy satellites are shifted towards the mainline. Such an observation is not obvious in the 2p spectra, where a possible -5 eV satellite would overlap with the $2p_{1/2}$ line due to the spin-orbit split of 5.7 eV.
Comparison with the experimental spectrum shows agreement concerning the spectral shape, although energy separation of the satellite is underestimated again.

5.1.5 Summary Rutile (110)

The overview spectrum shows negligible amounts of carbon, while the Ti 2p and O 1s photoemission peaks show reasonable agreement with published data from literature. The valence band spectra are also in agreement, although the determined position of the valence band maximum of -2.6 eV is lower than in literature. The spectral shape of the valence band shows a dependence from the measurement geometry i.e. when the setup is switched from 45° incidence to grazing incidence. Besides the observed change of the shape, a shift of 0.3 eV is detected. Additionally, the valence band spectra do not show states in the band gap region, but significant emission from above the determined valence band maximum is still observed. The valence band spectra at resonance also do not show any emission from the band gap region. Detailed analysis of the valence band spectra at resonance reveals the onset of an Auger between the valence band and the O 2s line, which is a possible Ti $L_{23}M_{45}M_{45}$ Auger, according to its kinetic energy of roughly 446 eV. The resonant Ti $L_{23}M_{23}M_{45}$ Auger spectra reveal the respective L_3 and L_2 Augers with the intensity of the L_3 Auger being higher at the L_2 edge than at the L_3 edge. The CIS spectra of Ti 3p and the valence states follow the XAS spectrum, but some deviations are detected. The CIS spectra also reveal that the resonant enhancement of the high binding energy peak VB **II** at the Ti 2p edge is stronger than that of the low binding energy peak VB **I**. Table 5.1 gives an overview of the results from photoelectron spectroscopy.

Line	binding energy	separation to Ti $2p_{3/2}$	FWHM
Ti $2p_{3/2}$	-459.3 eV	0 eV	1.1 eV
Ti $2p_{1/2}$	-465 eV	-5.7 eV	1.8 eV
Satellite A	-472.8 eV	-13.5 eV	2.6 eV
Satellite B	-478.5eV	-19.2 eV	2.7 eV
O 1s (main line, bulk sensitive)	-530.6 eV	-71.3 eV	1.2 eV
O 1s (shoulder, bulk sensitive)	-532 eV	-72.7 eV	1.7 eV
Ti 3p	-37.6 eV	421.7	2 eV
Ti 3p satellite	-51.2 eV	408.1 eV	3.8 eV
O 2p II	-7.2 eV	452.1	—
O 2p I	-4.7 eV	454.6	—
VBM	-2.6 eV	456.7 eV	—
gap state	not detected	—	—

Table 5.1: Overview of the photoelectron spectroscopy results

5.2 Titanium dioxide thin film

The preparation of the TiO_2 thin film is described in detail in the experimental section. As it is the case for the single crystalline sample, all measurements are carried out in the 45° geometry. For the measurements of the XLD signal, the grazing incidence setup is used in addition.

5.2.1 SR-PES Results

As it is the case for the single crystal, the as-prepared thin TiO_2 film shows only negligible amounts of carbon on the surface (not shown here). The 2p core level photoemission, again measured with an excitation energy of 900 eV in Fig. 5.17(a), shows all the features that are already known from the single crystal. The binding energy values are now shifted to lower values by 0.4 eV, that means the Ti^{4+} line appears at -458.9 eV now, also without contribution at the low binding energy side. The FWHM of this line is the same as in the single crystal (1.1 eV). The spin orbit split is again 5.7 eV, resulting in a peak position of the Ti$2p_{1/2}$ line at -464.6 eV. The FWHM of this peak is 1.9 eV, which is in the same range as the FWHM of the Ti $2p_{1/2}$ line of the single crystal. Again, two satellite lines are observed (now labelled A' and B'), but the separation to the main lines is reduced to

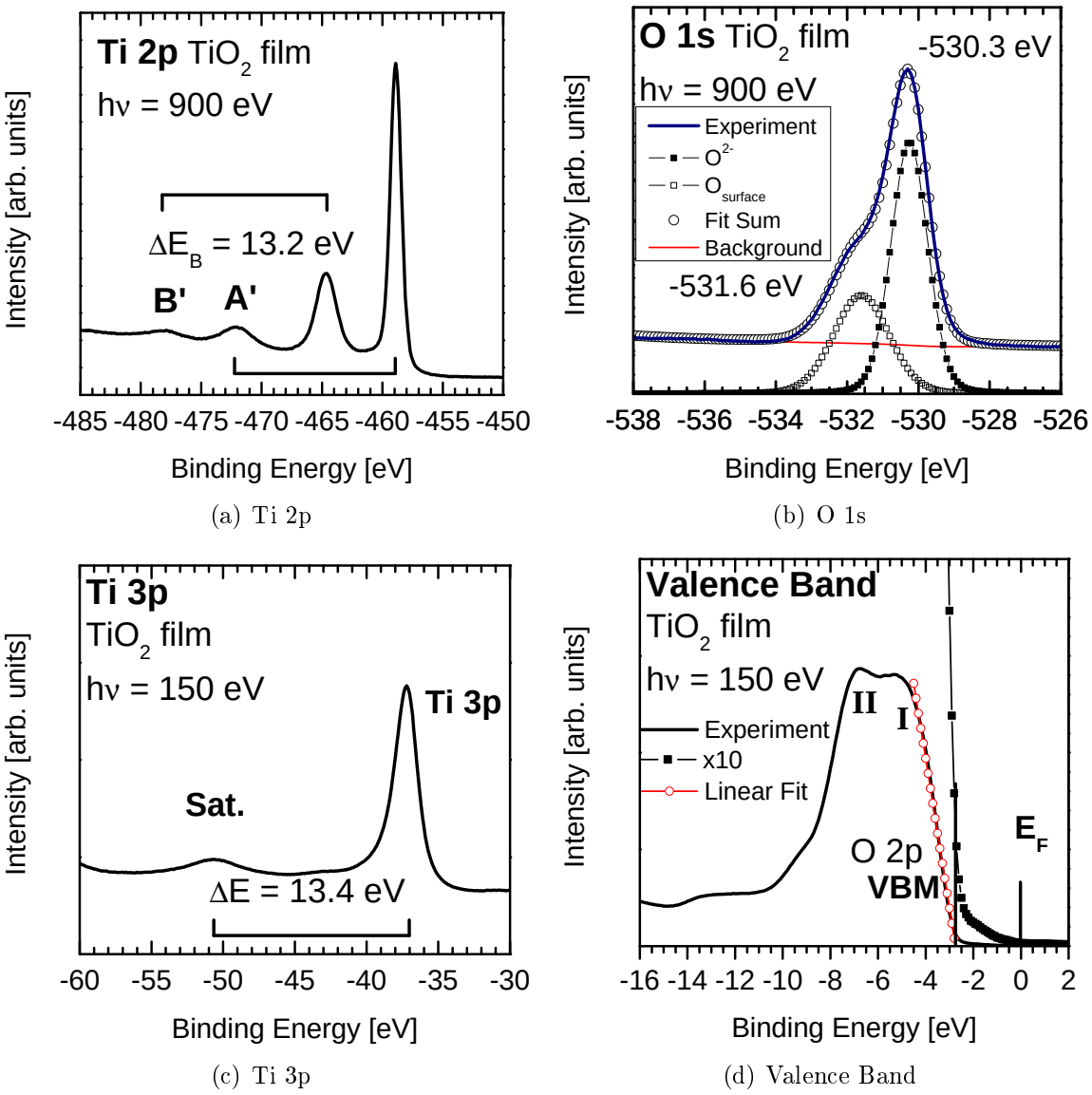

(a) Ti 2p

(b) O 1s

(c) Ti 3p

(d) Valence Band

Figure 5.17: Photoelectron spectra of Ti 2p, O 1s, Ti 3p and the valence band region of the 'as prepared' TiO_2 film

13.2 eV.

The O 1s spectrum, combined with a detailed peak analysis, is shown in Fig. 5.17(b). The main peak is located at -530.3 eV, which corresponds to a shift of 0.3 eV in comparison the the O 1s spectrum of the single crystal. The line width is 1.2 eV, which is the same value that is found for the single crystal. The shoulder at the high binding energy side is significantly higher than in the corresponding O 1s spectrum (Fig. 5.3(a)) of the single crystal (bulk sensitive measurement at $h\nu$=900 eV). The intensity ratio between the two lines is now 0.6, which is four times the value that is found in the O 1s spectrum of the single crystal.

The Ti 3p spectrum is shown in Fig. 5.17(c). The Ti 3p peak has a binding energy of -37.2 eV, which means a shift of 0.4 eV is observed in comparison to the single crystal as

well. The peak is accompanied by its satellite at -50.6 eV, corresponding to an energy separation of 13.4 eV. The width of 1.9 eV represents a negligible change to the single crystalline sample, where a width of 2 eV is found.
The valence band spectrum, excited with a photon energy of $h\nu$=150 eV, is shown in Fig. 5.17(d). Similar to the valence band of the crystalline sample, the spectrum is dominated by the broad (around 5 eV) valence band with two peaks at -6.8 eV and -5.3 eV, with the peak at the high binding energy having a slightly higher intensity than that at low binding energy. This is a contrast to the single crystal, where the peak at low binding energy has about 1.3 times the intensity of the high binding energy peak. Again, a linear fit (open circles) of the upper valence band edge is used to determine the valence band maximum, which is found at -2.75 eV. Another difference is the clearly pronounced valence band edge, which is not observed in this way in the single crystalline sample.
The magnified plot of the valence band (factor of 10; thin line with squares), shows the in-gap emission in more detail. Instead of a pronounced and clearly visible band gap state at around -0.7 eV as found in [1, 96], the as-prepared thin film only shows a broad emission without visible peaks.

5.2.2 XAS and XLD Results

The Ti 2p XAS spectrum of the thin film (in TEY mode) is shown in Fig. 5.18(a). Clear differences in comparison to the Rutile XAS spectrum are found. The pre-edge peaks at photon energies of 456.4 eV and 457.2 eV are smeared out in comparison to the Rutile XAS spectrum, while the position and width of the first sharp peak at 457.9 eV remains the same. In contrast to this, the properties of the following double peak structure are changing. The peaks appear now at photon energies of 459.6 eV and 460.4 eV (Rutile: 459.8 eV and 460.8 eV), and the intensity ratios change as well. In the thin film, the first one of the double peak shows higher intensity, while this is vice versa in the corresponding XAS spectrum of the Rutile crystal. In agreement with the Rutile XAS, only two peaks are observed in the L_2 part of the spectrum. In the XAS spectrum of the TiO_2 film, these peaks appear at photon energies of 463.3 eV and 465.7 eV, which are the same position as for Rutile. In the thin film, the e_g peak at the L_2 edge is higher than the corresponding t_{2g} peak, while in Rutile both peaks have the same height, with the t_{2g} peak at the L_3 edge being the highest peak in the spectrum. In the film, the e_g peak at the L_2 edge is the most intense line. As it is the case in the XAS spectrum of Rutile, satellite lines are observed as well. The separation is reduced to 12.4 eV, as indicated in the figure.
Comparison with the XAS results from section 5.1.2, as well as comparison with the literature [1, Fig. 33] makes clear, that the measured spectrum is not that of Rutile, but the agreement with the XAS spectrum of Anatase, which is shown by Diebold [1, Fig. 33] is poor as well. Better agreement is found with the results from J.H. Richter et al. [97]

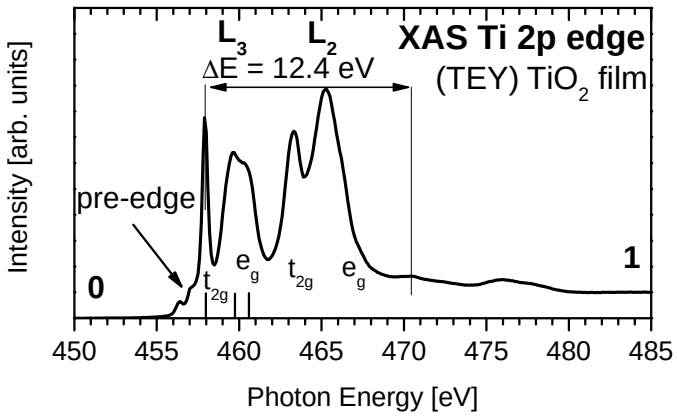

(a) XAS at Ti 2p edge

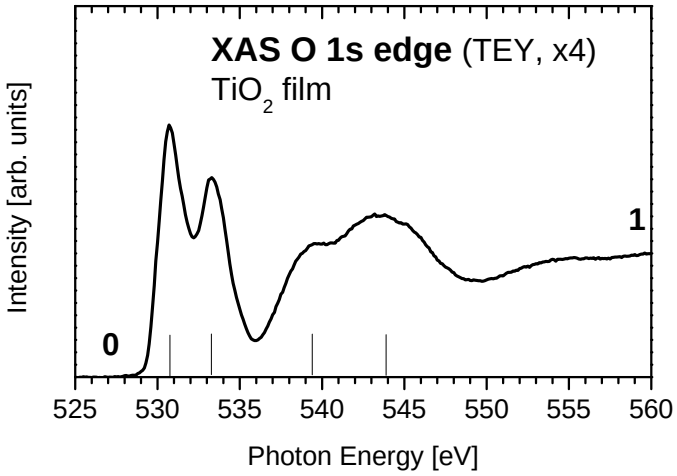

(b) XAS at Ti 2p edge

Figure 5.18: XAS spectra in TEY mode, at Ti 2p edge (a), and O 1s edge (b), normalized to an edge jump from 0 to 1 i.e. absorption per atom

as well as the results published by Brydson et al. [98], although the latter one presents EELS results instead of XAS results. The results from Thomas et al. [73] (measurements performed in Auger yield mode) also show better agreement as well as the results from Ruus et al. [99].

The XAS spectrum at the O 1s edge is shown in Fig. 5.18(b). Although the general appearance is similar to the XAS spectrum of Rutile, differences are visible. The two main peaks are observed at photon energies of 530.7 eV and 533.3 eV, resulting in a separation of 2.6 eV. The broadening of these two lines is stronger than that of the main peaks of the Rutile XAS, resulting in a stronger overlap of both lines. The peak positions in case of the Rutile crystal are 530.7 eV and 533.4 eV, which means that only negligible energy shift occurs. As it is the case for the single crystal, there is an intensity dip at 536 eV, followed by a broad peak with a width of about 12 eV from 537 eV to 549 eV. In contrast to the Rutile XAS, only two broad structures appear at 539.4 eV and 543.8 eV, while the corresponding spectrum of Rutile shows a structure with three peaks in this

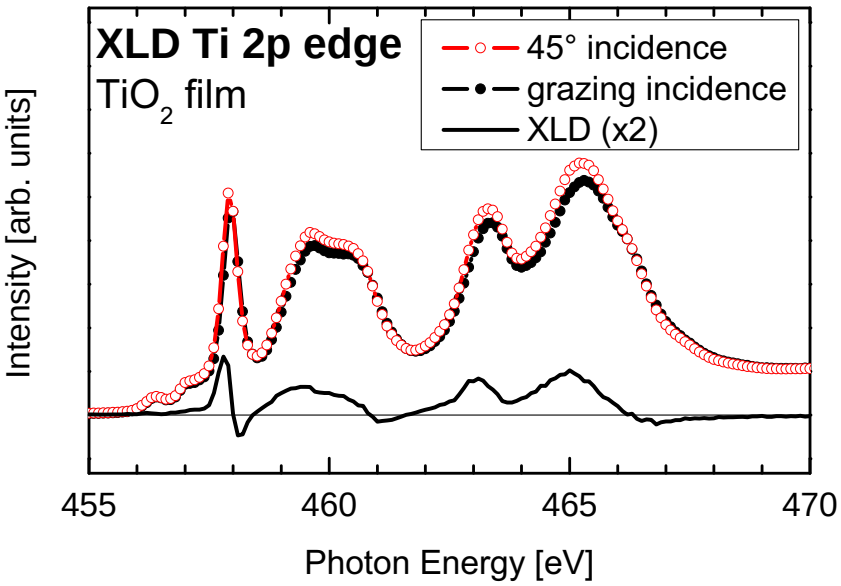

Figure 5.19: XLD at the Ti 2p edge

energy range. It is possible to discuss the visible shoulder at 542.3 eV as a third peak, which strongly overlaps with that one at 543.8 eV. The spectral shape of the O 1s XAS shows good agreement with the results of experiments in which Anatase was used, as shown in [73, 98, 99, 100] (in [100], the results from Brydson et al. [98] are compared to theory). It has to be noted, that again different experimental methods, like EELS and XAS in Auger yield, were applied, but a general comparison is reasonable.
The XLD of the TiO_2 film at the Ti 2p edge is shown in Fig. 5.19. In contrast to the results obtained from the crystalline sample, the intensity of the e_g part of the spectrum is higher in the 45° geometry. In order to receive a positive XLD signal, the calculation is now done in opposite way to the crystalline sample. In the energy range of the pre-edge structures, the XLD signal remains near Zero, while in the range of the t_{2g} peak in the XAS spectra, a peak in the XLD is observed as well.

5.2.3 ResPES Results

As it is done in the section 5.1.3, the full resonance photoemission dataset will be divided into two parts, allowing better visibility of the specified energy regions. At first, the valence band and O 2s regions are shown in Fig. 5.20. Similar to the crystalline sample, the 2nd order contribution is crossing the band gap region. In contrast to the first one, now in addition a resonance in the gap region is visible. It starts at photon energy of around 456 eV and thus appears at lower photon energies than the pre-edge structures in the XAS spectrum, that showed up at 456.4 eV and 457.2 eV. The binding energy of the observed Ti 3d gap state is -0.7 eV.
This gap was reported several times in the literature. Batzill et al. [96] found this gap

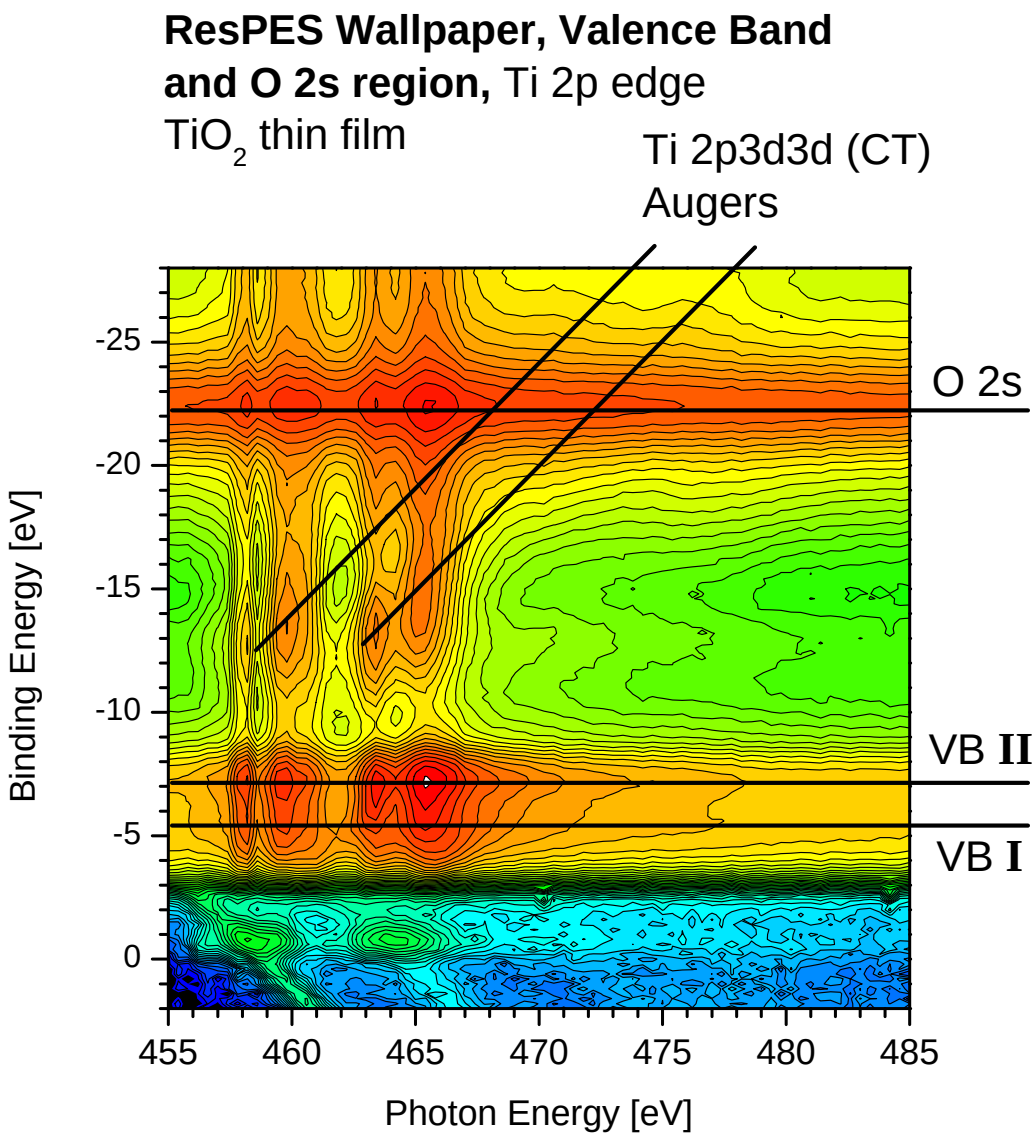

Figure 5.20: ResPES dataset of TiO_2 film at Ti 2p edge, binding energy region from the valence band down to the O 2s emission

state in both Rutile and Anatase samples at binding energy values of around -0.8 eV in off-resonance photoemission, while Prince et al. [69] found this state in similar binding energy position in resonance photoemission. The resonance of the gap state is significantly broader (5 eV) than the 2nd order contribution, which has a width of around 1 eV. Thus, a discussion of the properties of the in-gap state is still possible without calculating a correction for the 2nd order contribution.

The valence band also shows resonant enhancement of the intensity when the Ti 2p edge is reached. It can be clearly seen, that the resonance behaviour is different for both valence band peaks. The color code helps to emphasize the fact that the high binding energy peak of the valence band at around -7 eV shows the higher intensity in comparison to the low binding energy feature. The highest intensity is reached at a photon energy of 466 eV, which is indicated by the cut-off.

As it is observed in case of the Rutile sample, Auger-like features appear at the resonance in the binding energy region between the valence band and the O 2s peak. The Auger-like character of these features is evident, as both lines shift to higher binding energies when the photon energy is increased.

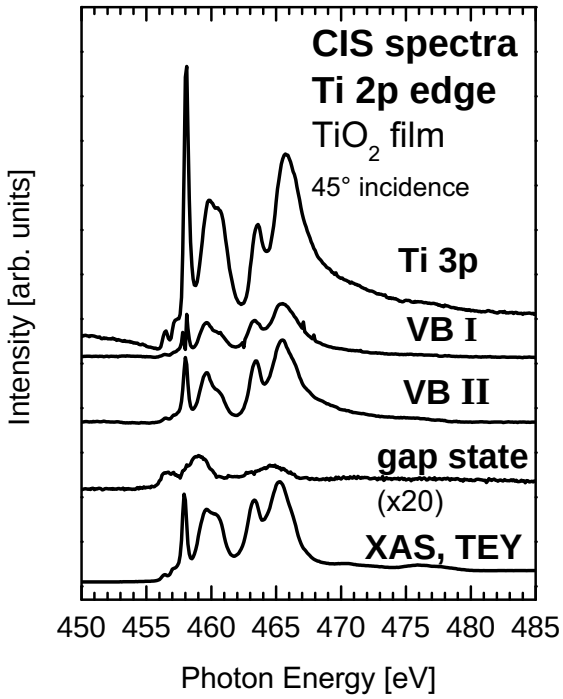

Figure 5.21: Constant initial state (CIS) spectra of Ti 3p, the valence band peaks and the gap state at the Ti 2p edge. For comparison, the XAS spectrum in TEY mode is included.

In Fig. 5.21 the excitation spectra of Ti 3p and the valence states together with the XAS spectrum are shown. Additionally, the CIS spectrum of the Ti 3d gap state is shown. For this plot, the procedure to subtract the contribution of the 2nd order is applied. The CIS spectrum of the Ti 3p line shows better agreement with the XAS spectrum than in case of the corresponding spectra of the single crystal. All features that are found in the TEY spectrum are now found in the Ti 3p CIS, although the intensity ratios are different.
The properties of the valence band CIS spectra are comparable to those from the single crystal. Again, the intensity at resonance is higher for the valence state VB **II** with higher binding energy than the state with low binding energy. The CIS spectrum of the low binding energy valence state shows some spikes, which are experimental artefacts, but do not influence the discussion of the results.
While the CIS spectra of the valence band and Ti 3p follow the shape of the TEY spectrum with reasonable agreement, the CIS spectrum of the Ti 3d band gap state shows significant differences. The onset of the gap state spectrum is shifted to lower photon energy of around 456 eV. In contrast to the XAS spectrum, no sharp and pronounced fine structure are found in the CIS spectrum of the gap state. The satellite structures from the XAS spectrum are also not reproduced in the CIS spectra of the thin film.

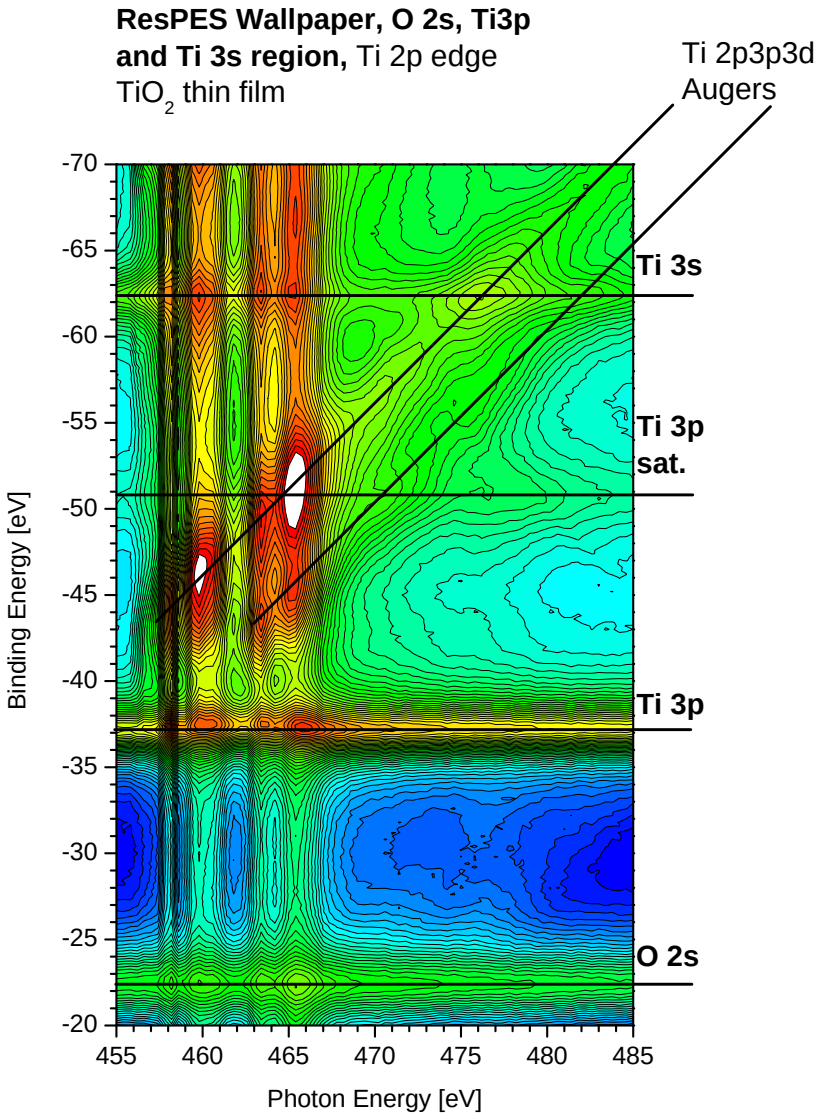

Figure 5.22: ResPES dataset of TiO_2 film at Ti 2p edge, binding energy region from O 2s, Ti 3p and satellite, and Ti 3s

The ResPES dataset of the higher binding energy region (Fig. 5.22) is very similar to that of the crystalline sample. As above, the Ti 3p intensity increases when the absorption edge is crossed. At a photon energy of 458 eV, the Ti $L_3M_{23}V$ Auger feature appears at a binding energy of around -44 eV, resulting in a kinetic energy of 414 eV. The highest intensity is reached at around 460 eV photon energy. The intensity drops down, but increases again when the L_2 edge is reached at around 464 eV. At this photon energy, the $L_2M_{23}V$ Auger with a kinetic energy of 420 eV appears. When the excitation energy is 466 eV, the intensity of the L_3 Auger increases again. In the binding energy region of the Ti 3p satellite at -51 eV, a tail with higher intensity is observed. A discussion of this is not straightforward, because in this energy range the Auger contribution has to be considered. Additionally, resonant ResPES datasets were recorded at the Ti 3p edge as well. This is shown in Fig. 5.23. The dataset starts with the valence band spectrum

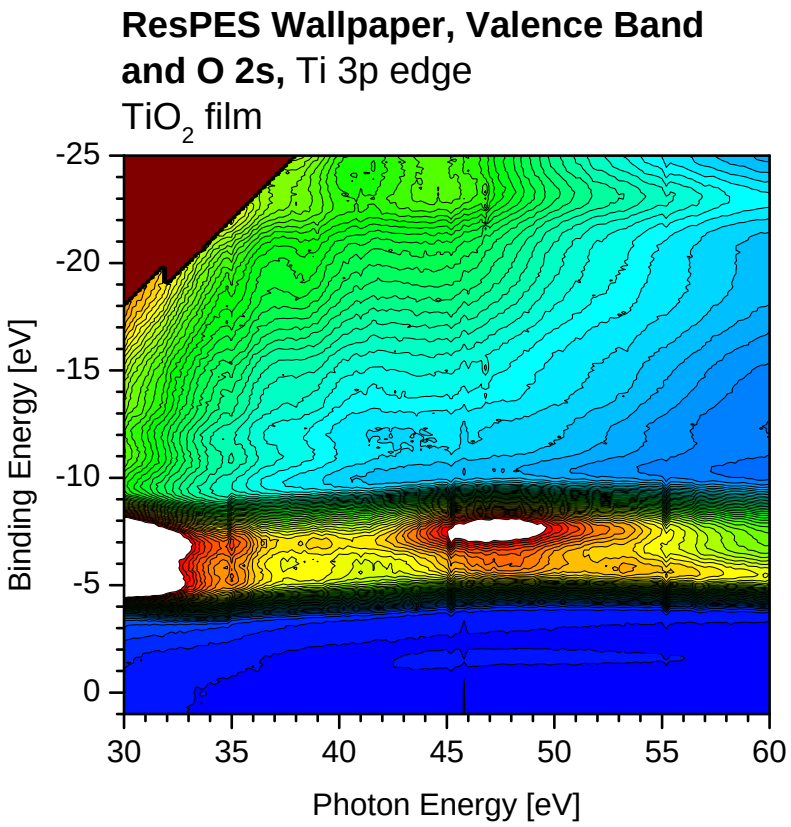

Figure 5.23: ResPES dataset of TiO_2 film at Ti 3p edge, binding energy region from the valence band down to the O 2s emission

recorded with a photon energy of 30 eV. The blank region from -18 eV to -25 eV is not measured and thus set to Zero. The high intensity in the valence band on the low energy side is caused by the O 2s resonance. The intensity of the valence band region is cut-off in the range from -4.5 eV to -8 eV for better visualization.

When the excitation energy corresponding to the Ti 3p binding energy (37 eV) is reached, a clear drop of the valence band intensity is visible. This extends up to a photon energy of 42 eV, where the valence band intensity increases. It is visible, that the high binding energy part of the valence band increases stronger than the low energy part, which was also observed in the 2p resonant photoemission. This is clearly visible in the energy range from 45 eV to 50 eV, where this intensity is cut-off, while the low energy part of the valence band is not, which proves its significantly lower intensity.

When the excitation energy further increases, the behaviour of the two valence band features is still different. The intensity of the high energy feature decreases rapidly between excitation energies from 50 eV to 60 eV, while the low energy feature decreases slower with increasing photon energy. In contrast to the observations made at the Ti 2p edge, no Auger-like features are observed in the binding energy range around -13 eV. The second significant difference is the fact that the emission intensity decreases at the Ti 3p edge, while it increases at the Ti 2p edge.

The highest intensity around the Ti 3p edge is observed between excitation energies from 45 eV to 50 eV, which is significantly higher than the nominal Ti 3p edge, which is expected to occur around 38 eV.

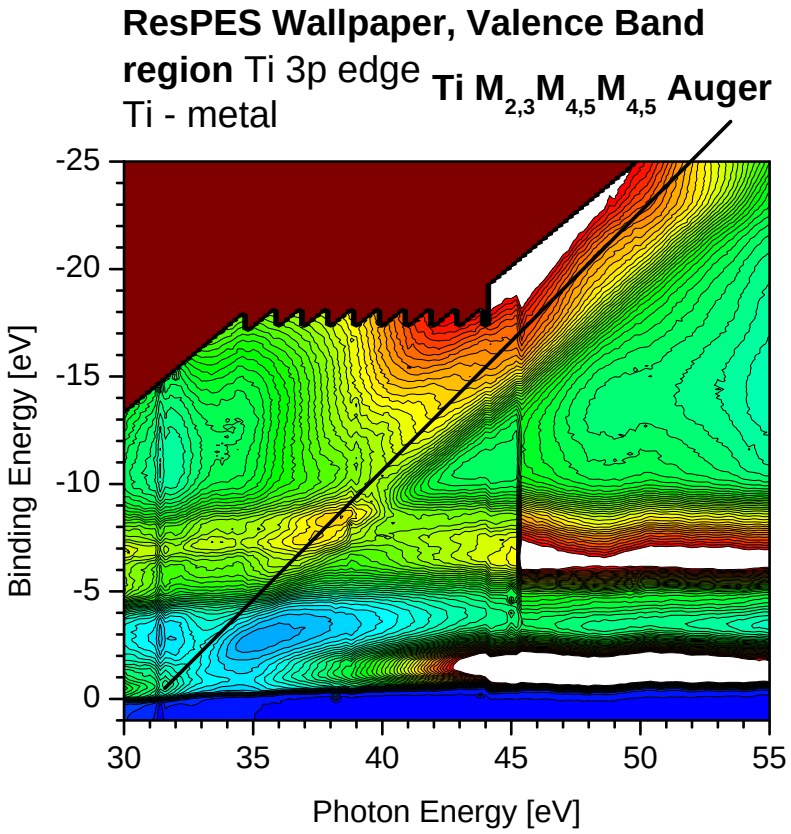

Figure 5.24: ResPES dataset of Ti metal film at Ti 3p edge, binding energy region shows Ti 3d, TiO_2 valence band and O 2s (due to oxygen adsorption)

The ResPES dataset of a metallic film is shown in Fig. 5.24. The binding energy of the 3p line in titanium is -32.7 eV. This is determined by PES measurements of a deposited film before oxidation. Although the film was kept in UHV conditions with a pressure of better than 10^{-9} mbar, it already shows significant uptake of oxygen during a time of around six hours. Nevertheless, this dataset is reasonable to show differences and similarities to the oxide. The low excitation energy part (30 eV) does not show such high intensity as in case of the oxide film. The Ti 3d emission close to Zero binding energy decreases when the photon energy increases, until 32 eV are reached. Here, the intensity increases, but immediately drops down again above 32 eV. This is the onset of the Ti $M_{2,3}M_{4,5}M_{4,5}$ Auger with a kinetic energy of $\approx$ 31 eV. This line is clearly visible at fixed kinetic energies due to the shape of the profile lines of equal intensities. Additionally, it is emphasized by the bold diagonal line across the dataset.
Between 32 eV and 36 eV, the 3d intensity shows a dip, while it increases again at excitation energies higher than 36 eV. The maximum intensity is observed at photon energies above 45 eV, which is indicated by the cut-off.

The discussion of the following features is not straightforward, as the measurement of this dataset is interrupted by the injection, which is visible as a kink in the O 2p valence band emission between excitation energies from 45 eV to 46 eV. Although an I_0 normalization is applied to the spectra, this artefact cannot be completely removed. In contrast to this,

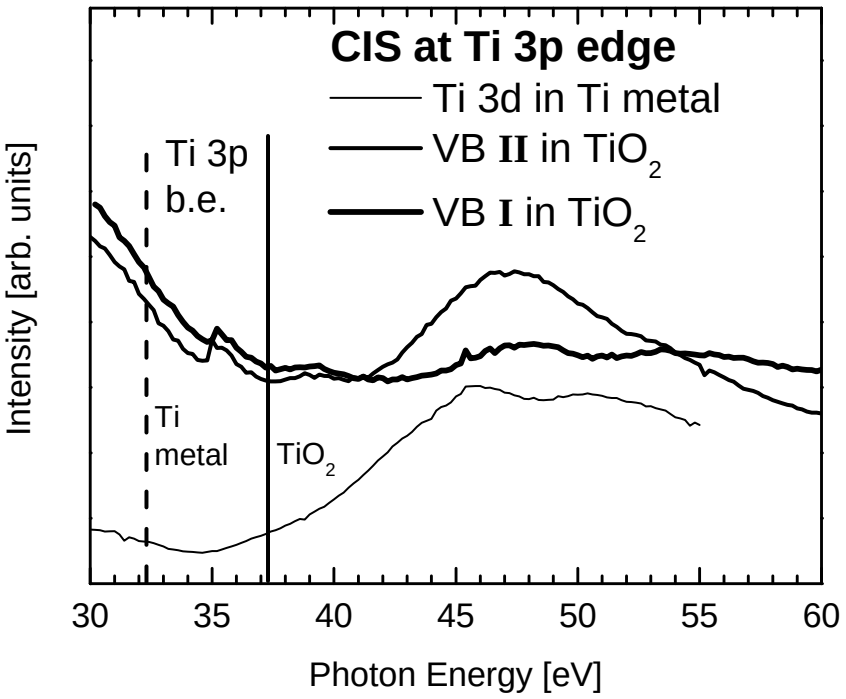

Figure 5.25: CIS spectra of Ti 3d in titanium metal (thin curve), and the two valence band peaks in TiO_2 (medium and bold curves, measured at the Ti 3p edge

the Ti 3d CIS spectrum, thin line in Fig. 5.25, does not show a kink due to the injection, which proves the correctness of the normalization procedure. On the other side, this also shows the rapidly increasing oxygen content. The CIS spectrum also shows that the maximum emission intensity is not reached at the expected value which would correspond to the Ti 3p binding energy of around -32 eV (marked by the vertical dashed line), but occurs at significantly higher excitation energies between 45 eV and 55 eV. The CIS spectrum reveals two broad peaks at excitation energies of roughly 46 eV and 51 eV. In contrast to this, the onset of the Auger line is located at the expected photon energy of around 32 eV.

The CIS spectra of the valence band features (medium and bold lines) start at significantly higher emission intensity than the Ti 3d CIS, but also show decreasing intensity, as was already stated above. In this dip region, small fine structures become visible between 35 eV and 36 eV, which is significantly lower than the binding energy of Ti 3p in TiO_2. This energy position is marked by the solid line. Above this edge, only features with low intensities at around 40 eV are observed, before the intensity then increases until its maximum value at photon energies around 47 eV is reached. As it was the case for the valence band CIS spectra at the Ti 2p edge, the spectral shape of both spectra differs

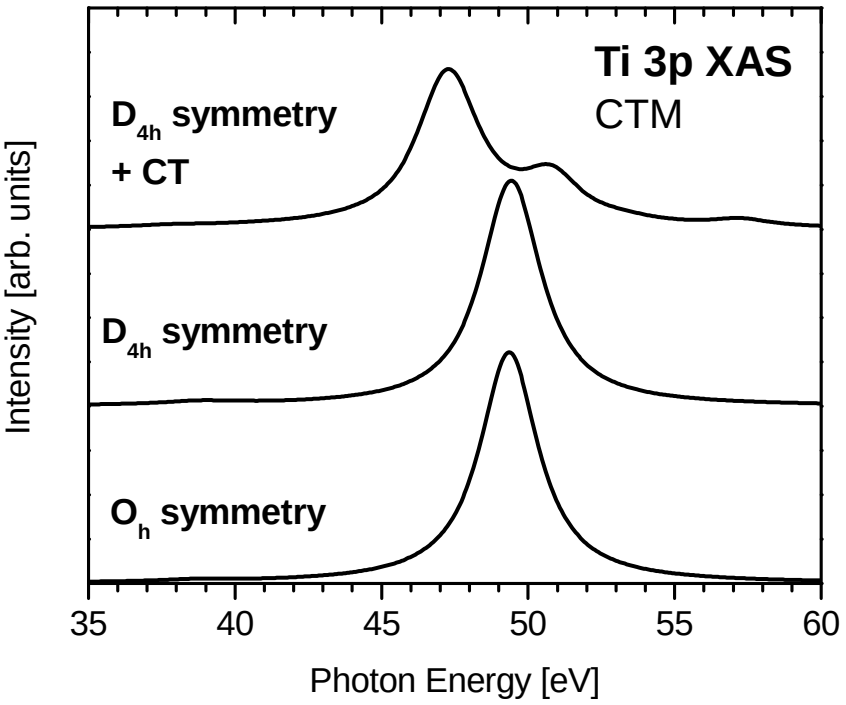

Figure 5.26: Multiplet calculations at the Ti 3p edge. For the Ti^{4+} ion, the same crystal field parameters as for the Ti 2p calculations are used.

from each other. It has to be pointed out that there is almost no energy shift of the maximum emission intensity of Ti 3d in the metal and the valence band in the in case of TiO_2 respectively. Additionally it has to be pointed out, that there are fine structures in the CIS spectra of the valence band at the Ti 3p edge, but the shape is not comparable with those from the Ti 2p edge, although both processes involve n-p $\rightarrow$ 3d transitions with the same symmetries.

5.2.4 Multiplet Charge Transfer Calculation

The calculations of a 2p XAS spectrum in order to fit the corresponding spectrum of the thin film did not lead to reasonable agreement. One reason is the rather complex distortion of the Anatase-[TiO_6] octahedron, on the other side it is not clear if the thin film is composed of pure Anatase or a mixture of Rutile and Anatase. The latter case would be more likely. Thus, the CTM calculation are limited to a qualitative simulation of the observations in the Ti 3p resonant photoemission experiment.
As an XAS spectrum in the TEY mode at the Ti 3p edge is missing, the CIS spectra at the valence states are used in order to represent the XAS spectrum. The good agreement between TEY and the CIS spectra of O 2p **I** and O 2p **II** were already shown before. This justifies such a qualitative comparison.
In Fig. 5.26, the same series of CTM calculations as in case of Rutile at the Ti 2p edge (Fig. 5.12) is shown. The spectra are Lorentz broadened by 2.4 eV FWHM and a Gaussian with

0.1 eV. The spectra are not shifted, as no prominent feature is found in the experiment. The calculation starts with Ti^{4+} in O_h symmetry, with 10 Dq = 2 eV (bottom). The broadened spectrum shows one dominating peak at 49.3 eV, with an intensity of 1.98 arb. units, while the total intensity is 2 arb. units. Any additional contribution is barely visible in the broadened spectrum, which results in a completely different spectral shape as in case of the 2p-3d calculations, despite the same symmetry of the transitions. The intensities of these additional feature are 3 orders of magnitude lower than the intensity of the dominating peak. This result differs significantly from the corresponding one at the Ti 2p edge, where all transitions are well pronounced.
In the middle curve, the symmetry is reduced to D_{4h}, with 10 Dq = 1.7 eV, Dt = -0.15 eV, and Ds = -0.1 eV, as it is the case for the 2p-3d CTM of Rutile in Fig. 5.12. In contrast to the previous result, the CTM at the 3p edge does not show visible changes, although the number of lines increases to as much as 20. The major part of the total intensity (2 arb. units) is found in two lines at 49.3 eV and 49.6 eV, with 1.97 arb. units in total. The low separation prevents visibility of this small split. This is again a significant difference to the 2p-3d XAS calculation, where symmetry reduction from O_h to D_{4h} caused well visible changes of the spectral shape. It has to be pointed out that with reduced broadening the increased number of lines becomes visible. In the top curve, the CT is switched on, with $\Delta = 3\ eV$, U_{dd} = 4 eV and U_{pd} = 6 eV, which increases the number of lines to 118. As a result of the core hole potential U_{pd}, the mainline shifts to lower energies. In the 2p-3d CTM, the influence of the core hole potential was neglected by referencing the spectra to the remarkable feature in the experimental 2p-3d XAS. Additionally, satellite structures become now visible, as it is the consequence of the enabled CT at the Ti 2p edge. It may be argued that it is not reasonable to use the same values for U_{pd} in case of a 2p and a 3p core hole, but the main intention of this calculations is to get a qualitative insight into the influence of the respective parameters. For this, an adaption of the 2p parameters for the 3p parameters is reasonable anyway.
Similar to the experiment, the highest intensity is observed at around 50 eV, which is well above the ionization energy of the 3p line. The Cowan code calculates the energy of the $3p^5 3d^1$ configuration to 37.3 eV, with a spin orbit split of 0.4 eV. This shows that the high energy for the maximum intensity is not an artefact of an improper calculation of the energies.

5.2.5 Summary Titanium dioxide thin film

The photoemission results of the TiO_2 thin film do not differ too much to that of the Rutile single crystalline sample. The differences are mainly found in the binding energy positions of the photoemission peaks. In contrast to the single crystalline sample, the thin film exhibits a band gap state, which becomes visible at resonance. Additionally, the

high energy component of the O 1s has higher intensity in case of the thin film. The PES results are briefly summarized in Table 5.2.

Line	binding energy	separation to Ti $2p_{3/2}$	FWHM
Ti $2p_{3/2}$	-458.9 eV	0 eV	1.1 eV
Ti $2p_{1/2}$	-464.6 eV	-5.7 eV	1.9 eV
Satellite A'	-472.1 eV	-13.2 eV	2.7 eV
Satellite B'	-477.8eV	-18.9 eV	2.9 eV
O1s (main line)	-530.3 eV	-71.4 eV	1.2 eV
O1s (shoulder)	-531.6 eV	-72.7 eV	1.7 eV
Ti 3p	-37.2 eV	421.7 eV	1.9 eV
Ti 3p satellite	-50.6 eV	408.3 eV	3.7 eV
O 2p II	-6.8 eV	452.1 eV	—
O 2p I	-5.3 eV	453.6 eV	—
VBM	-2.75 eV	456.15 eV	—
gap state (at resonance)	-0.7 eV	458.2 eV	

Table 5.2: Overview of photoelectron spectroscopy results of TiO_2 thin film

5.3 Chromium deposited on titanium dioxide film

In this section, an overview on the results of chromium deposition on TiO_2 thin film will be given. It starts with the photoemission results of the core levels (Ti 2p, O 1s and Cr 2p). The properties of the photoemission lines and the changes that are induced by the increasing chromium overlayer are described in detail. This will be followed by the presentation of the shallow core level (Ti 3p, O 2s and Cr 3p) and valence band spectra that are related to the corresponding core levels. Finally, the analysis will be concluded by XAS spectra, especially by those measured at the Cr 2p edges, where a time dependence of the properties is observed. These spectra then are related to their corresponding CIS spectra of the Cr 3d band gap state.

5.3.1 SR-PES Results

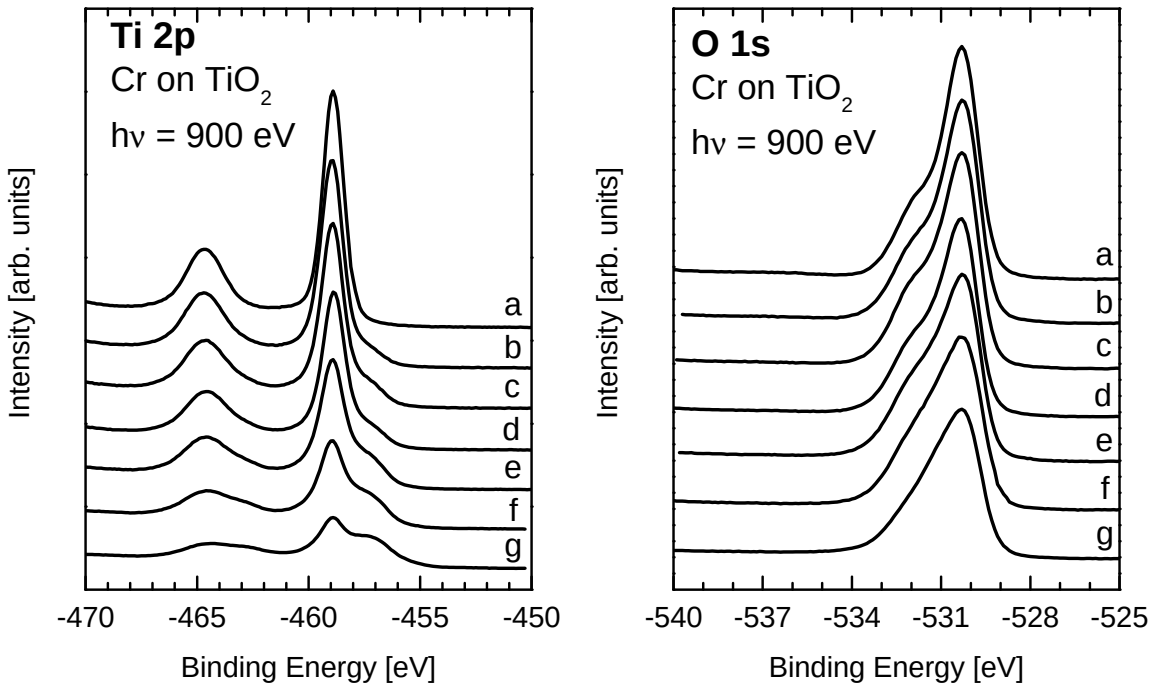

(a) Ti 2p; $h\nu$=900 eV (b) O 1s; $h\nu$=900 eV

Figure 5.27: Series of Ti 2p and O 1s core level spectra from clean film (a), less than 0.1 ML Cr (b), 0.1 ML Cr (c), 0.3 ML Cr (d), 0.5 ML Cr (e), 1 ML Cr (f) and 1.7 ML Cr (g) deposited on TiO_2

The series of the Ti 2p core level spectra with increasing Cr coverage is shown in Fig. 5.27(a). The series starts with the spectrum of the clean TiO_2 film (curve a). The corresponding properties are already described in detail above.
Upon the first deposition step, resulting in a layer thickness less than 0.1 ML of Cr (curve b), the Ti 2p intensity decreases and a shoulder at the low binding energy side at -457.4 eV appears. This shoulder shows the reduction of Ti^{4+} to Ti^{3+} at the interface.

Its intensity increases, when the Cr coverage is increased to 0.1 ML (curve c). In the next step of Cr growth (curve d), the intensity of the Ti^{4+} peak is decreasing further, while the Ti^{3+} peak is increasing. During the following deposition steps (to 0.5 ML, curve e; and to 1 ML, curve f) an ongoing decrease of the overall Ti 2p intensity occurs, while the relative Ti^{3+} intensity increases.

When the Cr layer thickness has reached the maximum value of 1.7 ML (curve g), there is significantly increased contribution from the low binding energy side at -456.4 eV. Now, a third component can be assumed to be present, the most likely one would be Ti^{2+}. The metallic state Ti^0 can be excluded, as the binding energy in metallic titanium is at significantly lower energy values of -454 eV.

The corresponding O 1s spectra are shown in Fig. 5.27(b). This series again starts with the clean film in curve a, which is also described above, although the discussion of these results is not straightforward as in the case of the Ti 2p series. The most significant changes are observed at the high binding energy side of the O 1s peak. When the chromium coverage increases from the clean film (curve a) to the maximum thickness of 1.7 ML in curve g, it becomes visible that the separation of the mainline and the high energy shoulder becomes less and less clear. This leads to an asymmetric peak in curve g, where besides the main peak no additional peaks can be assigned directly.

When the O 1s photoelectron spectra are related to the Ti 2p spectra, significant differences become evident. It can be seen that Cr deposition induces decreased O 1s intensity as well, but a quantitative analysis of both photoemission lines shows, that the integral intensity of the Ti 2p line decreases to 44% of the initial value, while the O 1s line decreases to 73% only (see Fig. 5.29), when the maximum chromium overlayer thickness is reached.

The series of the Cr 2p spectra is shown in Fig. 5.28. Upon the first deposition step (curve b), two components are visible in the Cr $2p_{3/2}$ spectrum. These components appear at binding energies of -576.4 eV and -574.6 eV. The corresponding binding energy values are additionally marked by horizontal bars. The binding energy of the $2p_{1/2}$ line is -585.5 eV resulting in a spin orbit split of 8.9 eV.

The intensity of the two components is increasing when the Cr thickness is further increased.

At an overlayer thickness of 1 ML (curve f), the spectrum is broadened and only one broad peak rather than two distinguishable ones are observed. The maximum of this broad peak is found at -576.2 eV in this curve, while in curve g the maximum is found at -575.3 eV.

In Fig. 5.29, the quantitative analysis of the core level emissions are shown. The decrease of the Ti 2p line is used in the model (solid line) of a layer by layer growth to calculate the Cr thickness. According to the model, the intensity of the Cr 2p line should increase

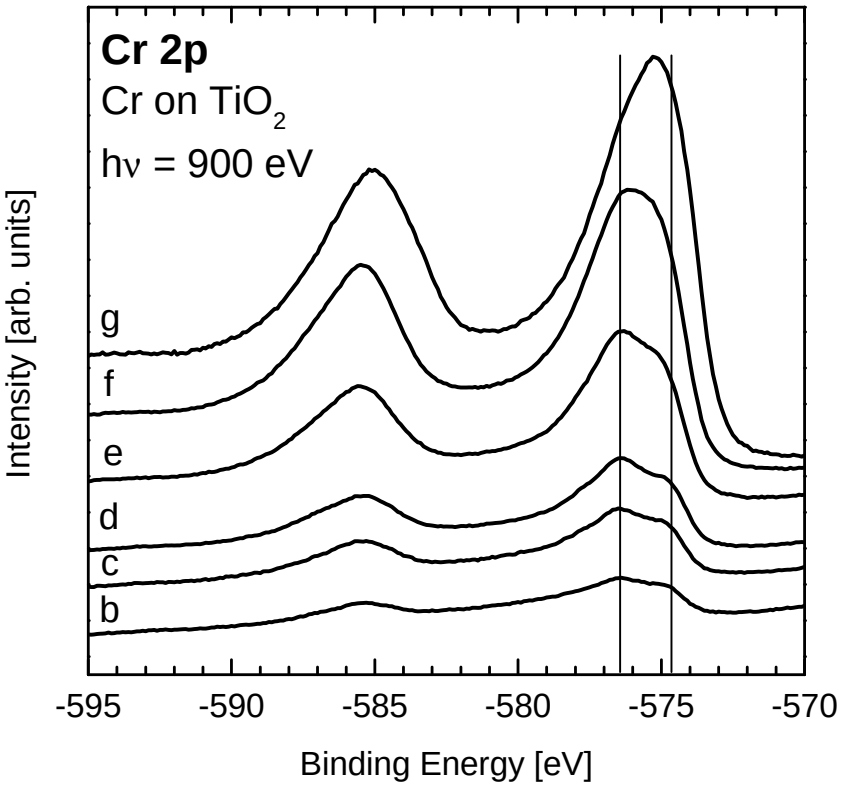

Figure 5.28: Series of Cr 2p core level spectra from less than 0.1 ML Cr (b), 0.1 ML Cr (c), 0.3 ML Cr (d), 0.5 ML Cr (e), 1 ML Cr (f) and 1.7 ML Cr (g) deposited on TiO_2; $h\nu$=900 eV

like

$$I(d) = I_0 \left(1 - \exp \frac{-d}{\lambda_{el} \cdot \cos(\theta)}\right)$$

where $I(d)$ is the intensity of a film with thickness d, I_0 is the intensity of film with infinite thickness, λ_{el} is the attenuation length of the photoelectrons of Cr 2p in the chromium overlayer, and θ is the angle between surface normal and optical axis of the analyser. For I_0 a value of 1.5 is used, as the photoemission cross section for Cr 2p is about 1.5 times the value of Ti 2p [101].

The intensity of the O 1s line follows the exponential decay during the first three steps of Cr growth, up to a layer thickness of 0.3 ML, but it increases again in the following step, which leads to 0.5 ML Cr coverage. It is evident that the O 1s intensity decreases slower than the Ti 2p intensity.

The series of the shallow core level spectra (Cr 3p, Ti 3p, O 2s) are measured in bulk sensitive ($h\nu$=450 eV, well below any absorption edge in Fig. 5.30(a)) and surface sensitive ($h\nu$=150 eV, Fig. 5.30(b)) mode. In both modes, two components are visible in the Cr 3p spectra, also in the first step. In the very first step ($<$ 0.1 ML), the Cr 3p contribution arises and becomes visible above the background. The low binding energy feature appears at -42 eV, while the high binding energy component appears at -43.8 eV. The intensity is increasing with increasing chromium overlayer thickness, but differences are observed for

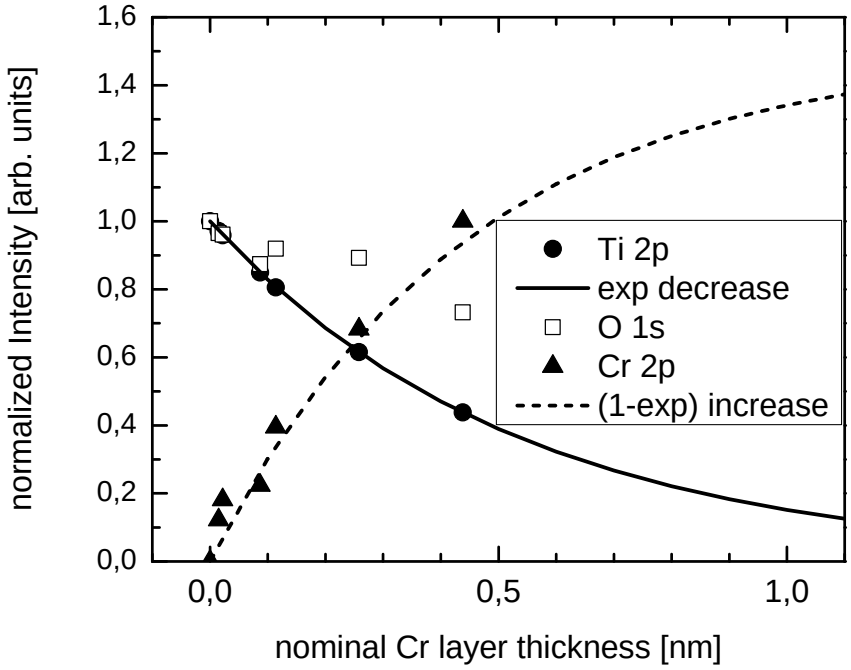

Figure 5.29: Analysis of the integral intensities of Ti 2p (full circles), O 1s (open squares), Cr 2p (full triangles) at $h\nu$=900 eV as function of nominal Cr layer thickness. The model of exponential decay (solid line) for Ti 2p and (1-exp) growth (dashed line) for Cr 2p are included.

the bulk and surface sensitive spectra. In the bulk sensitive spectrum, the component at the high energy side has higher intensity than the low binding energy component, while this is vice versa in case of the more surface sensitive spectrum. This behaviour does not change until an overlayer thickness of 1 ML is reached. Only when the layer thickness has reached its maximum thickness of 1.7 ML, the low binding energy feature is dominating in the bulk sensitive spectrum as well. This is different in case of the surface sensitive spectrum, where the low binding energy feature has higher intensity already in the first step of growth.

The Ti 3p spectra are comparable to the Ti 2p spectra, although the high initial FWHM of the Ti 3p line makes a detailed discussion more difficult. In both modes, the intensity is decreasing when chromium is deposited on the surface, while additional contribution from the low binding energy side is observed. This observation is similar to the results that are found in the Ti 2p lines. As observed for Ti 2p and O 1s the core level spectra, the shallow core levels Ti 3p and O 2s decrease in a different way as a result of chromium deposition. An analysis of the surface sensitive spectrum shows the decrease of the Ti 3p line, as described above, but the intensity of the O 2s line now remains almost constant, indicating an increased amount of oxygen at the surface, while Ti remains in the bulk.

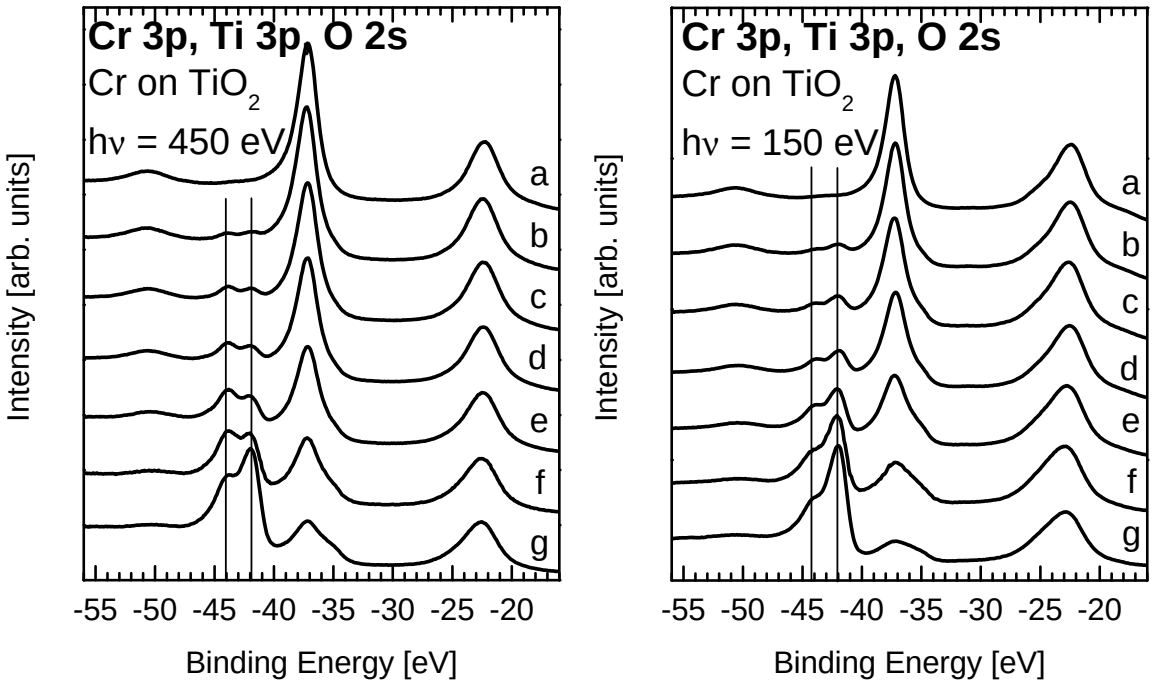

(a) Cr 3p, Ti 3p and O 2s in bulk sensitive mode; $h\nu$=450 eV

(b) Cr 3p, Ti 3p and O 2s in surface sensitive mode; $h\nu$=150 eV

Figure 5.30: Series of the shallow core level spectra from clean film (a), less than 0.1 ML Cr (b), 0.1 ML Cr (c), 0.3 ML Cr (d), 0.5 ML Cr (e), 1 ML Cr (f) and 1.7 ML Cr (g) deposited on TiO_2

In order to do a quantitative analysis, the resulting peak areas are normalized to the respective photoemission cross section, as this is considered to be the most crucial parameter for the so called sensitivity factors. This method is suitable, due to the small energy separation of the peaks. In this way, the kinetic energy differences can be neglected as well as different escape depth of the photoelectrons and, consequently, other parameters such as the transmission function of the analyser, are eliminated.

The results of bulk sensitive measurements are shown in Fig. 5.31(a), the results from the surface sensitive measurements are shown in Fig. 5.31(b). The plots are comparable with the analysis of the core level spectra in 5.29, where the purpose was to show the different decreasing behaviour of the Ti 2p and O 2s lines. In both cases, the result for the composition of the clean film is roughly 30% of titanium and 70% of oxygen, which is a significant difference to the nominal ration of 1:2 for the stoichiometric TiO_2 film. Corresponding to the results before, the oxygen content shows a different behaviour with increasing chromium thickness than the titanium content. This is observed in both the surface and bulk sensitive measurements. The surface sensitive measurement then shows a lower oxygen content in the final stage than the bulk sensitive method.

The content of Ti^{4+} is decreasing from around 30% to less than 10% in the final step, while the content of Ti^{3+} is around 2% in the first step of chromium growth and then remains

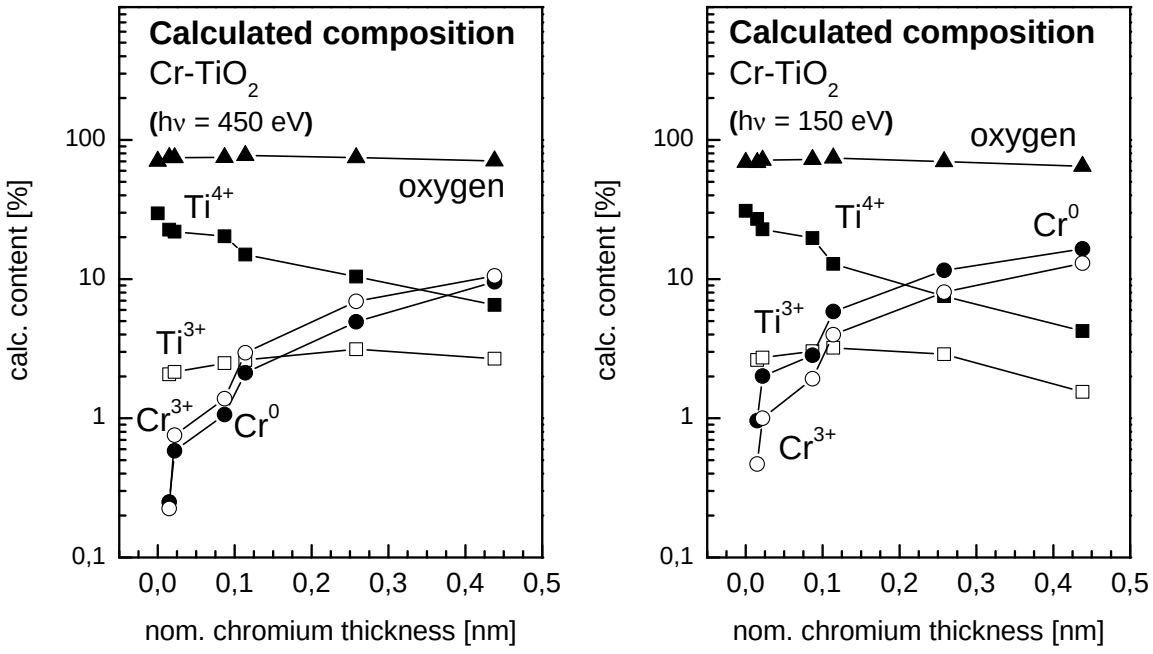

(a) Calculated content of individual species of oxygen, titanium and chromium, $h\nu$=450 eV

(b) Calculated content of individual species of oxygen, titanium and chromium, $h\nu$=150 eV

Figure 5.31: Calculated content of oxygen, titanium and chromium as a function of chromium overlayer thickness, results from bulk sensitive measurements with $h\nu$=450 eV (left panel), and surface sensitive measurement (right panel)

almost constant until the final stage. Only then, the content of Ti^{3+} is decreasing again. The general behaviour is observed in surface sensitive mode as well, but the content of Ti^{4+} decreases stronger than in the bulk sensitive mode. In the final stage, the content is now only around 4%, while decreasing content is evident already upon the third step of growth.

Both the Cr^0 and Cr^{3+} content are increasing very similar to each other, but the content of both components is higher in surface sensitive mode, where it start at around 1% for the metallic component in the first step, and ends up at around 20% upon the final step. In the bulk sensitive mode, the respective values are around 0.2% and less than 10% respectively. The summary of these results is also shown in tables 5.3 (bulk sensitive measurement) and 5.4 (surface sensitive measurement).

The valence band spectra are shown in an extra plot in more detail, again as a series of surface and bulk sensitive spectra. The properties of the valence band spectra of the clean TiO_2 film are described above. The spectral shape changes in both cases, when Cr is deposited. The spectrum of the clean film has two pronounced peaks. With increasing Cr overlayer thickness, this valence band emission develops into a structure with only one broad peak.

The changes in the band gap region are of more interest. While in both modes no emission (see 5.17 for details) from the gap region is visible, it becomes evident that initial

Cr thickness	Ti^{4+}	Ti^{3+}	Cr^{0}	Cr^{3+}	Oxygen
clean	29.7%	0%	0%	0%	70.3%
<0.1 ML	22.6%	2%	0.3%	0.2%	74.9%
0.1 ML	21.9%	2.1%	0.6%	0.8%	74.6%
0.3 ML	20.2%	2.5%	1.1%	1.4%	74.8%
0.5 ML	15%	2.6%	2.1%	2.9%	77.4%
1 ML	10.4%	3.1%	4.9%	6.9%	74.4%
1.7 ML	6.5%	2.7%	9.6%	10.5%	70.7%

Table 5.3: Composition of the interface layer as result from the analysis of the Cr 3p, Ti 3p and O 2s lines in bulk sensitive mode ($h\nu$=450 eV)

Cr thickness	Ti^{4+}	Ti^{3+}	Cr^{0}	Cr^{3+}	Oxygen
clean	31%	0%	0%	0%	69%
<0.1 ML	27%	2.6%	0.9%	0.5%	69%
0.1 ML	22.7%	2.7%	2%	1%	71.6%
0.3 ML	19.7%	3%	2.8%	1.9%	72.6%
0.5 ML	12.9%	3.2%	5.9%	4%	74%
1 ML	7.5%	2.9%	11.5%	8.1%	60%
1.7 ML	4.2%	1.5%	16.5%	13%	64.8%

Table 5.4: Composition of the interface layer as result from the analysis of the Cr 3p, Ti 3p and O 2s lines in surface sensitive mode ($h\nu$=150 eV)

Cr deposition induces two gap states. In the first step (< 0.1 ML), one gap state appears at a binding energy of -2.4 eV (surface sensitive mode), the second one has a binding energy of -0.7 eV. With increasing Cr thickness, the high energy state is shifting to lower energy.When the thickness has reached 1.7 ML, its binding energy is reduced to -2.1 eV. The low energy state remains visible as a shoulder with constant binding energy.
When the layer thickness has reached 1.7 ML, there is also emission close to the Fermi-Energy. The bulk sensitive spectra show the same behaviour. Initial Cr deposition induces the in-gap emission at around -2 eV, which also shifts to lower binding energy when the layer thickness increases. In contrast to the surface sensitive series, in the bulk sensitive spectra the low energy gap state is not clearly resolved, but is only visible as shoulder at the low energy side. Here, at maximum layer thickness, emission from the Fermi-Energy is clearly visible.
One additional observation is a time dependence of the system, which can be seen in Fig. 5.33. The first spectrum is already shown in Figs. 5.30(a) and 5.32(a). In this spectrum, the intensities of the two chromium components are comparable to each other. In the second spectrum, which is measured with significant time delay, the intensity of the Cr^{0} component has significantly decreased two around 2/3 of its initial intensity.
This time dependence is not systematically investigated in the photoemission spectroscopy measurements, but in order to investigate some of these properties, a fresh TiO_2 sample with around 0.3 ML of chromium deposited on the surface is prepared. The layer thickness

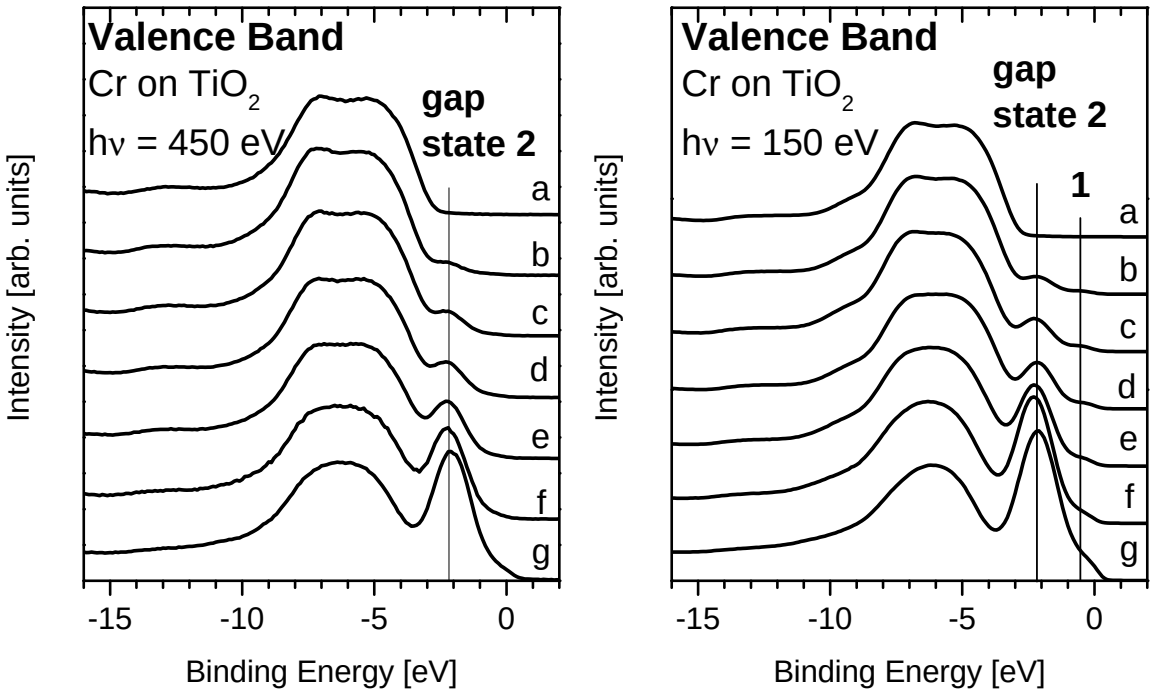

(a) Valence band in bulk sensitive mode; $h\nu$=450 eV

(b) Valence band surface sensitive mode; $h\nu$=150 eV

Figure 5.32: Series of valence band spectra from clean film (a), less than 0.1 ML Cr (b), 0.1 ML Cr (c), 0.3 ML Cr (d), 0.5 ML Cr (e), 1 ML Cr (f) and 1.7 ML Cr (g) deposited on TiO_2

is comparable to that of curves d in the previous experiments. This sample is not used for further experiments, the full series of chromium adsorption presented in this section is done with the same sample.

The overview spectra in Fig. 5.34(a) show that the C 1s intensity is also changed. The comparison between the as-prepared overview spectrum and its C 1s region with the post-deposition spectrum shows that the amount of carbon is significantly decreased by around 50%. An accurate quantification is somewhat difficult in this case, as no detailed C 1s spectra was recorded.

The as-deposited Cr 2p spectrum in Fig. 5.34(b) is very similar to that shown in curve d in Fig. 5.28. The two distinct components with an energy of separation of 1.8 eV are clearly visible. Upon the delay, the low-binding energy component i.e. the metallic component vanishes completely and only the oxidized component at 576.4 eV remains, indicating fully oxidized chromium. The appearance of an additional high binding energy component is evident as well, probably due to the formation of an additional oxidized component.

In the Ti 2p spectra in Fig. 5.34(c), a similar post-deposition oxidation is visible as well. The as-deposited spectrum shows the Ti^{4+} component at -458.9 eV together with the reduced Ti^{3+} component at around 1.5 eV lower binding energy. Upon time delay, re-oxidation occurs, in which all Ti^{3+} is oxidized to Ti^{4+} again. There is virtually no difference between the Ti 2p spectrum of the clean film and the Ti 2p spectrum of 0.3 ML

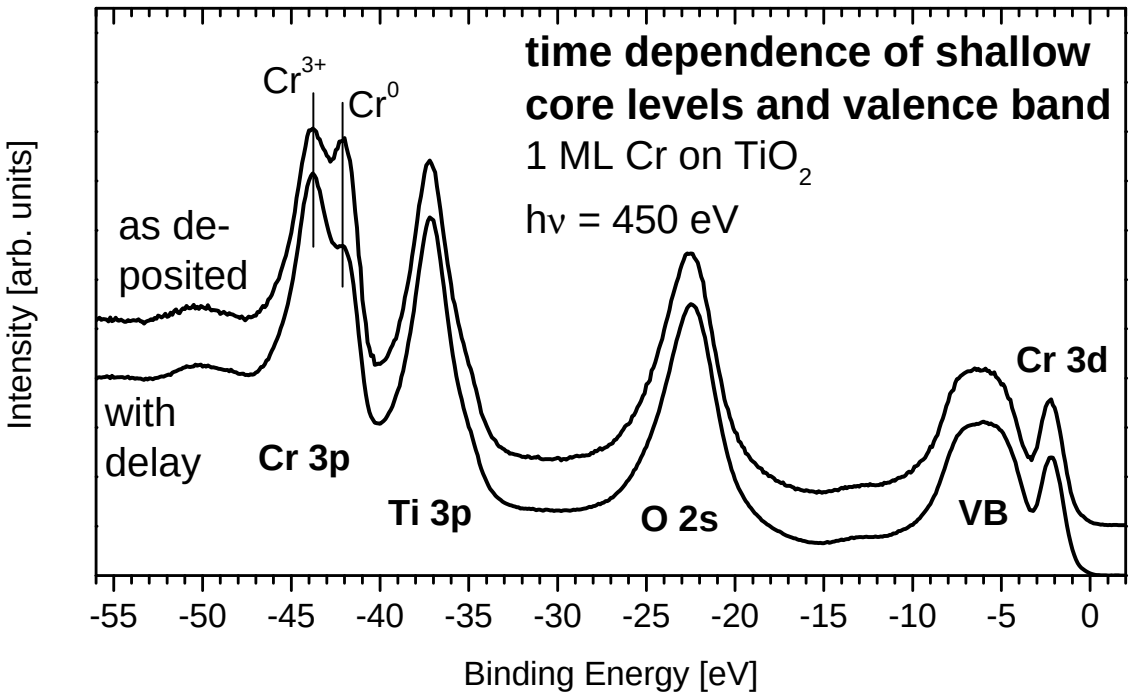

Figure 5.33: Time dependence of 1 ML Cr on TiO_2, observed in the photoemission spectra of the shallow core level Cr 3p. The 'as deposited' spectrum (top curve) is measured immediately after the deposition, the 'delayed' spectrum is measured after a break of 24 hours due to the operation schedule.

chromium deposited on this film, when a time span of around 3 hours has elapsed.
It pointed out that this observations are made in UHV conditions at base pressure in the 10^{-9} mbar range without exposure to additional gas. These properties of TiO_2 supported chromium have not been investigated systematically in the photoemission experiments, but an influence is clearly seen in the x-ray absorption spectra that are shown in the following section.

5.3.2 XAS Results

The series of XAS spectra at the Ti 2p edge with increasing Cr thickness are shown in Fig. 5.35(a). The spectral shape of the Ti 2p XAS is not significantly influenced by the increasing Cr overlayer, while the integral intensity is decreasing as a result of Cr deposition. In general, the distinct peaks of the clean film spectrum become less prominent i.e. smeared out when the overlayer thickness is increased. This is evident for the main peaks as well as for the pre-edge features. One additional observation is the fact, that the e_g peak in the L_2 decreases stronger than the t_{2g} peak. In case of the clean film (curve a), the e_g peak has the higher intensity, while at maximum Cr thickness (curve g) the peak intensities are the same. It has to be pointed out, that this behaviour is not observed in the L_3 region of the spectrum. Here, the t_{2g} and the two e_g peaks decrease uniformly.
The O 1s XAS spectra are shown in Fig. 5.35(b), where an influence is observed as

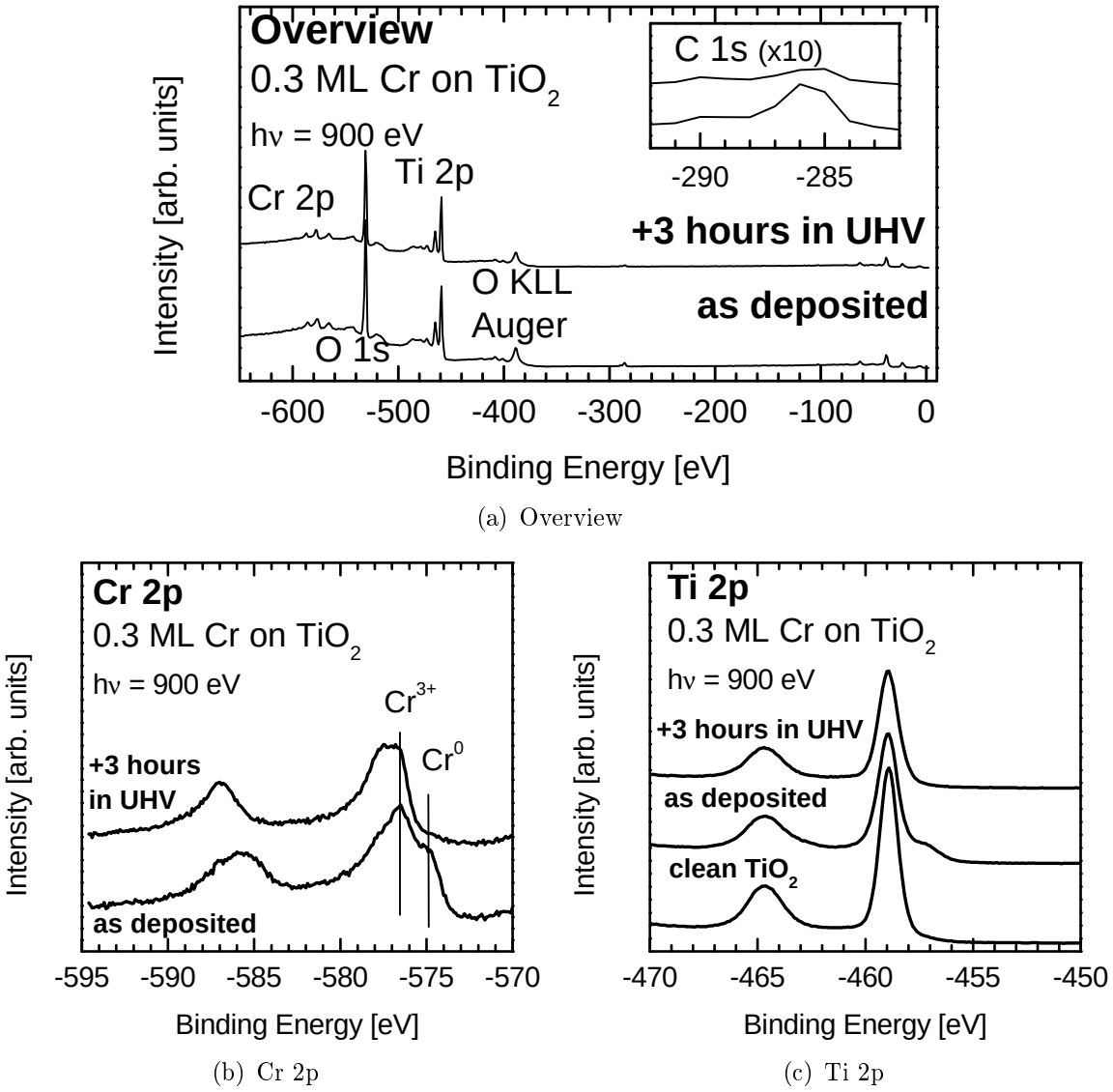

(a) Overview

(b) Cr 2p

(c) Ti 2p

Figure 5.34: The time dependence of the core levels from 0.3 ML Cr on TiO_2, as-deposited (bottom curves), and upon 3 hours in UHV (top curves) in (a) and (b). For comparison, the Ti 2p spectrum of the as-prepared film is included in (c).

well. Similar to the observation at the Ti 2p edge, the distinct features from the clean film (curve a), become more and more smeared out until the maximum layer thickness is reached (curve g). This is also visible for the high energy side between 536 eV and 548 eV. The intensities of the two main peaks at 530.7 eV and 533.3 eV decrease in different ways. In the XAS of the clean film (curve a), the low energy peak has higher intensity than the high energy feature, but then decreases stronger when Cr is deposited. When the maximum layer thickness is reached, both peaks have the same intensity. The analysis of the of Cr 2p XAS spectra is more difficult (Fig. 5.36) and the interpretation not as straightforward as in case of the Ti 2p edge spectra. Additionally, a time dependence is observed between the spectral shapes of the first XAS series (bold lines) and the second one (thin lines), which is measured with some time delay. The onset of the L_3 edge at

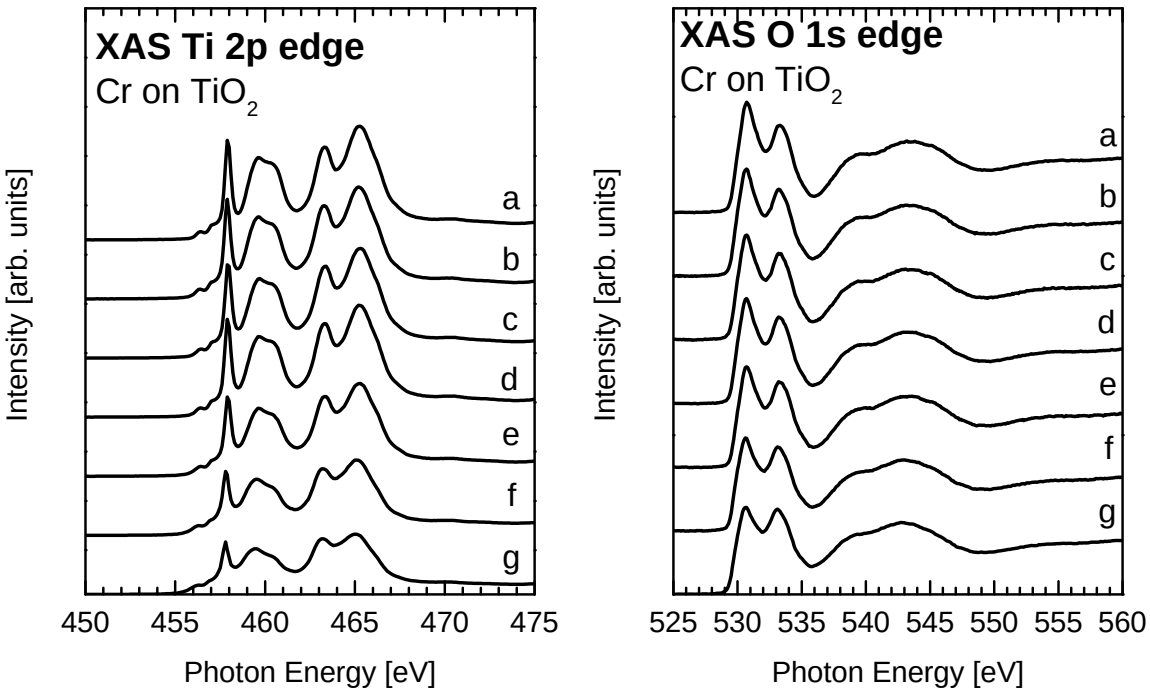

(a) XAS at Ti 2p edge

(b) XAS at O 1s edge

Figure 5.35: Series of XAS spectra at the Ti 2p and O 1s edges from clean film (a), less than 0.1 ML Cr (b), 0.1 ML Cr (c), 0.3 ML Cr (d), 0.5 ML Cr (e), 1 ML Cr (f) and 1.7 ML Cr (g) deposited on TiO_2

575 eV in curves b is clearly visible. In curve c (0.1 ML), fine structures become resolved in both datasets. In the bold curve c (first measurement), the L_3 part consists of the peaks at 575.3 eV, 576.4 eV and 577.3 eV and the L_2 edge consists of two peaks found at 583.9 eV and 585.4 eV. In the second spectrum (thin line), small but crucial changes are evident. In the L_3 part of the spectrum, the intensity of the first peak at 575.3 eV decreases. In the L_2 part of the spectrum, changes are visible as well, but not as strong as in the L_3 part. Here, the intensity of the peak at 583.9 eV decreases.

When the layer thickness is further increased (curves d and e), the fine structures become better resolved with increasing intensities. In both described steps, the time dependence is observed. While in curve d, the behaviour is very similar to that observed in curve c, this differs now in curve d. The intensity of the first peak is decreasing too, while that of the third peak at 577.3 eV is now increasing. The corresponding results in the L_2 region are very similar, the pre-peak at 583.9 eV now decreases, while the intensity of the L_2 main features is increasing as well.

In curve f (1 ML of Cr), an additional shoulder on the high energy side, around 578 eV, of the L_3 part is visible. Prior to the L_2 edge, a small pre-peak at around 582 eV appears as well. The peak at 583.9 eV is now separated from the other one at 585.4 eV. In curve f of the second dataset, the time dependence is better pronounced. Decreasing intensity of the first feature is clearly visible, while the intensity of the third peak increases stronger than

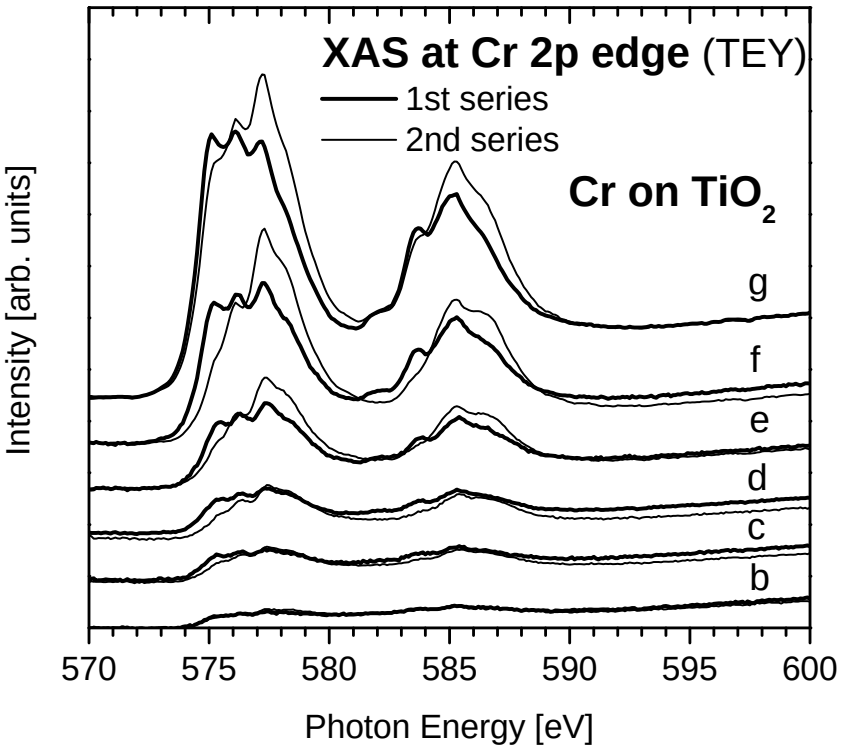

Figure 5.36: Series of Cr 2p XAS spectra from less than 0.1 ML Cr (b), 0.1 ML Cr (c), 0.3 ML Cr (d), 0.5 ML Cr (e), 1 ML Cr (f) and 1.7 ML Cr (g) deposited on TiO_2, the first series (bold lines) is measured directly after preparation, the second series (thin lines) is measured after a typical time span of 2 hours has elapsed.

before. The L_2 pre-peak at 582 eV is now suppressed as well as the L_2 peak at 583.9 eV. Similar to the results before, the intensity of the L_2 main peak increases as well as the high energy side of the L_2 part at around 586 eV. The comparison of curves f (1 ML) leads to similar results as the comparison of curves g, although the changes are not as clearly pronounced as before.

As a second step, the CIS spectra are analysed together with their corresponding XAS spectra in Fig. 5.37. The series of the CIS spectra is measured parallel to the measurements of the second XAS series, which means that a comparison between XAS and CIS spectra is allowed for these datasets only. In order to allow a qualitative comparison, the spectra are scaled to comparable intensities.

As it can be seen in the figure, the CIS spectra (bold lines) exhibit a significantly better signal to background ratio in the low coverage regime than the XAS spectra. Similar to the XAS spectra, the onset of the CIS spectrum is visible at around 575 eV. This spectrum then shows three distinct peaks at 575.4 eV, 576.3 eV and 577.4 eV together with a shoulder at the high energy side at around 579 eV. The onset of the L_2 edge is observed at 583 eV followed by a small peak at 583.8 eV and the main peak of the L_2 region at 586.9 eV. In curve c, representing the following deposition step, the observed features become more pronounced and better resolved without shift of the energy positions. Changes

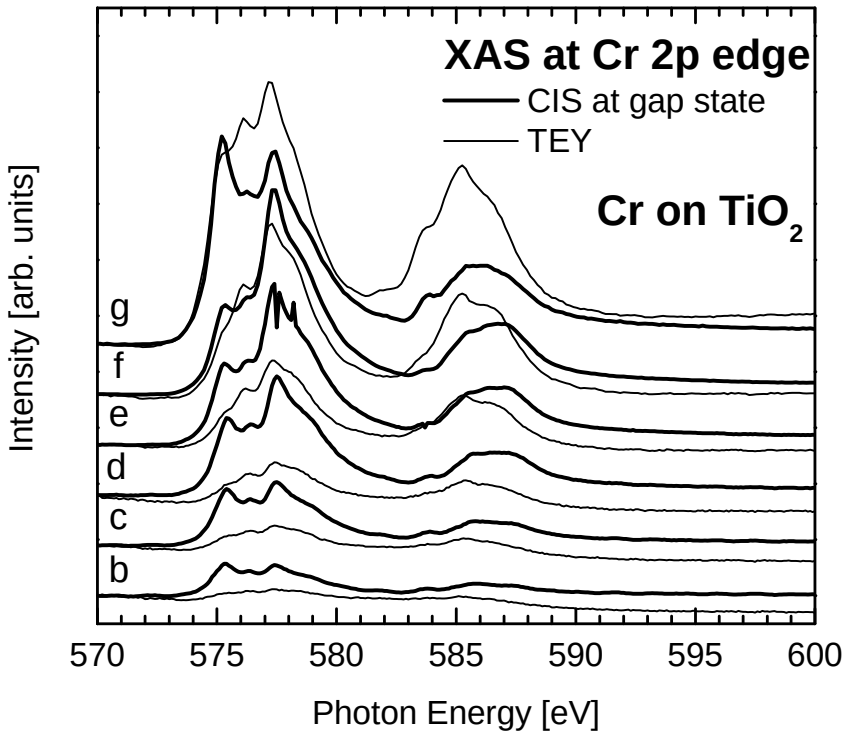

Figure 5.37: Series of CIS spectra at Cr 3d gap state (bold lines) and XAS spectra (thin lines, second series, measured parallel to the CIS spectra) at the Cr 2p edge of less than 0.1 ML Cr (b), 0.1 ML Cr (c), 0.3 ML Cr (d), 0.5 ML Cr (e), 1 ML Cr (f) and 1.7 ML Cr (g) deposited on TiO_2

are observed upon the third deposition step (curve d), where, the intensity of the peak at 577.4 eV has increased in comparison to the other two peaks of the L_3 edge.
The shape of curve e is very similar to that of curve d, except some spikes. This is an experimental artefact without any physical meaning. It is an additional observation, that the shape of the L_2 part has changed. In curve d, a broad peak (around 4 eV) is observed. The width is the same in curve e, but the low energy side of this broad peak is slightly lower than the high energy side. Curve f then shows an ongoing intensity increase of the 577.4 eV peak, accompanied by a decrease of the first peak at 575.4 eV. Additionally, the peak at 576.3 eV is overlapping with the 577.4 eV peak. The observed changes in the L_2 edge continue and the low energy side is further decreasing, although the changes are not as clear as in the L_3 edge. The L_2 peak is found at around 587 eV, the low energy contribution is observed at around 1.5 eV lower energy.
The final step (curve g) induces another significant change of the spectrum. Now, the first peak (575.4 eV) has increased intensity and is as high as the peak at 577.4 eV. The peak in between these two (576.3 eV) is still resolved.
The comparison with the XAS spectra (thin lines) proves that all features found in the XAS spectra can be assigned to their corresponding features in the CIS spectra, although the intensity ratios are different. Especially in curves e to g it is visible, that the branching ratios between L_3 and L_2 edges are different in the CIS and TEY spectra, with higher

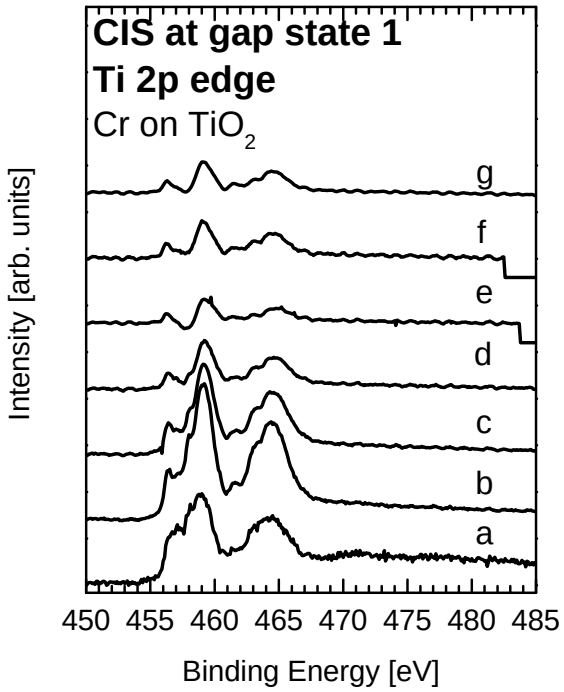

Figure 5.38: Series of CIS spectra at Ti 3d gap state at the Ti 2p edge of a clean film (a), less than 0.1 ML Cr (b), 0.1 ML Cr (c), 0.3 ML Cr (d), 0.5 ML Cr (e), 1 ML Cr (f) and 1.7 ML Cr (g) deposited on TiO_2

intensity in the L_2 region in case of the TEY spectra.

The corresponding CIS spectra of the Ti 3d defect state are shown in Fig. 5.38, beginning with the clean film in curve a. The second order contribution is subtracted from the spectra. Curve a is already shown in Fig. 5.21 together with the corresponding XAS spectrum. Curve b shows a stronger resonance of the defect state as it is the case in curve a. Additional fine structures are visible in the L_2 part of the spectrum. Curve c shows essentially the same features as curve b with decreased intensity due to the increased overlayer thickness. In the higher coverage regime from curve d on, the subtracted second order contribution seems to be somewhat overestimated. Consequently, the CIS spectra are not further discussed.

5.3.3 ResPES Results

In contrast to the results from the clean thin film and the crystalline sample, now only special photon energies are chosen to record the valence band spectra at resonant excitations. The two series of valence band spectra, measured on and off Ti 2p resonance, are shown in Fig. 5.39(a). Photon energies of 450 eV (thin lines) and 457.9 eV (bold lines) are used. This energy corresponds to the Ti $2p_{3/2} \rightarrow$ Ti $3d(t_{2g})$ transition, which leads to the sharp pronounced peak in the XAS spectrum. The spectra of the clean film (curve a) are used as an addition.

For the measurements before and at the Cr 2p edge(5.39(b)), 570 eV (thin lines) and

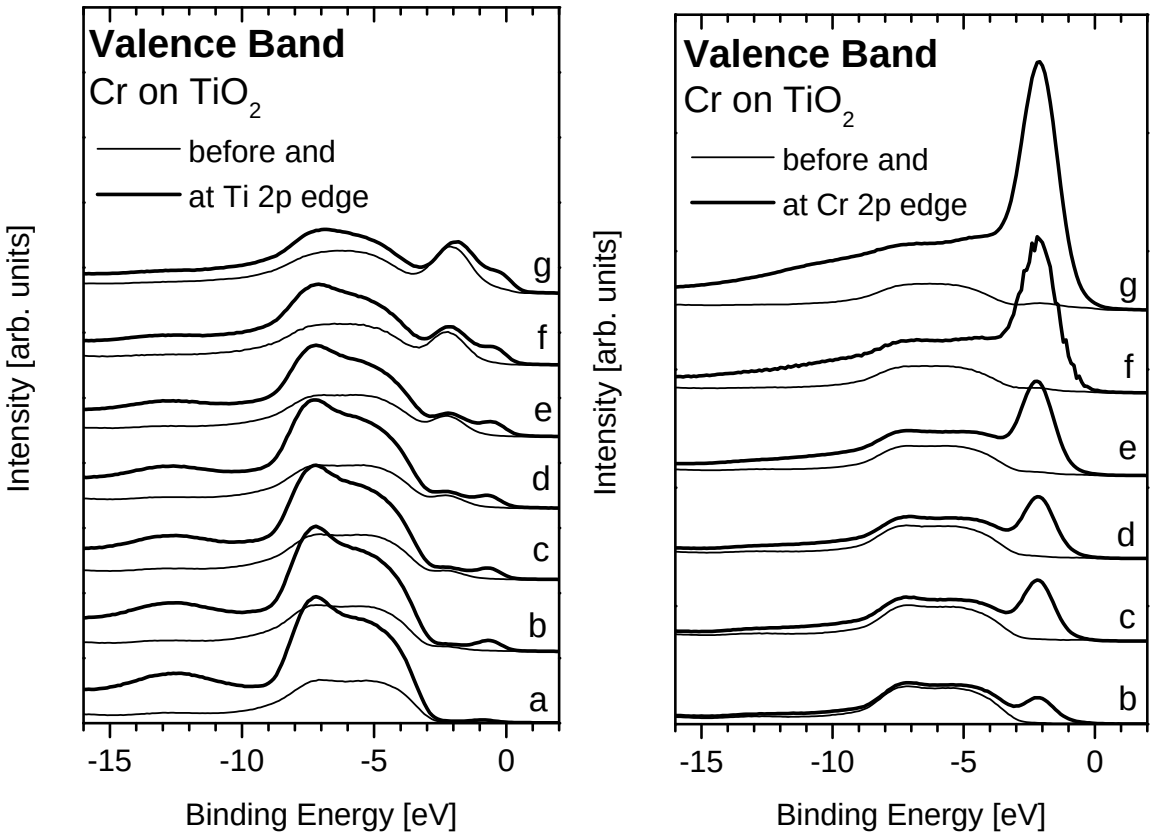

(a) on and off Ti 2p resonance measured valence band

(b) on and off Ti 2p resonance measured valence band

Figure 5.39: Series of valence band spectra on (bold curves) and off (thin curves) resonant excitation of less than 0.1 ML Cr (b), 0.1 ML Cr (c), 0.3 ML Cr (d), 0.5 ML Cr (e), 1 ML Cr (f) and 1.7 ML Cr (g) deposited on TiO_2. Before the Ti 2p edge, photon energy of 450+eV is applied, at the Ti 2p edge the photon energy is 459.7 eV. Additionally, at the Ti 2p edge higher photon energy of 463.5 eV is used as well (open circles) to eliminate the second order contribution, which crosses the gap region at photon energies of around 458 eV. The energies before and at Cr 2p edge are 570 eV and 575.4 eV.

575.3 eV are used. This energy reflects the first peak in the XAS spectra.

The clean film spectra (curves a) show the resonant enhancement of a band gap state at -0.7 eV as well as resonant enhancement of the valence band features. As already described in 5.2.3, both pronounced valence band features are not enhanced in the same way. It is evident that the high binding energy feature of the valence band is enhanced stronger than the lower lying one. The intensity enhancement in the binding energy region of around -13 eV which is described above as well, is clearly visible in this representation of the spectra too, although the Auger like character cannot be determined from this.

When Cr is deposited first (curve b), the described resonance of the band gap state increases. The observed intensity is roughly twice as high as in the clean film. The shape of the valence band at resonance follows closely that of the clean film.

The following steps (curves c to e) do not induce significant changes in both the on and off resonance valence band spectra, but it has to be pointed out that gap state 2 becomes

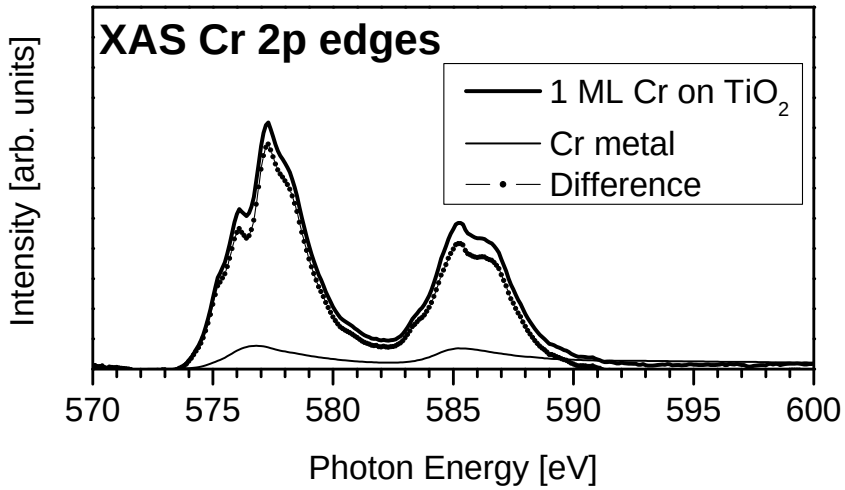

Figure 5.40: Effect of the subtraction of a metallic contribution from the experimental XAS spectrum of 1 ML Cr on TiO_2

better pronounced upon each step. The resonances of the band gap state remain the same, while the total intensity of the valence band resonance decreases step by step. Throughout the whole series, the shape of the valence band at resonant excitations remains more or less the same, as the high energy feature is always stronger enhanced than the lower one. Additionally, it is visible in spectra f and g, that this state appears at lower binding energy at resonance.

Before and at the Cr 2p edge (5.39(b)), it is visible that a resonance in the gap region occurs as well, but now the band gap state at -2.3 eV is resonantly enhanced. In the following steps from c to g, the resonant intensity increases step by step, but the binding energy position remains the same. In the first spectrum (curve b), the resonance extends up to a binding energy of about -1 eV, while in spectra g and f it has reached the Fermi-Energy at 0 eV. The origin of the spikes in curve f is an experimental artefact without physical meaning. It is also clearly visible, that the resonance intensity of the valence band increases successively from curve b to g. The intensity is not limited to the gap state and the valence band region, but extends down to -16 eV at 1.7 ML Cr. This is already evident in curve e and is still more pronounced in curve g.

5.3.4 Multiplet charge transfer calculations

The results of the XAS experiments at the Cr 2p edge (5.36) show that the shape of the XAS spectra is very similar in each series, which consequently means that not every single spectrum needs to be calculated. The XAS spectrum of 1 ML chromium on TiO_2 is chosen instead.

From the photoemission experiments (5.3.1) the existence of a metallic component is deduced. In order to enable a correct calculation and comparison, this metallic contribution is removed from the spectrum. This is shown in Fig. 5.3.4. Although the effect is rather

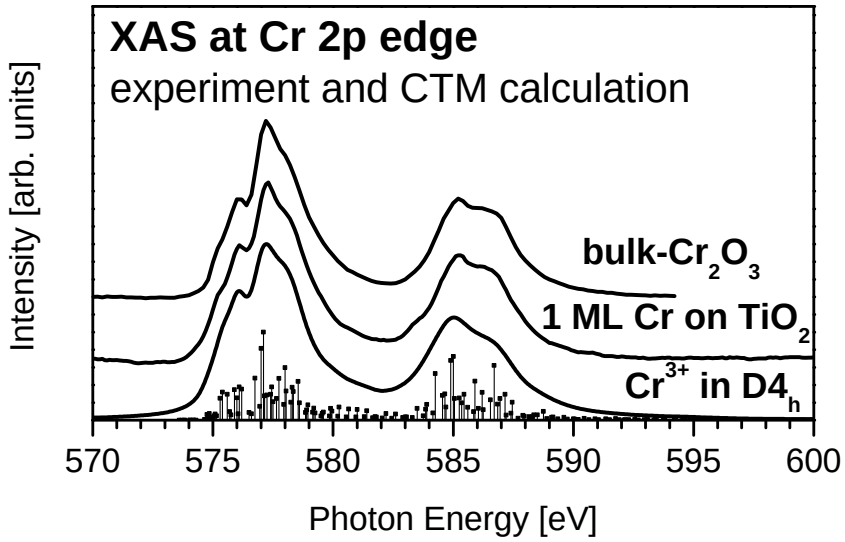

Figure 5.41: Experimental and calculated XAS spectra at the Cr 2p edges, of bulk-Cr_2O_3 (top), 1 ML Cr on TiO_2 (middle) and calculated Cr 2p XAS of a Cr^{3+} ion in D_{4h} symmetry with charge transfer. The parameters are $10Dq = 1.8eV$; $Dt = -0.04eV$ and $Ds = -0.08eV$; the CT parameters are $\Delta = 1eV$, $U_{pd} = 6eV$ and $U_{dd} = 4eV$.

small, this procedure is applied for the sake of correctness. The charge transfer multiplet model is also applied for the analysis of the Cr 2p XAS spectra, although these spectra are even more complex than the "simple" XAS spectra of TiO_2.

Fig. 5.3.4 shows the XAS spectrum of bulk-Cr_2O_3 (top curve), together with 1 ML relaxed (post-deposition oxidized) Cr on TiO_2 (TEY, middle curve). The first information derived from this comparison is the relaxation of the deposited chromium to bulk-like Cr_2O_3. The CTM result of Cr^{3+} in D_{4h} symmetry is obtained when 10 Dq = 1.8 eV, Ds = -0.08 eV and Dt = -0.04 eV. This leads to δ_1 = -0.52 eV, and δ_2 = -0.04 eV.

No reasonable agreement between a CTM calculation and the as-prepared Cr 2p XAS was found. The spectrum of bulk-Cr_2O_3 is reproduced by Seifarth in [102] from Stagarescu et al. [103]. In [40], a corresponding spectrum is found as well.

The parameter set allows the determination of the Cr 3d energy positions, as it is done for the Ti 3d levels in Fig. 5.14. The parameter set now also causes reversed ordering of the e_g and b_{2g} states. The three electrons are distributed in the low energy levels with parallel spin, according to Hund's Rule.

5.3.5 Summary of chromium deposition on titanium dioxide

In table 5.5, the most important binding energy values are given as an overview. Additionally, the results will be briefly summarized. The results from the photoemission experiments are as follows:

- The Ti $2p_{3/2}$ lines shows an additional low binding energy feature, and becomes damped to an intensity of 43% of the initial value, when the maximum overlayer

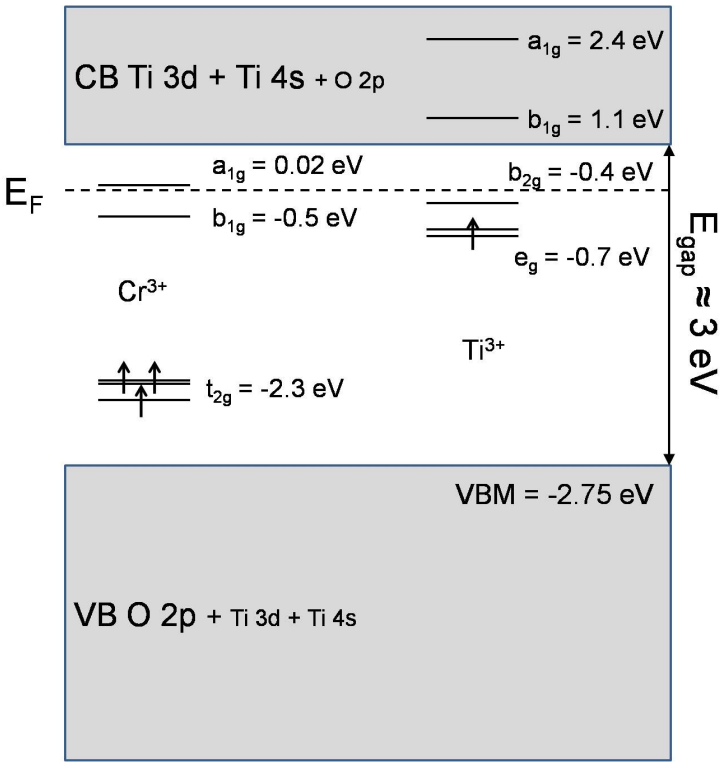

Figure 5.42: Energy level diagram for the Cr 3d and Ti 3d states, derived from the CTM parameters 10 Dq, Ds and Dt. According to the listing in Table 3.2, the order of the a_{1g} and b_{1g} is reversed as in case of TiO_2 CTM. Additionally, the calculation leads to reverse order for the e_g and b_{2g} orbitals as well, although the separation is small.

thickness is reached.

- The O 1s emission, which consists of two components in the clean film, develops to a strongly asymmetric line shape, indicating that the Cr_2O_3 component develops in between the mainline and the surface component, and is damped to only 73% of its initial value.

- The Cr 2p line consists of two components in the initial step of growth, but the two components cannot be resolved when the layer thickness is increased to the ML regime.

- The two chromium components are well resolved in the Cr 3p spectra and quantitative analysis is now applicable.

- The bulk and surface sensitive valence band spectra show the development of the two peak structure of clean TiO_2 into a structure with one single broad peak. This behaviour is more pronounced in surface sensitive mode than in bulk sensitive mode.

- The development of emissions from the band gap region is evident in both modes. Band gap state (2) develops from an in-gap emission to the more intense Cr 3d emission, where the label "gap state" is now longer reasonable.

Line	binding energy	separation to Ti $2p_{3/2}$
Ti $2p_{3/2}$, Ti^{4+}	-458.9 eV	0 eV
Ti $2p_{3/2}$, Ti^{3+}	-457.4 eV	2.5 eV
Ti $2p_{1/2}$, Ti^{4+}	-464.6 eV	-5.7 eV
Cr $2p_{3/2}$, Cr^{0}	-574.6 eV	-115.7 eV
Cr $2p_{3/2}$, Cr^{3+}	-576.4 eV	-117.5 eV
O 1s, mainline	-530.3 eV	-71.4 eV
Ti 3p, Ti^{4+}	-37.2 eV	421.7
Cr 3p, Cr^{0}	-42 eV	416.9 eV
Cr 3p, Cr^{3+}	-43.8 eV	415.1 eV
gap state 1 (Ti 3d)	-0.7 eV	458.2 eV
gap state 2 (Cr 3d)	-2.3 eV	456.6 eV

Table 5.5: Overview of photoelectron spectroscopy results of chromium deposition on TiO_2 thin film, energy positions of the main lines

5.4 Cobalt deposition on titanium dioxide

In contrast to the Cr-TiO_2 experiments, the experiments shown in this section are carried out during the low-α operation mode of the BESSY II storage ring. In this mode, the ring current is significantly lower (around one order of magnitude) and the intensity distribution is changed due to adaption of the ring's optics. This consequently means that for the achievement of reasonable signal-to-noise ratios in photoemission spectroscopy, the exit slit has to be opened to 100µm which means reduced energy resolution. Additionally, the measurement of individual CIS spectra is not possible, although TEY spectra can still be recorded with good quality. For this reason, one additional sample is prepared for measurements in the normal operation mode.

5.4.1 SR-PES results

The series of Ti 2p spectra is shown in Fig. 5.43(a), starting with the clean film in curve a. The FWHM is larger and is now 1.3 eV. This is an effect of the reduced energy resolution caused by the opened exit slit.
When cobalt is deposited first (curve b; 0.25 ML), the Ti 2p intensity decreases and a shoulder at the low binding energy side is observed. This behaviour corresponds to that from chromium deposition. The following deposition steps (curves c and d, 0.8 ML resp.

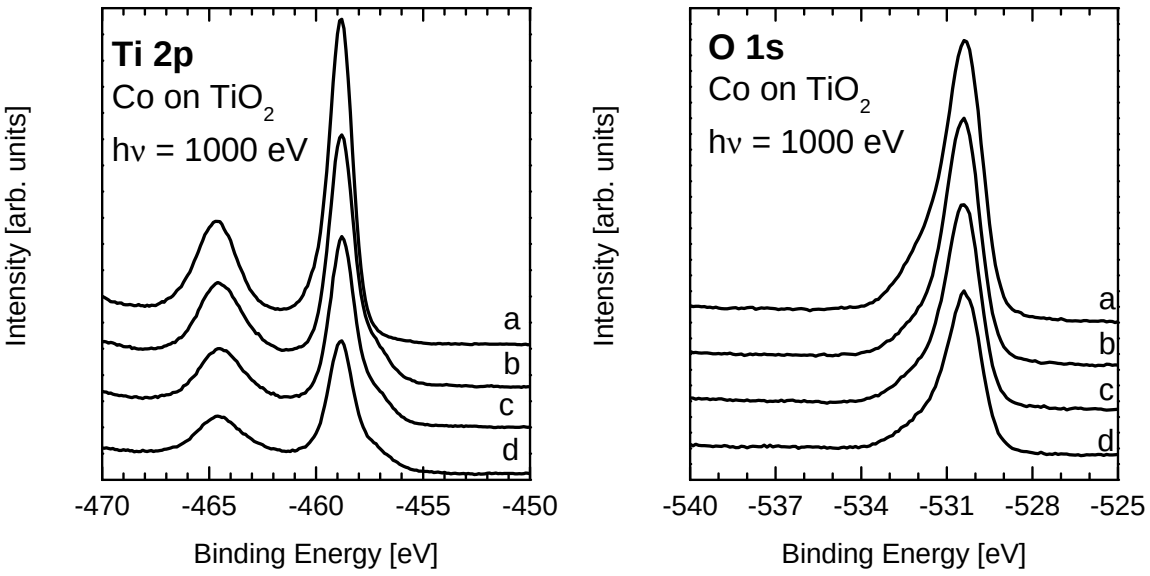

(a) Series of Ti 2p spectra

(b) Series of O 1s spectra

Figure 5.43: Series of Ti 2p and O 1s photoelectron spectra from clean TiO_2 film (a), 0.25 ML Co (b), 0.8 ML Co (c) and 1.6 ML Co (curve d) deposited on TiO_2 film; $h\nu$=1000 eV

1.6 ML Co), cause further decrease of the intensity, while the broadening of the line does not further increase.

The O 1s spectrum (5.43(b)) of the clean film (curve a), is very similar to that one shown in Section 5.2.1, although the shoulder at the high energy side is not as good resolved as in the first case. The peak of the O 1s line is located at 530.4 eV. The deposition of cobalt causes a decrease of the photoemission intensity as well. In contrast to the chromium deposition results, the spectral shape of the O 1s line does not change when cobalt is deposited.

The Co 2p spectrum of the lowest coverage obtained (0.25 ML, curve b in Fig. 5.44), shows three main features in the $2p_{3/2}$ region from -790 eV to -775 eV. As an optical guideline for the eye, these features are marked by vertical bars. The component with the lowest binding energy (-778.2 eV) is Co^0. The most intense component is found at -781 eV, which corresponds to an energy difference to Co^0 of 2.8 eV, and reflects an oxidized component. The $2p_{1/2}$ line of the oxidized component is at -797 eV which results in a spin orbit split of $\approx$16 eV.

Upon the following deposition step (curve c), the intensity of the metallic peak is increased, as well as that of the oxidized component. Upon the third deposition step (curve d), which leads to the highest coverage investigated in this series (1.6 ML), the metallic peak is dominant. In this spectrum, the metallic $2p_{1/2}$ line is well resolved as well.

For comparison, a normalized Co 2p spectrum of a metallic film is included as well. It has to be noted that the metallic spectrum is measured with a different spectrometer, which

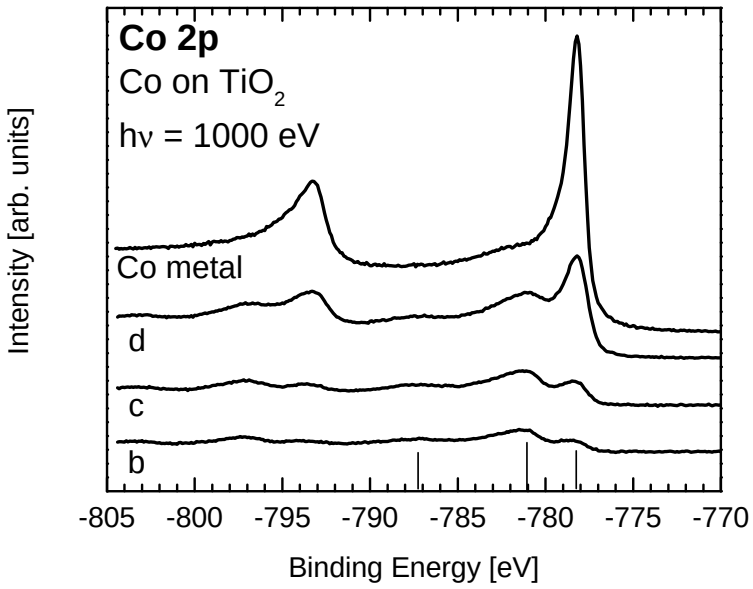

Figure 5.44: Co 2p photoelectron spectra of 0.25 ML Co (curve b), 0.8 ML Co (curve c) and 1.6 ML Co (curve d) deposited on TiO_2, for comparison, the Co 2p spectrum of metallic cobalt film is included (curve Co)

makes an absolute quantitative comparison inadequate. The 2p spectrum of the metal shows one dominant peak in the $2p_{3/2}$ region at -778.2 eV with the corresponding $2p_{1/2}$ line at -793.3 eV.

The valence band spectra of cobalt on TiO_2, measured in surface-sensitive mode, are shown in Fig. 5.45(a). The spectrum of a clean film is already shown above (Fig. 5.32(a), curve a), and thus not discussed again. The deposition of cobalt on the TiO_2 surface induces changes of the spectral shape of the valence band, similar to the results obtained from chromium deposition (5.3.1). The first in-gap emission appears at -0.7 eV, the second one at around -2.7 eV. As this state is not clearly separated from the valence band, an exact determination of the energy is difficult. In curve c, the intensity of both emissions has further increased, without obvious shifts of the binding energy. When the cobalt thickness further increases, the first in-gap emission shifts up to -0.4 eV below E_F, while the position of the second emission remains constant. Essentially the same information is deduced from the bulk-sensitive valence band spectra, but with worse signal-to-noise ratio. This is again an effect of the operation mode of the storage ring. Besides this, there are no differences concerning spectral shape or binding energy positions. It is evident that the defect state 1 at -0.7 eV in curve b is better pronounced than the defect state in case of chromium deposition. This is the case in both the surface and bulk sensitive measurements.

The analysis of the integral peak intensities is shown in Fig. 5.46. Again, the model of exponential decrease of the Ti 2p photoemission line is applied to calculate the nominal cobalt overlayer thickness. The Ti 2p and O 1s intensities are normalized to intensity

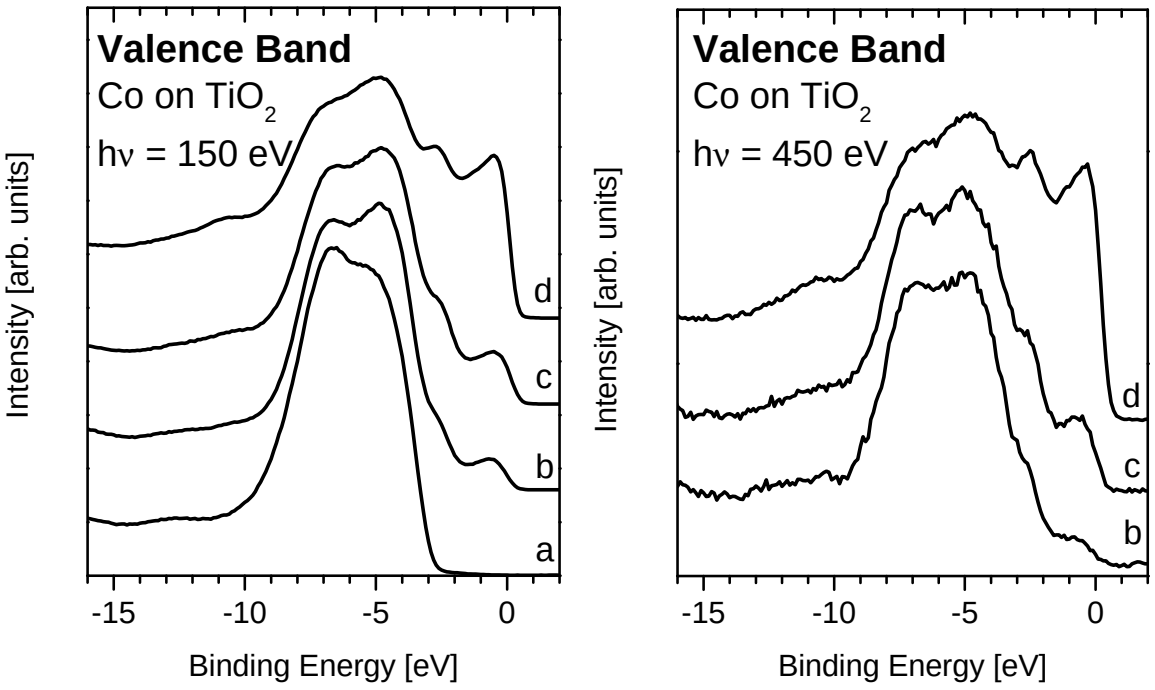

(a) Surface sensitive (b) Bulk sensitive

Figure 5.45: Valence band spectra clean of TiO_2 (a), 0.25 ML Co (curve b), 0.8 ML Co (curve c) and 1.6 ML Co (curve d) deposited on TiO_2, in surface ($h\nu$=150 eV) and bulk sensitive ($h\nu$=450 eV) mode

of One for the clean TiO_2 film, while the Co $2p_{3/2}$ intensity is arbitrarily normalized to One at the maximum investigated layer thickness. In contrast to the results of chromium deposition, the fitting of the Co 2p intensities is not applied, as there are not enough data points available to calculate a reliable model.

The most important result of this analysis is related to the behaviour of the Ti 2p and O 1s peaks. In contrast to the results in Section 5.3.1, the decreasing behaviour of the O 1s line is almost equal to the behaviour of the Ti 2p line.

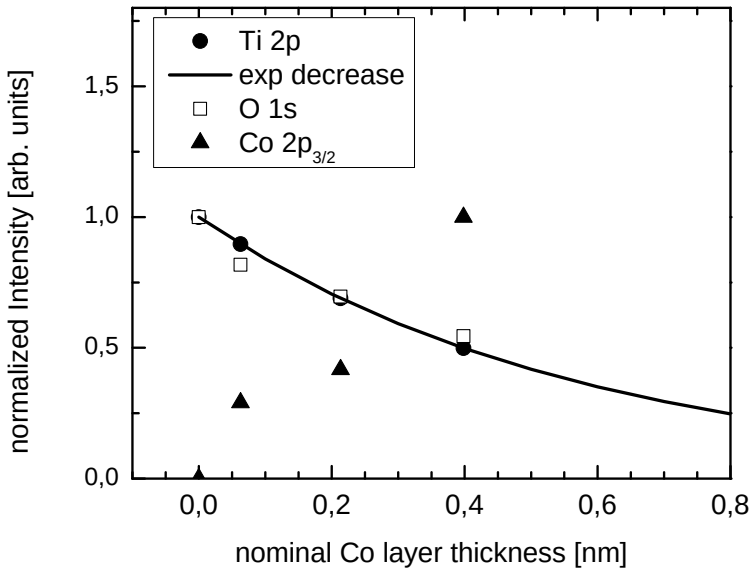

Figure 5.46: Analysis of the integral intensities of Ti 2p (full circles), O 1s (open squares), Co $2p_{3/2}$ (full triangles) at $h\nu$=1000 eV as function of nominal Co layer thickness. The model of exponential decrease (solid line) for Ti 2p is included.

5.4.2 XAS results

The XAS spectra at Ti 2p and O 1s edges are shown in Fig. 5.47. Both sets start again with the spectrum of the clean film (curves a), which are already described earlier (5.2.2). In case of the Ti 2p XAS (Fig. 5.47(a)) spectra, decreasing intensity is observed when going from the clean film to the maximum coverage of 1.6 ML cobalt in curve d. During this series, no pronounced changes of the spectral shapes are visible, except the uniform decrease of the spectral features.

Essentially the same observation is made for the O 1s spectra in Fig. 5.47(b). Besides the decreasing intensity, no visible changes of energy positions and intensity ratios of the features occur.

The onset of the L_3 absorption edge in curve b is visible at a photon energy of 777.8 eV. The main peaks follow at energies between 778 eV and 780 eV. In the energy range from 781 eV to around 784 eV, additional contribution that results in an asymmetry of the L_3 part is found. The onset of the L_2 edge follows at photon energy of around 793 eV with the L_2 peak at 793.9 eV, without any pronounced fine structures. Increased thickness of cobalt overlayer then induces improved signal-to-noise ratio with better pronounced structures, which allows a more reliable determination of the energy position of the fine structures. The analysis shows that the L_3 part consists of three peaks at 778.4 eV, 779 eV and 779.8 eV. Additionally, the asymmetric contribution between 781 eV and 784 eV becomes better pronounced. As it is the case in curve b, the L_2 range does not show any fine structures. It is obvious that the intensity of the first feature increases in comparison to the high energy part of the L_3 edge.

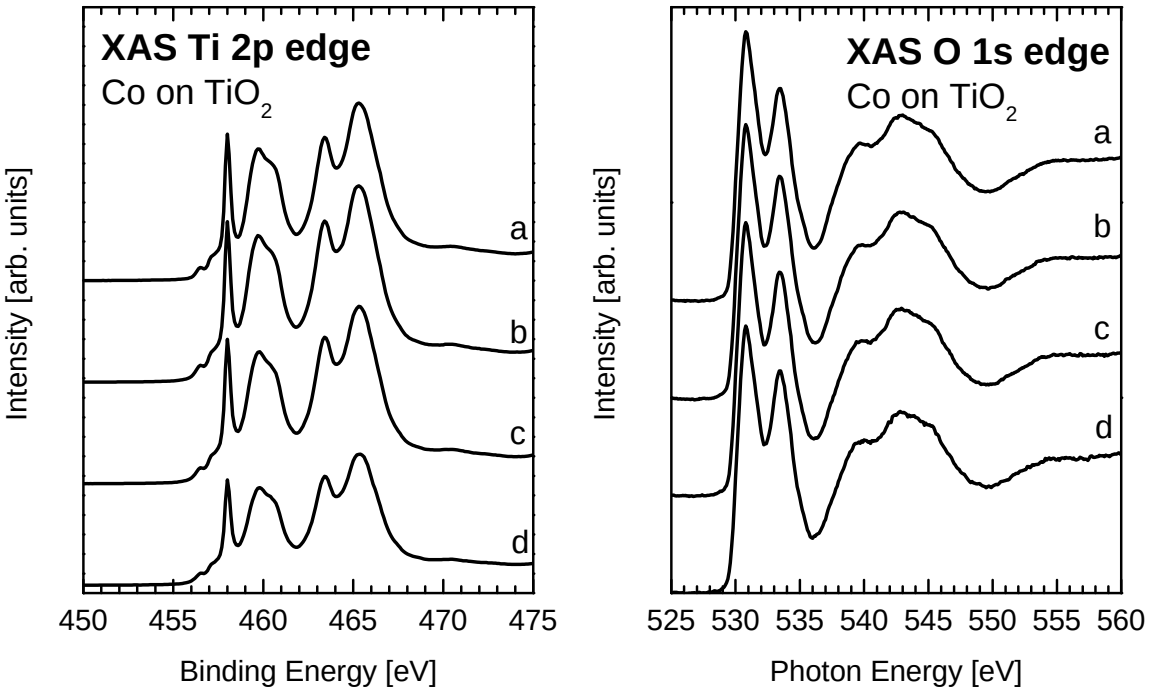

(a) Ti 2p edge

(b) O 1s edge

Figure 5.47: Series of XAS spectra at Ti 2p and O 1s edges of TiO_2 (a), 0.25 ML Co (curve b), 0.8 ML Co (curve c) and 1.6 ML (curve d) Co deposited on TiO_2

When 1.6 ML cobalt are reached, significant changes of the spectral shape occur. In contrast to curves b and c, the first feature at 778.4 eV now has significantly higher intensity in comparison to the other ones, while the onset at 777.8 eV does not change. While the other features of the L_3 edge are well resolved in curve c, this is no longer the case here. In curve d, the additional features are still present, but now only as less prominent shoulders at the high energy side. The broad feature in the energy range from 781 eV to 784 eV becomes more pronounced in comparison to curves b and c. Additionally, a similar asymmetry occurs in the L_2 edge as well.

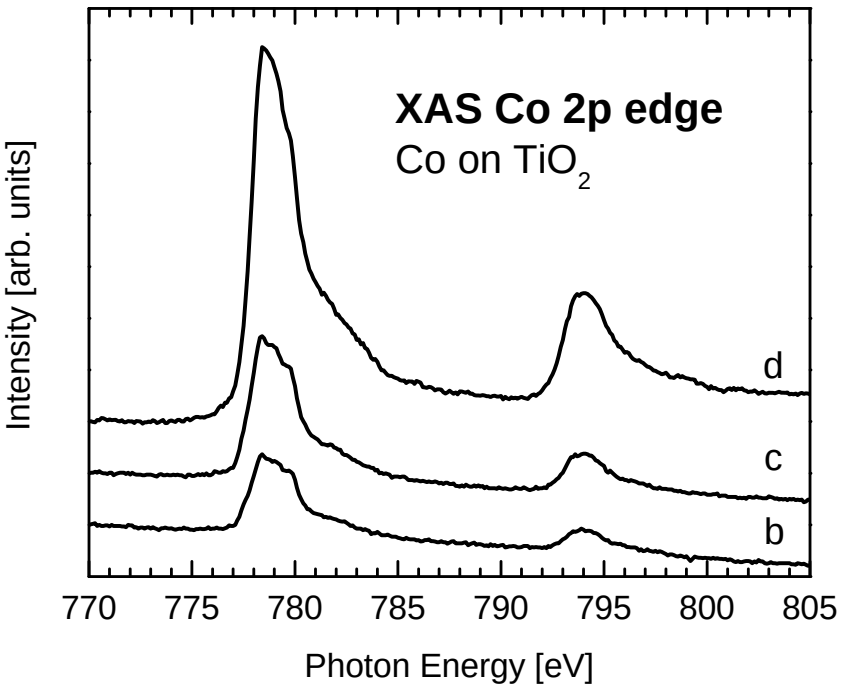

Figure 5.48: Series of XAS spectra at Co 2p edge 0.25 ML Co (curve b), 0.8 ML Co (curve c) and 1.6 ML (curve d) Co deposited on TiO_2

5.4.3 Resonant Photoemission results

The resonant photoemission data from the valence band region at the Ti 2p and Co 2p edges are shown in Fig. 5.49. In curves b, before and at the Ti 2p edge (5.49(a)), the result is very similar to the findings from the very first chromium deposition step (Fig. 5.39(a)). Again, at the Ti 2p edge, resonance in the band gap at -0.7 eV occurs, while the intensity of the high energy state is not influenced. The shape of the valence band at resonance is also very similar to that shown in Fig. 5.39(a).

This behaviour does not change when the cobalt layer thickness is increased to 0.8 ML. The shape of the valence band at resonant excitation is essentially the same as in the corresponding spectrum in b, but the intensity difference between resonant and off-resonant excitation is smaller. The intensity of the low energy defect state is the same as well, but the corresponding intensity in the off-resonance spectrum is higher.

This becomes more pronounced in curve d. Here, the intensity difference between resonant and off-resonant excitation of the defect state is significantly smaller. Additionally, it becomes evident that the position in resonant excitation differs from that in the off-resonance spectrum, probably indicating two different states. As it is the case in both previous spectra, the intensity of the high energy defect state does not change.

The resonant spectra at the Co 2p edge (Fig. 5.49(b)) do not show such sharp resonances as seen at the Cr 2p edges (Fig. 5.39(b)). Here, a resonance over the whole displayed energy range is observed rather than limitation to a small energy range or a single defect state. The whole valence band region shows resonance, with the peak at around -5 eV.

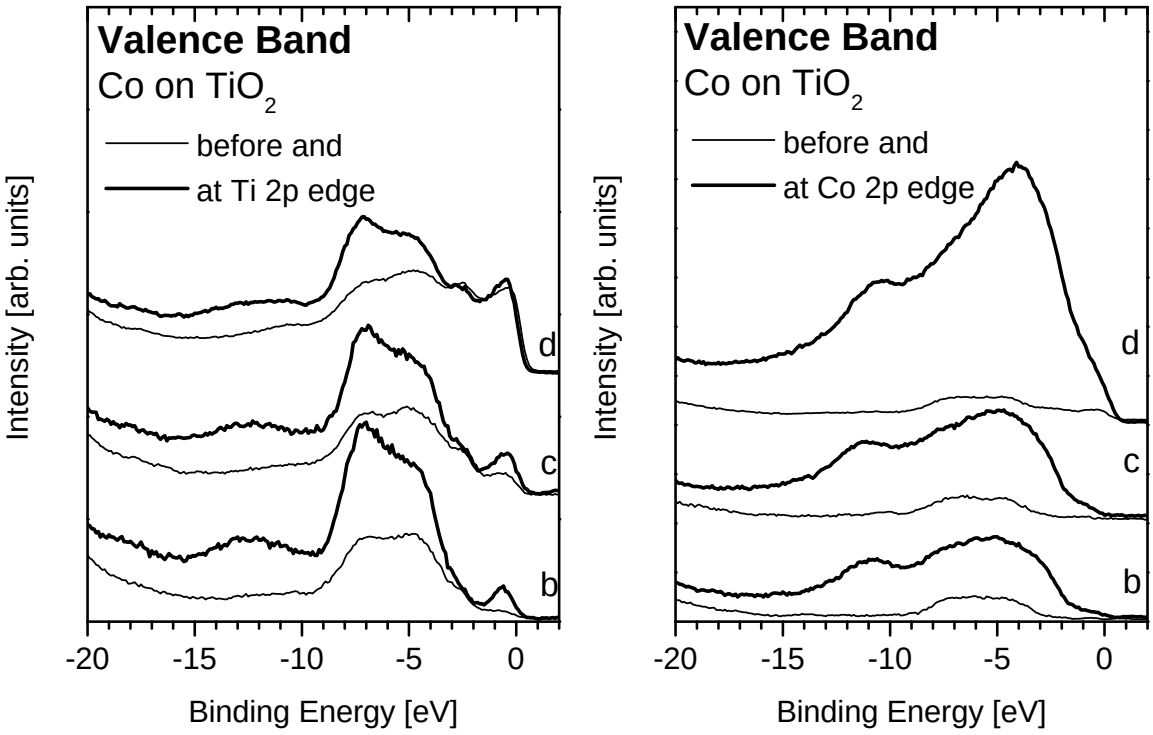

(a) Ti 2p edge

(b) Co 2p edge

Figure 5.49: Series of XAS spectra at Ti 2p and O 1s edges of TiO_2 (a), 0.25 ML Co (curve b), 0.8 ML Co (curve c) and 1.6 ML (curve d) Co deposited on TiO_2

The resonance extends down to -20 eV, but another pronounced peak is found at -11 eV. In the gap region, the emission reaches up to the Fermi-Energy.

In the second deposition step (curve c), this behaviour becomes more pronounced, but the general spectral shape does not change. The last deposition step (curve d) then shows strongly increased intensity at resonance in comparison to curves b and c, where both pronounced peaks at resonance are of comparable peak height. In contrast to this, the low energy peak is now roughly twice as high as the higher binding energy peak. The low energy feature now has shifted to lower binding energy of around -4 eV while the high energy feature does not shift and is still observed at -11 eV. Curve d shows a small additional contribution close to E_F, corresponding to the position of the low energy state at -0.4 eV.

For comparison, the ResPES results of the cobalt metal film are shown in Fig. 5.50, together with the corresponding dataset of 0.25 ML cobalt on TiO_2 (curves b from above). Again, a direct quantitative analysis of both datasets is not adequate. For better visualization, the off resonance spectrum of cobalt metal is magnified by factor of two in comparison to the resonance spectra. This spectrum only shows one prominent feature, the Co 3d emission at around -0.5 eV.

The resonance (I) (medium curve) at the Co 2p edge, causes an increase of the peak intensity in the valence band region by a factor of roughly 16. The most prominent feature

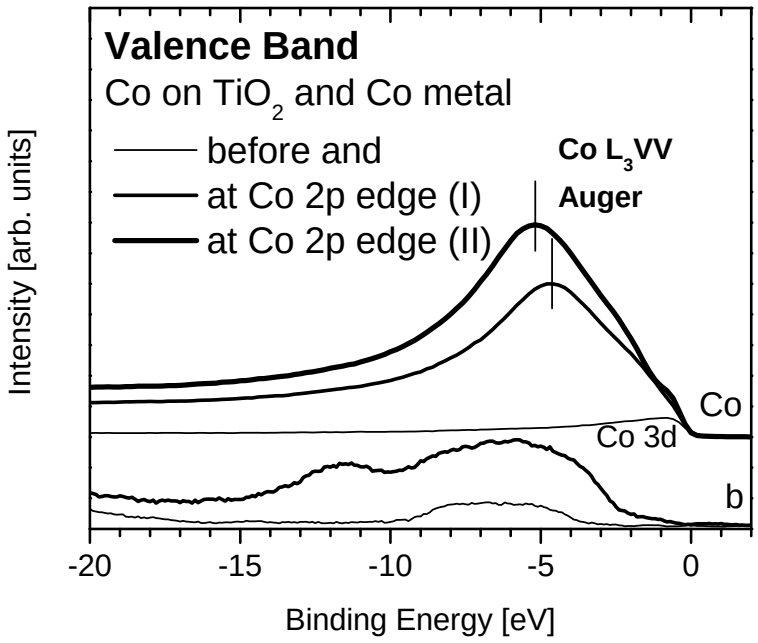

Figure 5.50: Valence band spectra of 0.25 ML Co on TiO_2 (b) and Co metal (Co) off resonance (thin curves), at Co 2p (I) edge (778.4 eV, intensity maximum in TEY XAS of 0.25 ML Co on TiO_2 at Co 2p edge, medium curves) and Co 2p (II) edge (779 eV, intensity maximum in TEY XAS Co metal, bold curve)

in the first spectrum is the broad peak, which is similar to that observed in cobalt on titanium dioxide at the Co 2p edge. It is located at -4.6 eV and its Auger-like character is revealed when the excitation energy is increased to 779 eV. This energy is chosen because it represents the maximum emission intensity of this feature. Now, this peak shifts to higher binding energy by the same energy difference (0.6 eV), which proves that it has a fixed kinetic energy of 773.8 eV. This Auger line is the Co $L_3M_{4,5}M_{4,5}$ Auger.
The difference between the resonant spectrum of the metal and the 0.25 ML Co on TiO_2 is the absence of the high energy contribution at around -11 eV, and the smaller width of the Auger contribution. Close to E_F, a small shoulder is observed, similar as it is the case in the resonant spectrum in curve d.
As it is already mentioned, the low-α mode of the storage ring does not allow to measure CIS spectra with a good signal to noise ratio. In order to study the resonances in more detail and allow comparison of XAS spectra in TEY mode with corresponding CIS spectra, one additional Co-TiO_2 sample is prepared and analysed in the normal multi-bunch hybrid operation mode. The layer thickness is comparable with that of curves b from above. The valence band spectrum of this film is shown in Fig. 5.51, and the binding energy positions that are chosen for the measurements of the CIS spectra are indicated.
The CIS spectra at the Ti 2p (Fig. 5.51(b)) edge are similar to the earlier shown datasets, and are not discussed in detail again. The resonant behaviour of gap state 2 has to be analysed very carefully. In the resonant valence band spectra (curves b and c) in Fig.

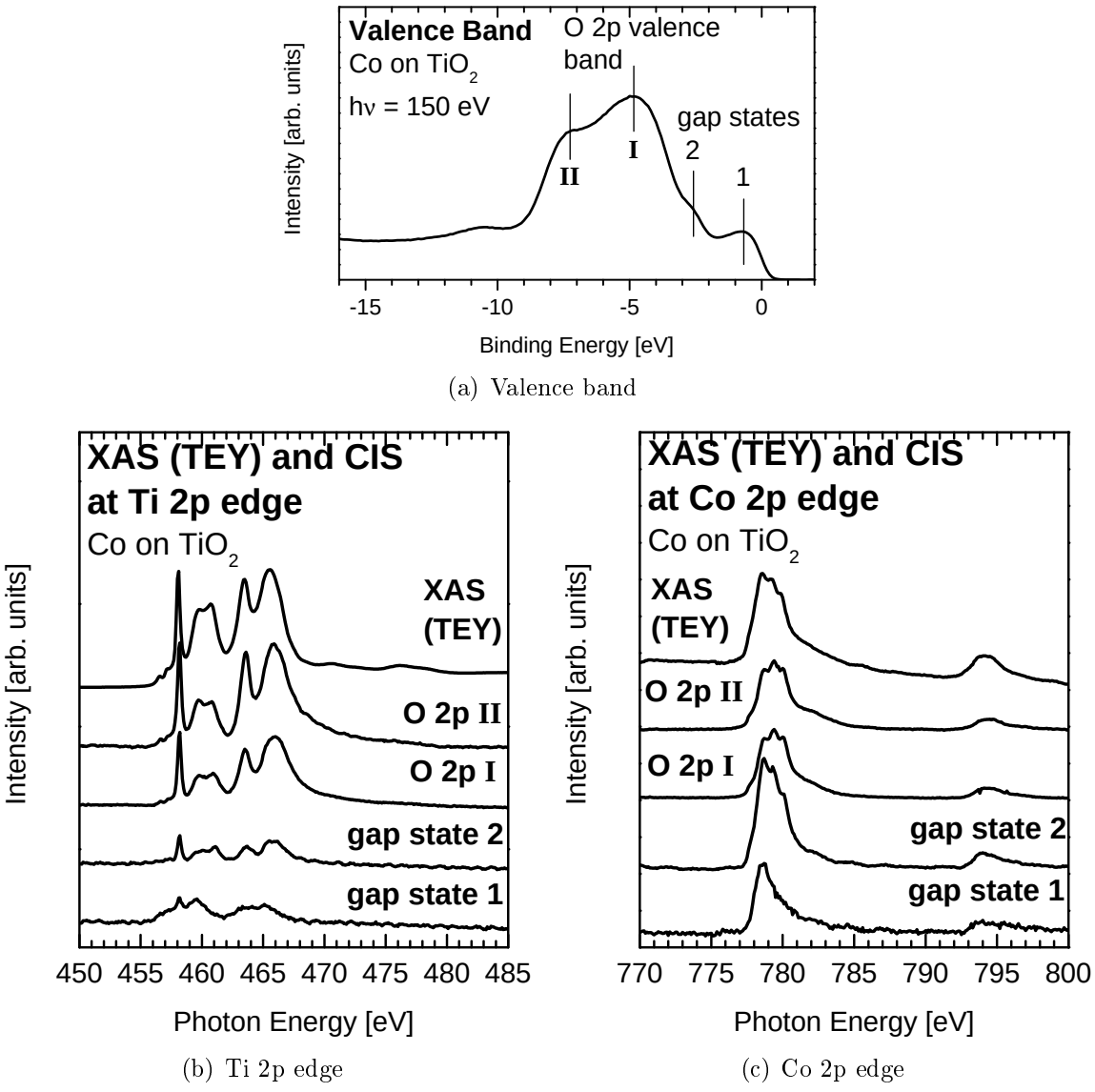

(a) Valence band

(b) Ti 2p edge

(c) Co 2p edge

Figure 5.51: XAS spectra in TEY mode (top) and constant initial state (CIS) spectra at the gap states and the valence band features at Ti 2p edge (left), and Co 2p edge (right). The energy positions are marked in the valence band spectrum in the top panel in Fig. 5.51(a)

5.49(a), it is visible that this state shows only small variation of the intensity, when the excitation energy is set to the Ti 2p edge. The observed resonance in the CIS spectrum can now be interpreted as a crosstalk between this gap state and the broad valence band, which is very close to this state. In contrast to the valence band states, the CIS spectrum of gap state 1 shows significant differences. First, it should be noted, that the onset of the edge is observed at lower photon energies than in case of the XAS spectrum. In the CIS spectrum, there is still contribution from the first prominent feature that is seen in the XAS spectrum at 457.9 eV, although the relative intensity is lower than in case of the XAS spectrum or the valence band CIS spectra. Besides this, the CIS spectrum is very similar to the CIS spectrum of the gap state in clean TiO_2, shown in Fig. 5.21.

For the analysis of the CIS spectra at the Co 2p edge, the properties shown in Fig. 5.50

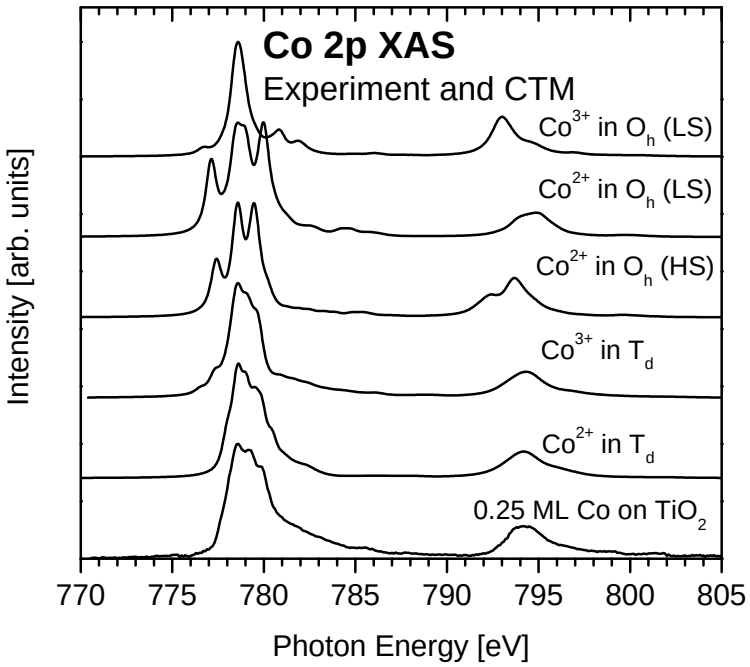

Figure 5.52: Experimental Co 2p XAS spectrum of 0.25 ML Co on TiO_2 (bottom), CTM calculations of Co^{2+} and Co^{3+} in T_d and O_h symmetry (see text for detailed description of the parameters)

have to be considered. The resonant spectra showed a very strong and broad cobalt Auger contribution in the energy range of the valence band. This means that a detailed distinction between cobalt Auger contribution and valence band resonance is not possible by only the two datasets.

The CIS spectrum of gap state 2 follows the XAS spectrum closely, with basically the same fine structures. In contrast to this, the CIS spectrum at gap state 1 differs significantly from the XAS spectrum. The width of the L_3 part of this spectrum is smaller, as it consists of only one asymmetric feature, whose peak energy corresponds to that of the first XAS feature. In contrast to the XAS spectrum, the L_2 only shows the onset at 792 eV with asymmetry at the high energy side, but no clearly pronounced peak is visible.

5.4.4 Multiplet Charge Transfer Calculations

Oxidation state	Symmetry	10 Dq	Δ
Co^{3+}	O_h (Low Spin)	2 eV	3 eV
Co^{2+}	O_h (Low Spin)	1 eV	3 eV
Co^{2+}	O_h (High Spin)	2 eV	3 eV
Co^{3+}	T_d	-0.25 eV	3 eV
Co^{2+}	T_d	-0.3 eV	6 eV

Table 5.6: Parameters for the cobalt CTM calculations, U_{pd} is chosen as 8 eV, U_{dd} as 6 eV

In order to get more insight in oxidation state and local symmetry of the oxidized cobalt

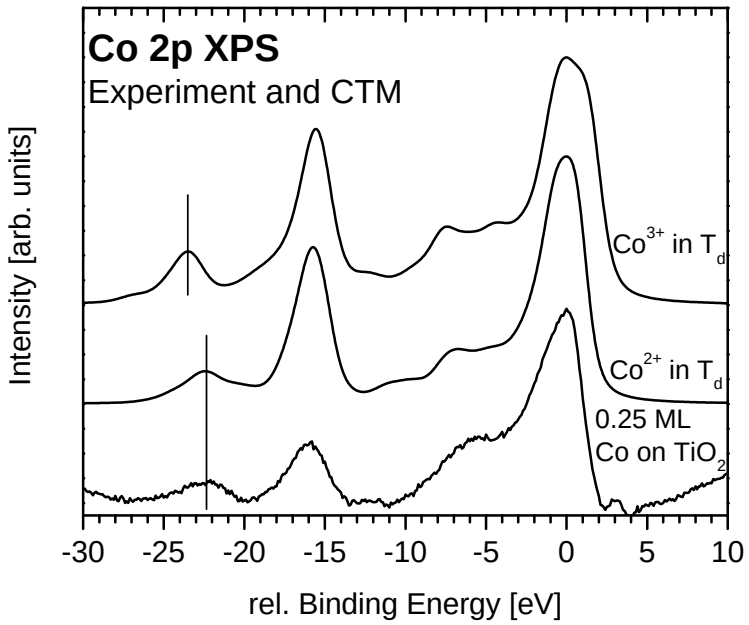

Figure 5.53: Calculated XPS spectra of Co^{3+} (top) and Co^{2+} (middle) in T_d symmetry, together with the experimental spectrum of o.25 ML Co on TiO_2 (the metallic Co-component is removed for better visibility)

component, CTM calculations (XAS and XPS) are carried out, and the results are compared to the experiment. As the signal-to-noise ratio of the low-α results is low, the additional spectrum that is recorded in the normal multi-bunch operation is chosen. The parameters of the calculation are listed in table 5.6.

The parameters of Hollmann et al. [104] are used as a guideline to define the high and low spin states. The parameters U_{pd} and U_{dd} are also chosen according to the authors.

The Co^{3+} in O_h symmetry with high spin is omitted, as according to literature [39, 104] this state only occurs when a very small 10 Dq is chosen (around 0.5 eV), corresponding to weak ligand field. Similar to this, only the high spin state in T_d symmetry is considered, as the transition to the intermediate spin occurs at unrealistic high values for 10 Dq_t. Distinction between high and low spin state of Co^{2+} in T_d symmetry is obsolete, as there is only one possibility to distribute seven d electrons in the orbitals in agreement with Hund's rule. The low spin states can only be realized by a violation of Hund's Rule.

The results of the CTM calculation show that the existence of either oxidation state in octahedral coordination is immediately ruled out. On the other side, both calculations in T_d symmetry show agreement with the experimental spectrum. The main features of the L_3 edge are well reproduced. This also applies for the broad contribution at the high energy side of the L_3 edge. The discrepancy is observed in case of Co^{3+}, where a well pronounced pre-edge structure at around 777 eV is observed in the calculation, which is absent in the experiment.

The calculated XPS spectra of Co^{2+} and Co^{3+} in T_d symmetry are shown in Fig. 5.53, with the same parameter set as for the corresponding XAS calculations in Fig. 5.52. The

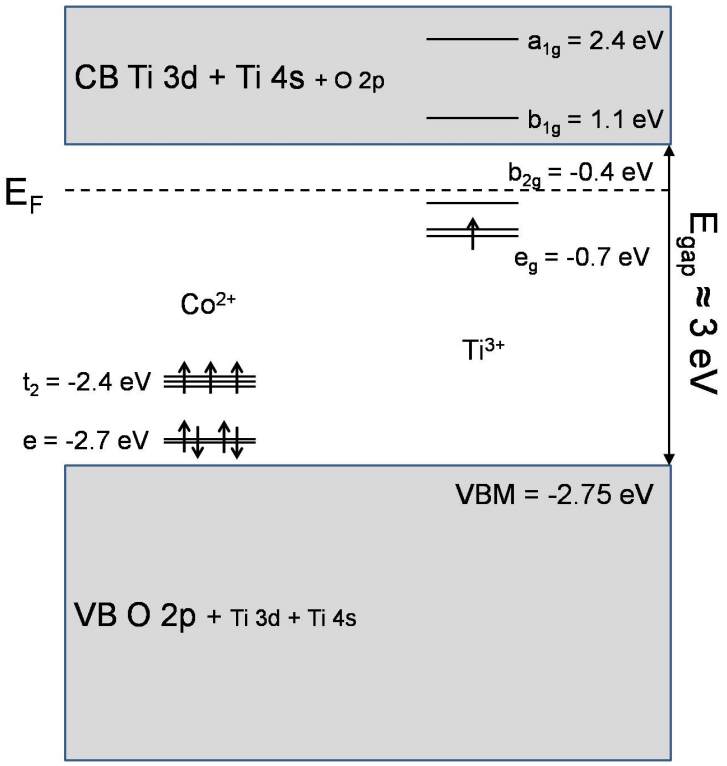

Figure 5.54: Energy level diagram of the Co 3d and Ti 3d states, derived from the CTM parameter 10 Dq. In comparison to O_h symmetry, the order of the e and t_2 states is reversed.

energy is referenced to the peak position of the $2p_{3/2}$ main line. For better visibility, the metallic contribution has been removed from the experimental spectrum (bottom). An artefact of this procedure remains at 3 eV rel. binding energy, but without influence on the discussion.

As it is the case in the XAS calculations, the agreement between calculation and experiment is good in both cases, while only minor differences are found. The spin-orbit split of the experimental spectrum is well reproduced, as well as the satellite structures, of which the $2p_{3/2}$ satellite of Co^{3+} exhibits more fine structure than that one of Co^{2+}, but the positions are reasonable. The important difference is found in the $2p_{1/2}$ satellite. While that one in the Co^{2+} spectrum coincides with that from the experimental one, the Co^{3+} satellite shows a separation, which is 1 eV higher.

Similar as for clean TiO_2 and the oxidized chromium on TiO_2, an energy level diagram that shows the relations of the different energy states to each other, can be derived from the CTM parameter set. This scheme is shown in Fig. 5.54. Due to the small crystal field split in the T_d symmetry, a difference of only 0.3 eV is found between the t_2 and e states. The distribution of the electrons among the d-states is done with respect to Hund's rule. The two low energy e states are occupied by paired electrons, while the higher energy t states are occupied by three unpaired electrons.

5.4.5 Summary of cobalt deposition on titanium dioxide

The binding energy positions from the photoemission experiments are briefly summarized in table 5.7. The results from the photoemission experiments are as follows:

Line	binding energy	separation to Ti $2p_{3/2}$
Ti $2p_{3/2}$, Ti^{4+}	-458.9 eV	0 eV
Ti $2p_{3/2}$, Ti^{3+}	-457.3 eV	2.6 eV
Ti $2p_{1/2}$, Ti^{4+}	-464.6 eV	-5.7 eV
Co $2p_{3/2}$, Co^{0}	-778.2 eV	-319.3 eV
Co $2p_{3/2}$, Co^{x+}	-781 eV	-322.1eV
O 1s, mainline	-530.4 eV	-71.5 eV
gap state 1 (Ti 3d)	-0.7 eV	458.1 eV
gap state 2 (Co $3d_{Ox}$)	-2.7 eV	456.2 eV
Co $3d_{metal}$	-0.4 eV	458.5 eV

Table 5.7: Overview of photoelectron spectroscopy results of cobalt deposition on TiO_2 thin film

- The Ti $2p_{3/2}$ line shows an additional low binding energy feature, which reflects Ti^{3+}.
- When the cobalt overlayer thickness has reached the maximum value, the intensity of the Ti $2p_{3/2}$ line decreases to 49% of the initial value.
- The spectral shape of the O 1s line emission does not change with increasing overlayer thickness, and the decreasing behaviour is the same as that of the Ti 2p line. At maximum cobalt thickness, the intensity of the O 1s line decreases to 54% of the initial value.
- The Co 2p line consists of two components in the initial step of growth. The intensity of the metallic component increases with increasing layer thickness.
- The valence band spectra show two defect states in the initial state. With increasing overlayer thickness, a development to Co 3d dominated emission is observed.
- The spectral shape of O 1s and Ti 2p XAS is not affected by cobalt deposition.

Chapter 6

Discussion

In this chapter, the results will be discussed in detail. In the first section, the focus will be on the properties of the TiO_2 samples. In the following section, the interaction between chromium and TiO_2 will be described, with focus on the post-oxidation. This will be followed by the interaction between cobalt and TiO_2, where the focus is on the identification of the oxidized component.

6.1 Titanium dioxide

In this section, the results obtained from TiO_2, both the crystal and the thin film, are compared with each other, and conclusions on stoichiometry and defect states will be drawn. The discussion will be supported by the CTM results, where applicable.

6.1.1 Stoichiometry, structure and defect states of Rutile (110) and thin film sample

The first question to address in this section is the influence of the different preparation procedure, described in section 4.1, which differs significantly from the methods described in section 2.1.1.
As the annealing steps are carried out in ambient air, oxidizing conditions are present, which are necessary conditions for the preparation of stoichiometric oxides. In Fig. 4.1 it is visible that as a consequence of the annealing in UHV conditions, the stoichiometric crystal becomes reduced, which is deduced from the changed color [1, Fig. 5]. The stoichiometry of the sample's surface region, which is monitored in PES experiments, is restored by the annealing procedure in ambient air. This is indicated by the low FWHM of 1.1 eV of the Ti $2p_{3/2}$ line, as it is shown in Fig. 5.2(a). Essentially the same result is evident in case of the thin film sample in Fig. 5.17(a), where the only difference is the fact that this sample is prepared out of a metallic film rather than a slightly reduced crystal.

Each spectrum shows only one contribution at -459.3 eV (Rutile, Fig. 5.2(a)) respectively -458.9 eV (thin film, 5.17(a)). The overview spectrum in Fig. 5.1 in addition shows negligible amounts of carbon, which is a consequence of the high temperature annealing step as well. The high temperature of roughly 800°C in combination with the oxygen atmosphere is also capable of oxidizing carbon contaminations to volatile compounds.
Stoichiometry of the crystalline sample is also indicated by the absence of a pronounced in-gap emission (Figs. 5.2(d) and 5.8), which is reported in literature for slightly reduced samples [1, 95, 96]. In contrast to this, such an in-gap state with binding energy of -0.7 eV is found for the thin film sample in the ResPES at the Ti 2p edge (Fig. 5.20). As described in the introduction (Section 3.4), resonance of the photoemission intensity requires a direct photoemission channel and an auto-ionization channel that both interfere constructively. The absence of the direct photoemission channel from a Ti $3d^1$ state in the Rutile crystal consequently rules out the resonance. In contrast to this, there are occupied Ti $3d^1$ defect states in the thin film sample that give rise to interference of both channels at the Ti 2p edge, as it is shown in Figs. 5.20 and 5.21. The origin of the emission above the extrapolated valence band edge of Rutile is not clear, but as the ResPES experiment shows, defect states can be ruled out, as no resonance in the gap region is observed.
The extrapolated position of the valence band maximum in Rutile (110) is -2.6 eV, as obtained from a linear fit of this edge (shown in Fig. 5.2(d)). While the VBM of the thin film shifts to higher binding energy of -2.75 eV, the Ti 2p line shifts to lower binding energy of -458.9 eV in case of the thin film. The shift of the VBM by 0.15 eV to -2.75 eV can be explained by donor-like surface defects that cause n-type doping, which shifts the VBM downward with respect to E_F. This is described by Diebold in [1, Fig. 35]. In contrast to the valence band spectra, the Ti 2p core lines are measured in a more bulk-sensitive mode, where this shift may not be obvious any more. Additionally, it has to be pointed out that one sample is crystalline Rutile, while the second one is more likely a polycrystalline sample composed of Rutile and Anatase. Consequently, the shifts can be assigned to have two different origins. On one side, the donor-like nature of the defect states, on the other side a different valence band structure of Anatase in comparison to Rutile.
The position of the O 1s mainline at -530.6 eV (shown in Fig. 5.2(b)) in the crystalline sample also shows good agreement with literature [1], which is a further proof for stoichiometry. The difference between the binding energies of the crystal and the thin film is 0.3 eV, which is a negligible difference to the shift of the respective Ti $2p_{3/2}$ lines, which is 0.4 eV. The additional contribution at the high energy side, separated by 1.4 eV in Rutile, is clearly assigned to a surface-related feature, as its relative intensity compared to the main line increases from 0.15 to 0.29, when the mode is changed from bulk to surface sensitive measurement. In the literature, this high binding energy feature is reported in the work of Bullock et al. [91], and Perron et al. [92], where this feature is assigned to the

2-fold coordinated oxygen atoms of the bridging rows of the Rutile (110) surface. According to Perron et al., adsorbed water molecules are reflected by a component in the O 1s spectrum that is separated by 3.8 eV with respect to the main line. On the hydroxylated surface, an additional component with a separation of 2.4 eV is found (Bullock et al., [91]), respectively 2.7 eV as reported by Hugenschmidt et al. in [105]. Consequently, the existence of both adsorbed and dissociated water on top of the Rutile surface is ruled out. The absence of molecular water corresponds well with the high temperature annealing step, which is carried out for both samples, in which they are heated to temperatures of ≈800°C. The temperature of each sample is still well above 100°C when they are inserted into the entry lock, which is immediately evacuated. Thus, the assignment of the high energy shoulder at -532 eV (Rutile), respectively -531.6 eV (thin film) to under-coordinated oxygen at the surface is reasonable. This allows the conclusion that the thin film sample exhibits more under-coordinated oxygen, as the relative intensity of this component is 0.6 in comparison to the mainline (bulk sensitive measurement) and thus significantly higher than in the corresponding spectrum of Rutile. This can be related to a higher surface area of a polycrystalline sample in comparison to a single crystal.
The x-ray absorption spectra of Rutile in Fig. 5.6 and the thin film in Fig. 5.18 reveal different spectral shapes at both the Ti 2p and O 1s edges. From this it is concluded that the thin film sample is not converted to Rutile completely, although some Rutile is expected due to the high temperature step. The composition respectively the Rutile to Anatase ratio cannot be concluded, as the Anatase XAS spectra that are found in literature ([1, 73, 97, 98, 99]), exhibit significant differences between each other. Such studies require availability of well-defined single crystalline Anatase, which has to be grown by epitaxy, as e.g. described by Hengerer et al. in [32]. As shown by Zhang and Banfield in [33], Anatase is metastable and converts to Rutile, with a conversion rate depending on the particle size. According to the authors, Anatase nano particles are more stable than Rutile nano particles. This is also in agreement with the results from Gallardo et al. [25], where the transition rate from Anatase to Rutile was found to depend on the particle size and specific surface area. This leads to the conclusion that the thin film contains Anatase crystallites. The XLD results of the thin film (Fig. 5.19) show a dependence of the x-ray absorption from the orientation of the sample surface with respect to the $\vec{E}$. This shows on one side that the structure of the thin film is not amorphous, and on the other side it shows that the various possible orientations are not distributed statistically, although the XLD signal is not as strong as in case of the Rutile crystal.
Resonant PES allows to draw conclusion on the pDOS, in this case the Ti 3d-derived pDOS in the valence band is of interest. The observations made in case of the crystal and the thin film are very similar. For this reason, the discussion of the ResPES results is done in parallel. The higher resonance intensity of the O 2p **II** component of the valence band in comparison to the O 2p **I** component, which is shown in Figs. 5.8 and 5.20, indicates

the higher contribution of Ti 3d to the valence band **II** component, which is explained by stronger covalent overlap of the Ti 3d and O 2p orbitals. A suitable model to explain this observations is the molecular approach, in which linear combinations of the atomic orbitals are used to construct bonding and non-bonding molecular orbitals. The covalent overlap between Ti 3d and O 2p orbitals is stronger when a 3d orbital points directly towards a ligand. As the O $2p_{x,y,z}$ orbitals are aligned along the x, y, and z-axes, higher covalent overlap is achieved for the e_g subset ($3d_{x^2-y^2}$, $3d_{z^2}$), if the deviation from O_h is neglected, which is reasonable for qualitative description. Otherwise, the symmetry of the orbital changes, but the index e.g. $3d_{z^2}$ is valid anyway. These orbitals form σ-type bonds, while the orbitals with t_{2g} symmetry form π-type bonds, which have higher energy than the σ-bonds. This also allows the conclusion that the valence band component **II**, at higher binding energy of $\approx$ -7 eV, reflects σ-bonds, while the component **I** reflects the π-bonds. In the empty orbitals (i.e. anti-bonding orbitals) the ordering is reversed, which means that the $\pi*$ orbitals have lower energy than the $\sigma*$ orbitals. In general, the same conclusions on covalency can be drawn from the analysis of the 3p ResPES results, shown in Fig. 5.23, where the resonance of the O 2p **II** part is stronger as well.

The CTM calculations of the Ti 2p-3d XAS, shown in Fig. 5.12, allow reasonable fitting of the experimental results. The comparison of the dataset shows that already with the assumption of a pure ionic interaction, the main features of the XAS spectra can be reproduced. However, in order to receive agreement for the satellite structures, CT states i.e. the covalent contribution has to be taken into account. It is an interesting point that when the CT states are enabled, the value of 10 Dq has to be reduced from 1.7 eV to 1.5 eV in order to yield the same splitting of the main lines of the XAS spectrum. Covalent bonding means higher probability of finding an electron in a Ti 3d orbital than in case of ionic interaction. This leads to a higher coulomb repulsion by which in return requires an adaption of the (ionic) 10 Dq value.

Comparison between the experimental spectrum and the calculated energy positions of the empty Ti 3d states (Fig. 6.1) shows good agreement, which allows the conclusion that in a d^0 system the positions of the most prominent features correlate well with the positions of the empty states. Nevertheless, the experimental L_3 XAS shows three peaks while there are five nominally empty 3d orbitals, of which at least two (the e_g subset in D_{4h}, consisting of $3d_{yz,xz}$) are degenerate. In contrast to this, the stick spectrum i.e. all allowed 2p-3d dipole transitions including the CT states, shows 134 allowed transitions with finite intensity, although only few states contribute significantly to the spectrum. The low width of the first peak may also be seen as an indication for a 3-fold degeneracy of the respective states. The observed mismatch is due to the deviation of the real local symmetry of the [TiO_6] octahedron in Rutile from the model of D_{4h} symmetry that is applied for the calculations.

In contrast to the observations at the Ti 2p edge, the 3p resonance occurs at energies well

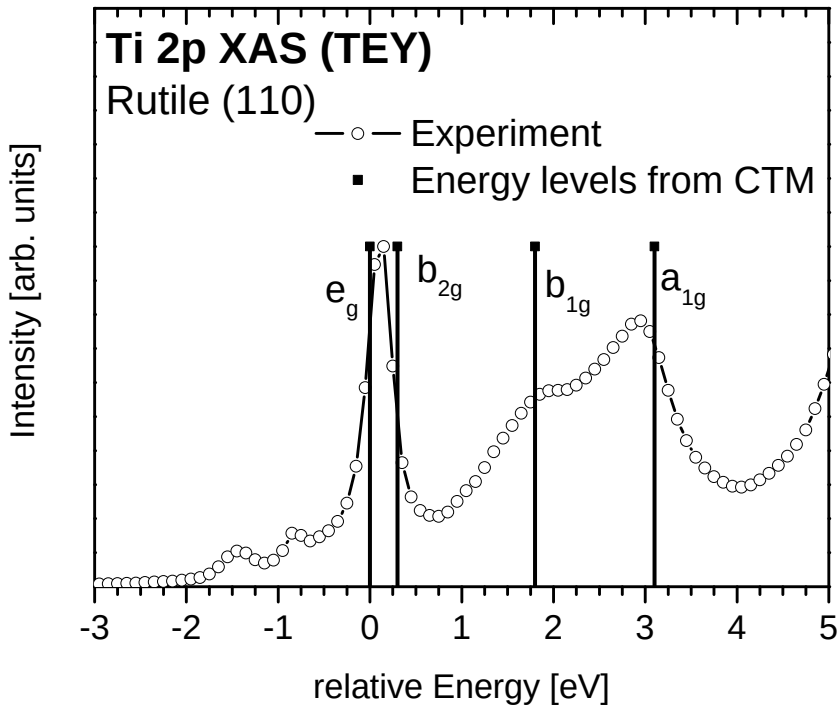

Figure 6.1: Experimental Ti 2p XAS of Rutile (110) (circles), and the relative positions of the 3d states derived from the CTM parameters 10 Dq, Ds and Dt

above the ionization threshold of the 3p line, which is ≈ 42 eV (E_{bind} ≈37 eV, Φ ≈ 5.5 eV, [55]). Similar results were shown by Nakajima et al. [56] (Cr on TiO_2) and [89] (Fe on TiO_2), where the intensities of Ti 3d and Cr 3d respectively Fe 3d derived defect states as a function of the excitation energies around the 3p edges were examined. The highest intensity for the Ti 3d states was found well above the ionization edge of the 3p lines as well. Kotani and de Groot described the fundamental differences between the 2p-3d and 3p-3d absorption in the 3d transition metals [81], although both excitations have the same symmetries. The atomic exchange interaction (the Slater-Condon-Parameter F^2), which is higher in case of 3p-3d than 2p-3d, is responsible for the different intensity distribution, as the energy separation of the different J-terms depends on F^2. The parameters F^2 are found in the output files of the CTM program, in case of Ti 2p-3d this value is 6.3 eV, while for Ti 3p-3d this value is 11.1 eV.

According to the excitation energy at which the resonance respectively the highest absorption is observed, the respective final is shifted into the vacuum, as also stated by Barth et al. [106], who named this the "far continuum". The high width of this part indicates a low lifetime of the corresponding state, which in return agrees with the findings of Barth et al. [106], that the corresponding final state is in the continuum.

Essentially the same is visible in the ResPES dataset of metallic titanium in Fig. 5.24. The increasing contribution of adsorbed oxygen does not influence the discussion, as the properties of metallic titanium are reflected by the Ti 3d states close to E_F. The onset of the 3p3d3d-Auger at photon energy of 32 eV corresponds well with the binding energy

of the 3p line in titanium metal, which shows that the 3p-3d absorption edge is at 32 eV. This is the minimum energy to create a 3p hole by excitation of a 3p electron into an empty state above E_F, which subsequently enables the 3p3d3d sCK Auger. In contrast to that, the highest absorption, reflected by the highest electron emission intensity, occurs at photon energy of around 45 eV, which is also well above the ionization potential of the 3p line, as it is the case for TiO_2. These findings are additional indications for the atomic nature of the XAS process, which is also evident in the metal.
Comparison of the 3p-3d CTM calculations in Fig. 5.26, with the 2p-3d CTM in Fig. 5.12 does not only show different intensity distributions, but also much higher sensitivity on changes of the local symmetry from O_h to D_{4h} in case of the 2p-3d XAS.

6.1.2 The role of the charge transfer states

The influence of the charge transfer states can be analysed in detail when the PES and XAS (Figs. 5.2(a) and 5.6(a)) experiments are analysed in combination with CTM calculations (Figs. 5.12 and 5.15). Besides the shift of the binding energy, the Ti 2p photoemission spectra of the film and the single crystal do not show significant differences, which makes the approach of a parallel discussion of both spectra reasonable. As the attempts of simulating XAS spectra of the thin film did not yield reasonable results, this is excluded from discussion, but it is assumed that the qualitative bonding properties are very similar in both systems.
CTM calculations of Ti 2p XPS did not reveal any changes, when the local symmetry was reduced from spherical to O_h and D_{4h}, which shows that photoemission of the core levels is not as sensitive on the local symmetry as x-ray absorption. In all three cases, only two final states i.e. the $2p_{3/2}$ and the $2p_{1/2}$ core hole are allowed, which corresponds to the single particle description, according to de Groot [81]. The increased width of the $2p_{1/2}$ line when the CT is switched on, is caused by additional contribution from more final states, while the $2p_{3/2}$ line still consists of one final state only. Although the CT states are allowed, no pronounced satellite features are visible. The attractive force of the core hole potential U_{pd} shifts electrons from the valence band into 3d states, which results in the well visible satellites at around -10 eV rel. binding energy.
Besides the charge transfer as a consequence of the presence of a core hole at the titanium atom, the CT state as ground state, contributing with ≈33% for $\Delta = 3$ eV, is considered in the calculations as well.
In contrast to this, the repulsive U_{dd} potential does not influence position or spectral shape of the satellite features. This is explained by the fact that the photoemission process does not transfer an electron from 2p into a 3d state, but into the vacuum instead. As a consequence of this, the d-d repulsion has no effect in case of a $d^0\underline{L}^0 + d^1\underline{L}^1$ ground state.

Essentially the same conclusions can be drawn from the analysis of the Ti 3p XPS calculations, although the high FWHM of ≈2 eV of the experimental spectrum (Fig. 5.2(d)) makes such a detailed discussion as it is the case for the 2p lines, somewhat difficult. One interesting result is the calculated spin-orbit split of the 3p line, which is ≈680 meV. This value is large enough to be measured in photoemission at a synchrotron, for example in case of the Si 2p line, with a comparable separation. This means that an intrinsic effect, e.g. strong life time broadening, is responsible for this.
Indications for the CT states are also found in the ResPES datasets, where Auger-like features are observed in the binding energy region between the valence band and the O 2s line. The Auger-like character is evident, as the binding energies increase when the excitation energies are increased, with a slope of One, which in return means constant kinetic energies. According to the kinetic energies of ≈445 eV (L_3) respectively ≈450 eV (L_2), these Auger channels are assigned to the Ti 2p3d3d Augers. This is a strong contradiction to the nominal d^0 configuration of Ti in TiO_2, as the described Auger requires two electrons in 3d-orbitals of one atom. Although the $d^2\underline{L}^2$ CT state, which is required to enable this described Auger channel, is not included in the CTM calculations, it has to be considered. As Okada and Kotani [107] described, a ground state of TiO_2 that consists of 39.5% $d^0\underline{L}^0$, 48.1% $d^1\underline{L}^1$ and 12.3% $d^2\underline{L}^2$ CT states, yields good agreement for experiment ant theory. Instead of Ti 2p3d3d Auger, the more precise description Ti $2p3d_{CT}3d_{CT}$ Auger should be preferred. The fact that these Auger-like features are observed in both cases i.e. in the single crystal without gap states, and the thin film with gap state contribution, shows that these Auger channels are not related to the occupied defect states. Besides this, the defect states have Ti $3d^1$ character, which is not sufficient to enable the a Ti 2p3d3d Auger.

6.1.3 Coster-Kronig process

The higher FWHM of the Ti $2p_{1/2}$ line can be analysed in combination with the calculated XPS spectrum. The stick spectrum shows that the Ti $2p_{3/2}$ line consists of only one final state, while the main contribution of the Ti $2p_{1/2}$ consists of two lines, separated by 0.54 eV. The constant broadening of the stick spectrum instead does not explain the roughly two times higher FWHM of the experimental Ti $2p_{1/2}$ line in comparison to the $2p_{3/2}$ line. This is directly related to the two resonances in the L_3 Auger line that occur at both the L_3 and L_2 edges. The responsible mechanism is the resonant Coster-Kronig process, which transfers the L_2 hole that is created at the L_2 edge, into an L_3 hole. This L_3 hole subsequently decays via the same channel as the resonant L_3 Auger. The energy difference between these two states, which corresponds to the spin-orbit split of 5.7 eV, is possibly transferred to either the previously excited electron, or to valence electrons. The energy is sufficient to eject the excited electron from the conduction band, but with

a very low kinetic energy, as $\Phi \approx 5.5$ eV. This electron vanishes in the background and cannot be detected by photoemission. Another possible channel is thermalisation of the energy by valence electrons.
Detailed examination of the involved photoemission final state ($2p^5$) yields two distinct J states with total angular momentum of $J = |L - S| = 1/2$ and $J = |L + S| = 3/2$, with $L = 1$ and $S = 1/2$. This gives rise to the term symbols $^2P_{3/2}$ and $^2P_{1/2}$. During the CK process, the L_2 hole, corresponding to the $^2P_{1/2}$ state, is transferred into an L_3 hole, corresponding to the $^2P_{3/2}$ state. With this message, the CK process respectively the $L_2 \rightarrow L_3$ transition is understood as change of the total angular momentum of the given electronic configuration rather than an electronic transition between two energy levels. This can be interpreted as a change of the alignment between electronic angular momentum and spin from anti-parallel $|L - S|$ to parallel $|L + S|$.
The whole resonant process may then be written as $L_2L_3M_{4,5} \rightarrow L_3M_{2,3}M_{4,5}$ process. X-ray fluorescence can also be ruled out as the origin for the missing L_2 Auger intensity. As the studies of Kurmaev et al. [64] showed, the intensity ratios of L_3:L_2 fluorescence is also far away from 2:1, even at the L_2 edges. Kurmaev et al. give a corrected branching ration between L_2:L_3 of 0.36, far away from the resonance. The expected value from the branching ratios of the 2p photoemission is 0.5.
The possible reason for the absence of the L_2 Auger above the resonance can be due to a transition, in which the energy difference between L_2 and L_3 is transferred to a valence electron, which can be excited into the conduction band. As already mentioned, the spin-orbit split energy of Ti 2p is smaller than the ionization potential of the valence electrons in TiO_2.

6.2 Growth of chromium on titanium dioxide

For the discussion of chromium growth on TiO_2, the post-deposition oxidation, which is shown in Fig. 5.34, has to be taken into account, as the as-prepared state of the sample is not stable but experiences changes of its composition. This process occurs without exposure to additional oxygen, which means that the sample is always stored in the analysis chamber under UHV conditions, with a pressure below 10^{-9} mbar range. For this reason, the discussion will start with the post-deposition oxidation, and will subsequently continue with the properties of the interface region.

6.2.1 Time dependence and post deposition oxidation

The initial deposition of chromium on the clean and near-stoichiometric TiO_2 surface causes an interface reaction, in which Ti^{4+} from the substrate is reduced Ti^{3+}, which is evident from the appearance of the low binding energy component in the Ti 2p PES spec-

tra (Fig. 5.27(a)). This observation is in agreement with the findings from the Diebold group [9], who also followed the changes of the Ti 2p spectra as a function of chromium thickness, and Winde [55]. The reduction of the substrate is accompanied by a partial oxidation of the deposited chromium, which becomes evident from the analysis of the Cr 2p spectrum (b) in Fig. 5.28, where two components at -574.6 eV and -576.4 eV are identified. The resolution of both components is better in case of the 3p spectra, as shown in Fig. 5.30, where the two components are separated by 1.8 eV as well. The metallic chromium component is in contrast to the results from the Diebold group [9], who only found one chromium component in the initial stage of growth, and assigned this component to the Cr^{3+} state, due to its shift to a higher binding energy by 1.7 eV, with respect to the $2p_{3/2}$ line of the metal. Although Nakajima et al. [56] did not apply core level spectroscopy, the authors were able to show the metallic character of Rutile (001) supported chromium by exposure to oxygen. This differences already indicate the crucial role of the surface morphology, as Pan, Diebold et al. used Rutile (110), while Nakajima et al. have chosen Rutile (001). Throughout this thesis, a thin film substrate is chosen, which is most likely polycrystalline, and thus exposes several crystallites with different surface orientations.
In case of the Cr 2p core level spectrum of 0.3 ML Cr in Fig. 5.34(b), the metallic component vanishes during a time of ≈3 hours, and only the oxidized component remains. The Ti 2p spectrum in Fig. 5.34(c) shows that the oxidation of the chromium metal is not realized by further reduction of the TiO_2 support, as the low binding energy component of the Ti $2p_{3/2}$ line vanishes as well, and only the Ti^{4+} component remains. As already shown by Nakajima et al. [56], the exposure of TiO_2 supported chromium to additional oxygen (20 L in this case) leads to vanishing of the two in-gap emissions, which are labelled 1 and 2 here (described in Figs. 5.32(b) and 5.3.3), while the gap emission develops to the valence structure of Cr_2O_3. In contrast to these results, only the interaction between Cr-TiO_2 and the residual gas caused the post oxidation that is reflected by the changes shown in Figs. 5.33, 5.34(b) and 5.34(c). As Fig. 5.33 shows, the post-deposition oxidation is no longer complete, when the thickness has increased to 1 ML, even after a time span of 24 hours has elapsed.
One interesting result is the removal of the carbon contamination, which is seen in the overview spectrum in Fig. 5.34(a). It is known that TiO_2 surfaces are self-cleaning under certain conditions, but it is not clear, in which way the oxidation, as described above, is influenced by the oxidation of the carbon contaminations. For the self-cleaning of TiO_2, water is necessary, which is also present in the residual gas of the UHV system, despite a careful bake out procedure. Water is split into radicals that can subsequently oxidise molecules on the surface, which might also have an effect on adsorbed metal particles. Although adsorbed water on the surface itself is ruled out, as explained in section 6.1.1, the presence of water in the residual gas may be sufficient to promote the oxidation of carbon.

The relaxed Cr 2p XAS spectra indicate bulk-like Cr_2O_3, as the comparison with the reference spectrum in Fig. 5.3.4 shows. The agreement between calculation and experiment is good, despite the rather strong distortion from the D_{4h} symmetry of the [CrO_6] octahedron. The resulting energy level diagram shows a very small δ_2, which means that the lower $3d_{xy}$ and the higher $3d_{yz,xz}$ levels are separated by 0.04 eV only. The high stability of Cr_2O_3 is derived from the very stable, half filled t_{2g}^3 (or e_g^2 and b_{2g}^1 in D_{4h}) configuration.

6.2.2 The growth of chromium on titanium dioxide thin films

The discussion in the previous section shows that at least during the first deposition steps (up to 0.5 ML of chromium), the exposure to residual gas is sufficient to completely reoxidise the surface during a time of few hours. The oxidized component is identified as Cr^{3+}, as the separation of the corresponding $2p_{3/2}$ component is 1.8 eV, with respect to the $2p_{3/2}$ line of the metallic component. The metallic chromium component is evident in the Cr 2p spectra in Fig. 5.28, as well as in the bulk and surface sensitive Cr 3p spectra in Fig. 5.30, where both lines are better resolved. As already mentioned above, the structure of the thin film, which is not single crystalline, is seen as the main reason for the different adsorption behaviour. In case of the bulk sensitive measurement of the Cr 3p line (Fig. 5.30(a) and Table 5.3), the intensity of both components is more or less equal. In contrast to that, the intensity of the metallic component is higher than the oxidized one at -43.8 eV in case of the surface sensitive measurement (Fig. 5.30(b) and Table 5.4). This clearly shows that the metallic component is located on top, while the oxidized component is closer to the interface. The chromium overlayer thickness is calculated by applying the model of uniform layer-by-layer growth to the decrease of the Ti 2p intensity (Fig. 5.29). The good agreement between the Cr 2p intensities and the model of layer-by-layer growth, which predicts an intensity of

$$I\left(d\right) \sim 1 - \exp \frac{-d}{\lambda \cdot \cos\left(\theta\right)}$$

does indicate that layer-by-layer growth is occurring. From these results, the following model of chromium growth on the thin film, illustrated in Fig. 6.2.2, is developed. In the model, the findings from the LEIS experiments by the Diebold group [9] are included. In the very first step of chromium deposition, small islands of oxidized chromium (Cr^{3+}) are formed, and the TiO_2 surface is reduced. According to Pan et al. [9], the coverage is not complete, but only 80% of the surface are covered by oxidized islands. In contrast to the chromium growth on a single crystal, metallic chromium is present (middle panel) already in the very first step of growth. As the metallic component would be oxidized on the clean TiO_2 surface, its location is on the top of the oxidized chromium islands. The position on top rather than at the interface is also indicated by the surface sensitive Cr 3p

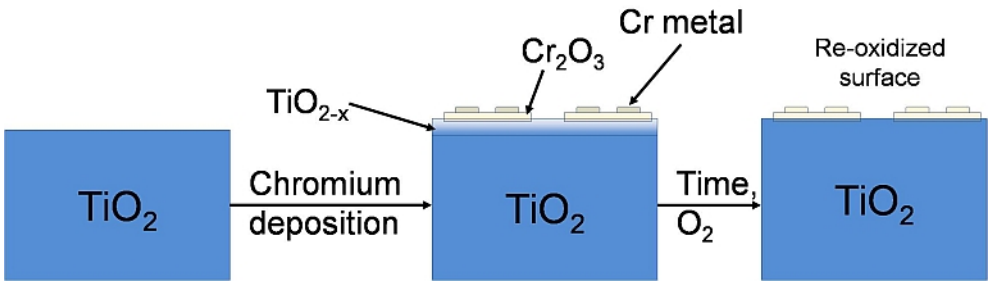

Figure 6.2: Model of the initial step of chromium deposition and the corresponding interface reaction, followed by the post-deposition oxidation

spectra. Due to exposure to oxygen from the residual gas, the surface then is re-oxidized. Due to the quasi-2D growth, during the next deposition steps, adsorption sites on top of the clean TiO_2 are preferred, although in addition the previously described metallic component appears on top of the oxidized islands.
With the discussion from the previous section, the deviation of the oxygen intensity from the model of layer-by-layer growth, which corresponds to

$$I(d) \sim \exp \frac{-d}{\lambda \cdot \cos(\theta)}$$

can be explained as well. One one side, the oxygen extraction, as described by Pan et al. [9], has to be taken into account. The second factor, which is evident from the results shown in Fig. 5.34, is the incorporation of additional oxygen from the residual gas into the material, which consequently leads to higher oxygen content than it is expected from a pure layer-by-layer growth without any further reaction than the redox reaction directly at the interface.
First indication for the complex nature of the interaction between chromium and titanium dioxide were give by Winde [55] in the HR-TEM measurements, where significant intermixing between chromium and titanium dioxide was found, rather than a sharp and well defined interface.

6.3 Electronic structure

Conclusions on the electronic structure of the interface region, together with the partial pDOS, can be drawn from the Cr 2p and Ti 2p resonant PES spectra (Fig. 5.3.3). The focus here is on the properties of the defect states 1 and 2. In the sub-ML regime, both gap states are well distinguishable, as at the Ti 2p edge the low energy gap state 1 at -0.7 eV shows a resonance. The intensity at resonance is stronger than in case of the clean film, as there is now higher contribution from the direct photoemission channel. This resonance is still observed when 1.7 ML of chromium are deposited.

In contrast to this, ResPES at the Cr 2p edge only enhances defect state 2 at -2.3 eV. Upon the first deposition step, the resonance is limited to the defect state only, which indicates the localized nature of this state. With further increasing thickness, the intensity extends down to a binding energy below the valence band of TiO_2, which is as reflection of the more de-localized nature of the valence electrons of the metallic component i.e. the 4s electrons.
The energy level scheme (Fig. 5.42, which is derived from the CTM calculations and the positions of the occupied defect states, is consistent. It shows that only the lowest energy states are occupied, while the higher ones are not. The lowest Cr 3d states with t_{2g} symmetry form the stable t_{2g}^3 configuration. The term t_{2g} is chosen as on one side the symmetry is the result of a deviation from O_h, on the other side the resulting split between the three levels is only 0.04 eV and thus it is neglected. The next-highest occupied energy state is the Ti 3d derived two-fold degenerate e_g subset, while all the higher states are empty.

6.4 Cobalt deposition

The interaction between cobalt and the TiO_2 surface is less intense than the interaction between chromium with TiO_2, which is known from the summary of metal growth on TiO_2 by Diebold [1]. Nevertheless, an interface reaction is evident, as seen in the core level spectra in Figs. 5.43(a) and 5.44. In the first section of this discussion, the interface will be described. In the second part, the discussion will focus on the chemical state of the oxidized cobalt component, which is realized by combination of Co 2p PES and XAS with the Co 2p CTM calculations.

6.4.1 The growth of cobalt on titanium dioxide thin film

The calculation of the cobalt overlayer thickness is realized by application of the model of uniform layer growth:

$$I(d) \sim \exp\left(-\frac{d}{\lambda}\right)$$

As it is known from the studies by the Diebold group [1, 108], and the theoretical description by Campbell [45], the growth mode correlates with the interface reactivity respectively with the surface energies. Campbell predicted that the mid-to-late transition metals form clusters rather than wetting the oxide surface. Nevertheless, this model is suitable for a first order description of the most important differences to chromium on TiO_2.
The weak interaction is reflected by the relative intensities of the Ti^{4+} and Ti^{3+} components, as the intensity ratio does not change, when the cobalt thickness is increased.

In contrast to the observation made in case of Cr-TiO_2, the intensity of the O 1s line now decreases in the same way as it is the case for the Ti 2p line, which shows that no additional oxygen is incorporated into the overlayer. The only chemical interaction between cobalt and substrate occurs in the initial step of growth. As a consequence of the weak but present reduction of Ti^{4+} to Ti^{3+} in the initial step, oxidized cobalt is found besides the metallic component. This is evident from the corresponding core level spectra (Fig. 5.44), where Co^0 is found at -778.2 eV, accompanied by the oxidized component component at -781 eV. This topic will be further discussed in the following section.
The analysis of the valence band spectra (on and off-resonance) indicates qualitative differences in comparison to the case of chromium deposition on TiO_2. Although the amount of Ti^{3+} in comparison to Ti^{4+} is similar in curves b in Figs. 5.27(a) (Cr) and 5.43(a) (Co), the low energy defect state in the band gap region at -0.7 eV (Fig. 5.45(a)) is much better pronounced in case of cobalt than in case of chromium (Fig. 5.32(b). The spectrum at Ti 2p resonant excitation in Fig. 5.49(a) then shows the same properties of the low energy gap state as in case of chromium on TiO_2 in Fig. 5.39(a). The fundamental difference becomes visible when the highest cobalt coverage of 1.6 ML is reached, where the binding energies in off-resonant and Ti 2p resonant excitation are not equal, but lower binding energy of -0.4 eV is observed in the off-resonance spectrum. This allows the conclusion that in curve d in Fig. 5.49(a) two different states are probed. The off-resonance spectrum shows the dominating Co 3d states of cobalt metal, while the Ti 2p resonant spectrum enhances the intensity of the Ti $3d^1$ defect state. This is supported by the observations that are made in case of Co 2p resonant excitation (Fig. 5.49(b)), with the broad resonance from E_F down to -20 eV, which reveals two different components, as concluded from the comparison with the resonant spectrum of the metal in Fig. 5.50. Finally, the CIS spectra at both states at the Co 2p edge indicate different properties for each state. As the high energy state closely follows the XAS spectrum, it can be concluded that it reflects the same properties i.e. it corresponds to the oxidized cobalt component. In contrast to this, the absence of fine structures in the CIS spectrum of the low energy state indicates metallic character. This is also supported by the fact that the low energy state has shifted toward E_F in the valence band spectrum of curve d. From this point of view, the CIS spectrum of the low energy state at the Ti 2p edge reflects the Ti $3d^1$ properties. Finally it can be concluded that there are two different occupied states close to E_F, one is the Ti $3d^1$ state of Ti^{3+}, the second one is the Co $3d^7$ state reflecting cobalt metal. The oxidized cobalt component then is reflected by the high energy defect state at -2.7 eV. The question if there is covalent overlap between Co 3d and Ti 3d cannot be finally answered, as photoemission averages over the probed volume.
The energy level diagram in Fig. 5.54 is consistent as well, as again only the low energy states are occupied. The Co 3d states have the lowest energy, while the next level on the energy axis is the Ti 3d subset with e_g symmetry with one electron.

6.4.2 Oxidation state and local symmetry

In this section, it is intended to identify the oxidation state of cobalt on TiO_2, which is not straightforward, as the chemical shifts from the metal to the Co^{2+} and Co^{3+} oxidation states are small. Additional information, such as satellite separation and spin-orbit split have to be included as well.
McIntyre et al. [109] give a chemical shift of 2 eV for CoO and CoO(OH), 1.9 eV for Co_2O_3, and 3 eV for $Co(OH)_2$. All values are given with respect to the Co $2p_{3/2}$ line in the metal. In contrast to this, Barr [110] gives a shift of 1.9 eV for CoO and 2.7 eV for Co_2O_3, although the latter may be valid for Co_3O_4 rather than Co_2O_3. Finally, Tan et al. [111] give the chemical shifts together with the satellites, which are helpful for the analysis. For CoO, the authors give a shift of the mainline of 2.8 eV, with the satellite having a separation of 7.9 eV. For Co_2O_3, they give a shift of 2.9 eV, with a satellite separation of 6.3 eV, and for Co_3O_4, the observed chemical shift is 2.3 eV, and the satellite separation is 7.5 eV. From this overview, it is not possible to determine the oxidation state, as there discrepancy between the listed energy shifts and satellite separations.
The probability of hydroxide formation (CoO(OH) or $Co(OH)_2$) is very low, as the experiments are done in UHV. Additionally, in the discussion of the O 1s spectra of TiO_2 (Section 6.1.1), the existence of H_2O respectively –OH groups on the surface was ruled out. One has to keep in mind that the published binding energies are valid for the bulk materials, and as Barr pointed out, Co_3O_4 could be present rather than Co_2O_3.
For the analysis, the CTM proved as a valuable tool in order to simulate the Co 2p XAS and XPS spectra and thus get an insight into oxidation state and coordination geometry. The results in Fig. 5.52 show that Co^{2+} and Co^{3+} in O_h symmetry can be ruled out, as there is strong discrepancy between the experiment and CTM calculations. The results indicate tetrahedral coordination instead, with good agreement for both Co^{2+} and Co^{3+} with the experimental spectrum. The only small disagreement is found in the Co^{3+} spectrum, in which pre-edge structures are found at around 777 eV, which do not appear in the experimental spectrum respectively the Co^{2+} CTM spectrum.
The high value of 6 eV for the CT parameter Δ, which is used for the calculation of the Co^{2+} spectra, can be explained by the electronic configuration of Co^{2+}. In T_d symmetry, the 3d orbitals branch into the low energy, 2-fold degenerate e subset, and the 3-fold degenerate t_2 subset. With respect to Hund's rule, the configuration then is $e^4t_2^3$ i.e. the e subset is full, and the t_2 subset is half filled with parallel electron spins. Thus, a CT process has to overcome the energy gap between ligand states and the high energy t_2 subset, plus the energy that is required to place an electron with spin-down in an orbital that is already occupied by a spin-up electron. In contrast to this, Co^{3+} in T_d has high spin configuration with $e^3t_2^3$, with one unpaired electron in the low energy e subset. This means that the CT parameter can be lower, as the transfer energy is reduced by the

amount of stabilization energy of an additional electron in the low energy subset. From the XAS CTM results, the formation of Co^{2+} is considered rather than Co^{3+}.
Additional indications for Co^{2+} are also found in the XPS CTM calculations in Fig. 5.53. While the energy shifts of the satellites with respect to the $2p_{3/2}$ lines are in good agreement for both the Co^{2+} and the $Co_{3/2}$ CTM, differences are visible in the energy range of the $2p_{1/2}$ lines, between -25 eV and -13 eV rel. binding energies. The energy position of the Co $2p_{1/2}$ satellite, at ≈-22 eV rel. binding energy, is better reproduced in case of the Co^{2+} CTM than in case of the Co^{3+} CTM, although the differences between both is only ≈-1.5 eV.
Although the thermodynamic data of ΔH^0 and ΔG^0 in table 6.1 are valid for the bulk compounds only, they can serve as an additional hint for the possible chemical reaction at the Co-TiO_2 interface. The values are taken from [13], and the value of Co_2O_3 is estimated from the values of CoO and Co_3O_4, as a corresponding value for Co_2O_3 is not listed. The equations are normalized to one unit of cobalt in order to allow an estimation of the formed state. The values given in kJ per mol are also converted to eV, which corresponds to the values of ΔH^0 and ΔG^0 if one atom of cobalt is considered rather than one mol. As already mentioned, this first order approach only includes the values of

Reaction	ΔH^0	ΔG^0
2 TiO_2 + Co → Ti_2O_3 + CoO	129.2 $\frac{kJ}{mol}$ (1.35 eV)	127.6 $\frac{kJ}{mol}$ (1.32 eV)
3 TiO_2 + Co → $1\frac{1}{2}$ Ti_2O_3 + $\frac{1}{2}$ Co_2O_3	224.1 $\frac{kJ}{mol}$ (2.33 eV)	128.1 $\frac{kJ}{mol}$ (1.33 eV)

Table 6.1: Overview on the values of ΔH^0 and ΔG^0 for possible reaction between TiO_2 and Co

the bulk and does not consider contributions from the surface energies. Both described reactions are endothermic, shown by the positive value of ΔH^0, which means that they should not run spontaneously. On the other side, the energy that is required to form 1 unit of oxidized cobalt in each case is rather low (1 eV respectively 2 eV) and can be provided by illumination with visible light. Less energy is required for the first reaction, in which Co^{2+} is formed, which is an additional argument that favours the Co^{2+} state rather than the Co^{3+} state.
In summary, several clues are found that support the statement that the oxidized cobalt component on the TiO_2 surface is in the Co^{2+} state. Namely, these are the absence of the pre-edge feature in the Co^{2+} CTM in T_d symmetry, the good agreement of the satellite separations in the corresponding Co 2p XPS CTM, and the thermodynamic consideration that also favour Co^{2+}.
As an example, the bulk-truncated Anatase (101) surface is shown in Fig. 6.3, with the four oxygen atoms forming a distorted tetrahedron highlighted (purple). It consists of two oxygen atoms from the top row in [010] direction (marked with **1**), and two oxygen atoms

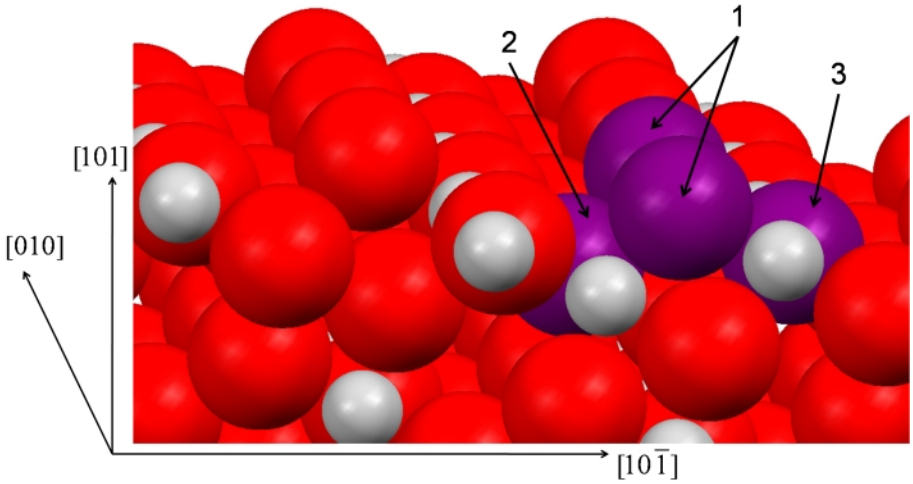

Figure 6.3: Representation of the non-relaxed Anatase (101) surface, the dark spheres highlight a surface site forming a distorted tetrahedron of four oxygen atoms

from underneath this row (**2** and **3**). The distances between two oxygen atoms from the top row is 3.785 Å, the O–O distance between **1** and **2** is 2.801 Å, the **1**–**3** distance is 3.04 Å, and the distance between **2** and **3** is 3.721 Å. The O–O distance in the regular $[Co^{2+}O_4]$ tetrahedron in Co_3O_4 is 3.148 Å. The differences of the O–O distances in the regular $[Co^{2+}O_4]$ tetrahedron and the distorted tetrahedron on the Anatase surface allow the conclusion that this distorted tetrahedron offers enough space to coordinate a Co^{2+} ion. In this argumentation, relaxations and reconstructions of the surface are neglected. As the authors of [57] and [58] did not focus on the very first step of cobalt growth on TiO_2, there is no possibility to compare the obtained results with previous ones from experiments with single crystalline samples.

Summary and Conclusion

The properties of titanium dioxide thin films have been studied and related to the properties of a Rutile single crystal. It turned out that oxidation in ambient air is a suitable step to achieve stoichiometric or near-stoichiometric surfaces. From the properties of the O 1s line of the thin film, polycrystalline morphology with higher surface-to-bulk ratio is deduced. Due to the chosen characterization methods, the influence of the preparation steps in ambient air on the structure of either the crystal nor the thin film is known.
The satellites observed in both photoemission and x-ray absorption have been assigned to a CT state, which is not only caused by the presence of a core hole at the titanium atom. The same origin of both satellites is shown by ResPES, where the photoemission satellite of the Ti 3p line shows higher intensity at excitation energies corresponding to the XAS satellites. The CT states are also indicated by Auger-like features that show the onset at the Ti 2p edges, with kinetic energies corresponding to Ti 2p3d3d Augers. This process is only possible if two d-electrons are present at one atom.

Chromium deposition causes the well-known interface reaction, in which the substrate is reduced and the deposited metal is oxidized. The strong post-deposition oxidation of both the overlayer and the substrate is assigned to effective oxygen adsorption from residual gas on one side, on the other side to a similar mechanism that is described as bulk-assisted re-oxidation. The self-cleaning of the surface is observed as well.

The interaction of cobalt with the TiO_2 surface is found to be much weaker. CTM calculations immediately allow the conclusion that the oxidized cobalt component is located in tetrahedral coordination. Corresponding sites are found on both the Rutile (110) and Anatase (101) surfaces. The oxidation of cobalt on TiO_2 should not run spontaneously from the thermodynamic point of view, but the calculation is carried out for the bulk materials with neglected surface energies. The rather low activation energy of ΔH^0 of 1.35 eV favours the formation of Co^{2+}.

Bibliography

[1] U. Diebold, "The surface science of titanium dioxide," *Surface Science Reports*, vol. 48, pp. 53–229, 2003.

[2] G. van der Laan, "Polaronic satellites in x-ray-absorption spectra," *Physical Review B*, vol. 41, p. 12366, 1990.

[3] F. Morales, F. de Groot, P. Glatzel, E. Kleimenov, H. Bluhm, M. Hävecker, A. Knop-Gericke, and B. Weckhuysen, "In Situ X-ray Absorption of Co/Mn/TiO_2 Catalysts for Fischer–Tropsch Synthesis," *The Journal of Physical Chemistry B*, vol. 108, no. 41, pp. 16201–16207, 2004.

[4] L. Zheng, M. Xu, and T. Xu, "TiO_{2-x} thin films as oxygen sensor," *Sensors and Actuators B: Chemical*, vol. 66, pp. 28–30, 2000.

[5] P.-C. Maness, S. Smolinski, D. Blake, Z. Huang, E. Wolfrum, and W. Jacoby, "Bactericidal Activity of Photocatalytic TiO_2 Reaction: toward an Understanding of Its Killing Mechanism," *Appl. Environ. Microbiol.*, vol. 65, no. 9, pp. 4094–4098, 1999.

[6] C. Tsai and H. Teng, "Chromium-doped titanium dioxide thin-film photoanodes in visible-light-induced water cleavage," *Applied Surface Science*, vol. 254, pp. 4912–4918, 2008.

[7] V. Bondzie, S. Parker, and C. Campbell, "The kinetics of CO oxidation by adsorbed oxygen on well-defined gold particles on TiO_2 (110)," *Catalysis Letters*, vol. 63, pp. 143–151, 1999.

[8] T. Minato, T. Susaki, S. Shiraki, H. Kato, M. Kawai, and K. Aika, "Investigation of the electronic interaction between TiO_2(110) surfaces and Au clusters by PES and STM," *Surface Science*, vol. 566-568, pp. 1012–1017, 2004.

[9] J. Pan, U. Diebold, L. Zhang, and T. Madey, "Ultrathin reactive metal films on TiO_2(110): growth, interfacial interaction and electronic structure of chromium films," *Surface Science*, vol. 295, pp. 411–426, 1993.

[10] I. Bruno, J. Cole, P. Edgington, M. Kessler, C. Macrae, P. McCabe, J. Pearson, and R. Taylor, "New software for searching the Cambridge Structural Database and visualizing crystal structures," *Acta Crystallographica Section B*, vol. 58, no. 3 Part 1, pp. 389–397, 2002.

[11] C. Macrae, P. Edgington, P. McCabe, E. Pidcock, G. Shields, R. Taylor, M. Towler, and J. van de Streek, "*Mercury*: visualization and analysis of crystal structures," *Journal of Applied Crystallography*, vol. 39, no. 3, pp. 453–457, 2006.

[12] C. Macrae, I. Bruno, J. Chisholm, P. Edgington, P. McCabe, E. Pidcock, L. Rodriguez-Monge, R. Taylor, J. van de Streek, and P. Wood, "*Mercury CSD 2.0* – new features for the visualization and investigation of crystal structures," *Journal of Applied Crystallography*, vol. 41, no. 2, pp. 466–470, 2008.

[13] D. Lide, Ed., *Handbook of Chemistry and Physics, 84th Edition 2003 – 2004*. CRC Press, 2003.

[14] A. Vittadini, A. Selloni, F. Rotzinger, and M. Grätzel, "Structure and Energetics of Water Adsorbed at TiO_2 Anatase (101) and (001) Surfaces," *Physical Review Letters*, vol. 81, no. 14, pp. 2954–2957, 1998.

[15] G. Charlton, P. Howes, C. Nicklin, P. Steadman, J. Taylor, C. Muryn, S. Harte, J. Mercer, R. McGrath, D. Norman, T. Turner, and G. Thornton, "Relaxation of TiO_2(110)-(1×1) Using Surface X-Ray Diffraction," *Physical Review Letters*, vol. 78, no. 3, pp. 495–498, 1997.

[16] J. Mayer, U. Diebold, T. Madey, and E. Garfunkel, "Titanium and reduced titania overlayers on titanium dioxide(110)," *Journal of Electron Spectroscopy and Related Phenomena*, vol. 73, no. 1, pp. 1–11, 1995.

[17] M. Li, W. Hebenstreit, U. Diebold, A. Tyryshkin, M. Bowman, G. Dunham, and M. Henderson, "The Influence of the Bulk Reduction State on the Surface Structure and Morphology of Rutile TiO_2(110) Single Crystals," *The Journal of Physical Chemistry B*, vol. 104, pp. 4944–4950, 2000.

[18] M. Wu and P. Møller, "Studies of the electronic structure of ultrathin Cu films on a TiO_2(110) surface," *Surface Science*, vol. 224, pp. 250–264, 1989.

[19] L. Dake and R. Lad, "Electronic and chemical interactions at aluminum/TiO_2(110) interfaces," *Surface Science*, vol. 289, pp. 297–306, 1993.

[20] H. Onishi and Y. Iwasawa, "Dynamic Visualization of a Metal-Oxide-Surface/Gas-Phase Reaction: Time-Resolved Observation by Scanning Tunneling Microscopy at 800 K," *Physical Review Letters*, vol. 76, no. 5, pp. 791–794, 1996.

[21] N. Nakajima, H. Kato, T. Okazaki, and Y. Sakisaka, "Photoemission study of the modification of the electronic structure of transition-metal overlayers on TiO_2 surfaces I. Fe on TiO_2(110)," *Surface Science*, vol. 561, pp. 79–86, 2004.

[22] M. Henderson, "Mechanism for the bulk-assisted reoxidation of ion sputtered TiO_2 surfaces: diffusion of oxygen to the surface or titanium to the bulk?," *Surface Science*, vol. 343, no. 1-2, pp. L1156–L1160, 1995.

[23] M. Henderson, "A surface perspective on self-diffusion in rutile TiO_2," *Surface Science*, vol. 419, no. 2-3, pp. 174–187, 1999.

[24] K. K. K.-N.P. Kumar and A. Burggraaf, "Textural evolution and phase transformation in titania membranes: Part 1.–Unsupported membranes," *Journal of Materials Chemistry*, vol. 3, no. 11, pp. 1141–1149, 1993.

[25] J. Gallardo Amores, V. Sanchez Escribano, and G. Busca, "Anatase Crystal Growth and Phase Transformation to Rutile in High-area TiO_2, MoO_3-TiO_2 and Other TiO_2-supported Oxide Catalytic Systems," *Journal of Materials Chemistry*, vol. 5, no. 8, pp. 1245–12498, 1995.

[26] R. Wyckoff, *Crystal Structures*. Wiley Interscience Publishers, New York, 1963.

[27] A. Thomas, W. Flavell, A. Kumarasinghe, A. Mallick, D. Tsoutsou, G. Smith, S. Patel, M. Grätzel, and R. Hengerer, "Resonant photoemission of anatase TiO_2 (101) and (001) single crystals," *Physical Review B*, vol. 67, p. 035110, 2003.

[28] M. Lazzeri, A. Vittadini, and A. Selloni, "Structure and energetics of stoichiometric TiO_2 anatase surfaces," *Physical Review B*, vol. 63, no. 15, p. 155409, 2001.

[29] G. Herman, M. Sievers, and Y. Gao, "Structure Determination of the Two-Domain (1×4) Anatase TiO_2(001) Surface," *Physical Review Letter*, vol. 84, no. 15, pp. 3354–3357, 2000.

[30] W. Hebenstreit, N. Ruzycki, G. Herman, Y. Gao, and U. Diebold, "Scanning tunneling microscopy investigation of the TiO_2 anatase (101) surface," *Physical Review B*, vol. 62, no. 24, pp. R16334–R16336, 2000.

[31] M. Lazzeri, A. Vittadini, and A. Selloni, "Erratum: Structure and energetics of stoichiometric TiO_2 anatase surfaces [Physical Review B 63, 155409 (2001)]," *Physical Review B*, vol. 65, no. 11, p. 119901, 2002.

[32] R. Hengerer, B. Bolliger, M. Erbudak, and M. Grätzel, "Structure and stability of the anatase TiO_2 (101) and (001) surfaces," *Surface Science*, vol. 460, no. 1-3, pp. 162–169, 2000.

[33] H. Zhang and J. Banfield, "Thermodynamic analysis of phase stability of nanocrystalline titania," *Journal of Materials Chemistry*, vol. 8, pp. 2073–2076, 1998.

[34] P. Cox, *Transition Metal Oxides*. International Series of Monographs on Chemistry 27, Oxford University Press, New York, 1992.

[35] F. F. T. Albaret and C. Noguera, "First principles simulations of titanium oxide clusters and surfaces," *Faraday Discussions of the Chemical Society*, vol. 114, pp. 285–304, 1999.

[36] P. Hardman, G. Raikar, C. Muryn, G. van der Laan, P. Wincott, G. Thornton, D. Bullett, and P. Dale, "Valence-band structure of TiO_2 along the Γ-Δ-X and Γ-Σ-M directions," *Physical Review B*, vol. 49, no. 11, pp. 7170–7177, 1994.

[37] M. Henderson, W. Epling, C. Perkins, C. Peden, and U. Diebold, "Interaction of Molecular Oxygen with the Vacuum-Annealed TiO_2(110) Surface: Molecular and Dissociative Channels," *The Journal of Physical Chemistry B*, vol. 103, no. 25, pp. 5328–5338, 1999.

[38] R. Newnham and Y. de Haan, "Refinement of the α Al_2O_3, Ti_2O_3, V_2O_3 and Cr_2O_3 structures," *Zeitschrift für Kristallographie*, vol. 117, pp. 235–237, 1962.

[39] J. Huheey, E. Keiter, and R. Keiter, *Anorganische Chemie*. de Gruyter, 1993.

[40] Y. Dedkov, A. Vinogradov, M. Fonin, C. König, D. Vyalikh, A. Preobrajenski, S. Krasnikov, E. Kleimenov, M. Nesterov, U. Rüdiger, S. Molodtsov, and G. Güntherodt, "Correlations in the electronic structure of half-metallic ferromagnetic CrO_2 films: An x-ray absorption and resonant photoemission spectroscopy study," *Physical Review B*, vol. 72, no. 6, p. 060401, 2005.

[41] L. Chioncel, H. Allmaier, E. Arrigoni, A. Yamasaki, M. Daghofer, M. Katsnelson, and A. Lichtenstein, "Half-metallic ferromagnetism and spin polarization in CrO_2," *Physical Review B*, vol. 75, no. 14, p. 140406, 2007.

[42] W. Baur and A. Khan, "Rutile-type compounds. IV. SiO_2, GeO_2 and a comparison with other rutile-type structures," *Acta Crystallographica Section B*, vol. 27, no. 11, pp. 2133–2139, 1971.

[43] X. Liu and C. Prewitt, "High-temperature X-ray diffraction study of Co_3O_4: Transition from normal to disordered spinel," *Physics and Chemistry of Minerals*, vol. 17, no. 2, pp. 168–172, 1990.

[44] U. Diebold, J. Pan, and T. Madey, "Ultrathin metal film growth on TiO_2(110): an overview," *Surface Science*, vol. 331-333, pp. 845–854, 1995.

[45] C. Campbell, "Ultrathin metal films and particles on oxide surfaces: structural, electronic and chemisorptive properties," *Surface Science Reports*, vol. 27, pp. 1–111, 1997.

[46] P. Hardman, R. Casanova, K. Prabhakaran, C. Muryn, P. Wincott, and G. Thornton, "Electronic structure effects of potassium adsorption on TiO_2(100)," *Surface Science*, vol. 269-270, pp. 677–681, 1992.

[47] A. Grant and C. Campbell, "Cesium adsorption on TiO_2(110)," *Physical Review B*, vol. 55, no. 3, pp. 1844–1851, 1997.

[48] B. Demri, M. Hage-Ali, M. Moritz, J. Kahn, and D. Muster, "X-ray photoemission study of the calcium/titanium dioxide interface," *Applied Surface Science*, vol. 108, p. 245, 1997.

[49] Z. Li, J. H. Jørgensen, P. Møller, M. Sambi, and G. Granozzi, "A photoemission and resonant photoemission study of Ba deposition at the TiO_2 (110) surface," *Applied Surface Science*, vol. 142, pp. 135–139, 1999.

[50] S. Pétigny, B. Domenichini, H. Mostéfa-Sba, E. Lesniewska, A. Steinbrunn, and S. Bourgeois, "Molybdenum deposition on TiO_2 (110) surfaces with different stoichiometries," *Applied Surface Science*, vol. 142, no. 1-4, pp. 114–119, 1999.

[51] R. Bennett, P. Stone, and M. Bowker, "Pd nanoparticle enhanced re-oxidation of non-stoichiometric TiO_2 : STM imaging of spillover and a new form of SMSI," *Catalysis Letters*, vol. 59, p. 99, 1999.

[52] F. Pesty, H.-P. Steinrück, and T. Madey, "Thermal stability of Pt films on TiO_2(110): evidence for encapsulation," *Surface Science*, vol. 339, pp. 83–95, 1995.

[53] A. Asaduzzaman and P. Krüger, "Adsorption of 3d Transition Elements on a TiO_2(110) Surface," *The Journal of Physical Chemistry C*, vol. 112, pp. 19616–19619, 2008.

[54] J. Pan, B. Maschhoff, U. Diebold, and T. Madey, "Structural study of ultrathin metal films on TiO_2 using LEED, ARXPS and MEED," *Surface Science*, vol. 291, pp. 381–394, 1993.

[55] C. Winde, *Herstellung und Charakterisierung von Cr-Schichten auf TiO_2 (110) Oberflächen.* PhD thesis, Universität Stuttgart; Max-Planck-Institut für Metallforschung, 2002.

[56] N. Nakajima, H. Kato, T. Okazaki, and Y. Sakisaka, "Photoemission study of the modification of the electronic structure of transition-metal overlayers on TiO_2 surfaces II. Cr on TiO_2(001)," *Surface Science*, vol. 561, pp. 87–92, 2004.

[57] Y. Shao, W. Chen, E. Wold, and J. Paul, "Dispersion and electronic structure of titania-supported cobalt and cobalt oxide," *Langmuir*, vol. 10, no. 1, pp. 178–187, 1994.

[58] J. Chai, J. Pan, S. Wang, C. Huan, G. Lau, Y. Zheng, and S. Xu, "Thermal behaviour of ultra-thin Co overlayers on rutile $TiO_2(100)$ surface," *Surface Science*, vol. 589, pp. 32–41, 2005.

[59] O. Dulub, W. Hebenstreit, and U. Diebold, "Imaging Cluster Surfaces with Atomic Resolution: The Strong Metal-Support Interaction State of Pt Supported on $TiO_2(110)$," *Physical Review Letters*, vol. 84, no. 16, pp. 3646–3649, 2000.

[60] S. Tauster, S. Fung, and R. Garten, "Strong metal-support interactions. Group 8 noble metals supported on titanium dioxide," *Journal of the American Chemical Society*, vol. 100, no. 1, pp. 170–175, 2000.

[61] H. Kuzmany, *Festkörperspektroskopie.* Springer Series in Surface Sciences 25, Springer, 1989.

[62] G. Margaritondo, *Introduction to Synchrotron Radiation.* Oxford University Press, 1988.

[63] D. Coster and R. Kronig, "New type of auger effect and its influence on the x-ray spectrum," *Physica*, vol. 2, pp. 13–24, 1935.

[64] E. Kurmaev, A. Ankudinov, J. Rehr, L. Finkelstein, P. Karimov, and A. Moewes, "The L_2:L_3 intensity ratio in soft X-ray emission spectra of 3d-metals," *Journal of Electron Spectroscopy and Related Phenomena*, vol. 148, no. 1, pp. 1–4, 2005.

[65] P. Cumpson and M. Seah, "Elastic Scattering Corrections in AES and XPS. II. Estimating Attenuation Lengths and Conditions Required for their Valid Use in Overlayer/Substrate Experiments," *Surface And Interface Analysis*, vol. 25, pp. 430–446, 1997.

[66] A. Schöll, Y. Zou, T. Schmidt, R. Fink, and E. Umbach, "Energy calibration and intensity normalization in high-resolution NEXAFS spectroscopy," *Journal of Electron Spectroscopy and Related Phenomena*, vol. 129, no. 1, pp. 1–8, 2003.

[67] J. Stöhr, *NEXAFS Spectroscopy.* Springer Series in Surface Sciences 25, Springer, 1996.

[68] U. Fano, "Effects of Configuration Interaction on Intensities and Phase Shifts," *Physical Review*, vol. 124, no. 6, pp. 1866–1878, 1961.

[69] K. Prince, V. Dhanak, P. Finetti, J. Walsh, R. Davis, C. Muryn, H. Dhariwal, G. Thornton, and G. van der Laan, "2p resonant photoemission study of TiO_2," *Physical Review B*, vol. 55, pp. 9520–9523, 1997.

[70] J. Danger, H. Magnan, D. Chandesris, P. L. Fèvre, S. Bourgeois, J. Jupille, A. Verdini, R. Gotter, and A. Morgante, "Intra-atomic versus interatomic process in resonant Auger spectra at the Ti L_{23} edges in rutile," *Physical Review B*, vol. 64, p. 045110, 2001.

[71] R. Ruus, A. Saar, J. Aark, A. Aidla, T. Uustare, and A. Kikas, "Resonant auger spectra of TiO_2 at Ti2p and O1s absorption edges," *Journal of Electron Spectroscopy and Related Phenomena*, vol. 93, pp. 193–199, 1998.

[72] P. L. Fèvre, J. Danger, H. Magnan, D. Chandesris, J. Jupille, S. Bourgeois, M.-A. Arrio, R. Gotter, A. Verdini, and A. Morgante, "Stoichiometry-related Auger lineshapes in titanium oxides: Influence of valence-band profile and of Coster-Kronig processes," *Physical Review B*, vol. 69, no. 15, p. 155421, 2004.

[73] A. Thomas, W. Flavell, A. Mallick, A. Kumarasinghe, D. Tsoutsou, N. Khan, C. Chatwin, S. Rayner, G. Smith, R. Stockbauer, S. Warren, T. Johal, S. Patel, D. Holland, A. Taleb, and F. Wiame, "Comparison of the electronic structure of anatase and rutile TiO_2 single-crystal surfaces using resonant photoemission and x-ray absorption spectroscopy," *Physical Review B*, vol. 75, no. 3, p. 035105, 2007.

[74] J. Nerlov, Q. Gel, and P. Møller, "Resonant photoemission from TiO_2(110) surfaces: implications on surface bonding and hybridization," *Surface Science*, vol. 348, pp. 28–38, 1996.

[75] R. Heise, R. Courths, and S. Witzel, "Valence band densities-of-states of TiO_2(110) from resonant photoemission and photoelectron diffraction," *Solid State Communications*, vol. 84, no. 6, pp. 599–602, 1992.

[76] Z. Zhang, S.-P. Jeng, and V. Henrich, "Cation-ligand hybridization for stoichiometric and reduced TiO_2 (110) surfaces determined by resonant photoemission," *Physical Review B*, vol. 43, p. 12004, 1991.

[77] K. Smith and V. Henrich, "Resonant photoemission in Ti_2O_3 and V_2O_3: Hybridization and localization of cation 3d orbitals," *Physical Review B*, vol. 38, no. 14, p. 9571, 1988.

[78] E. Bertel, R. Stockbauer, and T. Madey, "Resonant electron emission in Ti and TiO_2," *Physical Review B*, vol. 27, no. 3, pp. 1939–1942, 1983.

[79] T. Kaurila and J. Väyrynen, "Resonant photoemission of titanium," *Journal of Electron Spectroscopy and Related Phenomena*, vol. 82, pp. 165–172, 1996.

[80] R. Cowan, *The Theory of Atomic Structure and Spectra*. Los Alamos Series in Basic and Applied Sciences 3, University of California Press, 1981.

[81] F. de Groot and A. Kotani, *Core Level Spectroscopy of Solids*. Advances in Condensed Matter Science, Taylor & Francis CRC press, 2008.

[82] F. de Groot, J. Fuggle, B. Thole, and G. Sawatzky, "2p x-ray absorption of 3d transition-metal compounds: An atomic multiplet description including the crystal field," *Physical Review B*, vol. 42, no. 9, pp. 5459–5468, 1990.

[83] F. de Groot, "X-ray absorption of transition metal oxides: An overview of the theoretical approaches," *Journal of Electron Spectroscopy and Related Phenomena*, vol. 62, no. 1–2, pp. 111–130, 1993.

[84] F. de Groot, "X-ray absorption and dichroism of transition metals and their compounds," *Journal of Electron Spectroscopy and Related Phenomena*, vol. 67, no. 4, pp. 529–622, 1994.

[85] F. de Groot, "Multiplet effects in X-ray spectroscopy," *Coordination Chemistry Reviews*, vol. 249, no. 1-2, pp. 31–63, 2005.

[86] J. Chen, "NEXAFS investigations of transition metal oxides, nitrides, carbides, sulfides and other interstitial compounds," *Surface Science Reports*, vol. 30, no. 1-3, pp. 1–152, 1997.

[87] A. Taverner, P. Hollamby, P. Aldridge, R. Egdell, and W. Mackrodt, "An inverse photoemission study of empty electronic states in TiO_2," *Surface Science*, vol. 287-288, pp. 653–657, 1993.

[88] J. Woicik, E. Nelson, L. Kronik, M. Jain, J. Chelikowsky, D. Heskett, L. Berman, and G. Herman, "Hybridization and Bond-Orbital Components in Site-Specific X-Ray Photoelectron Spectra of Rutile TiO_2," *Physical Review Letters*, vol. 89, no. 7, p. 077401, 2002.

[89] U. Diebold, H.-S. Tao, N. Shinn, and T. Madey, "Electronic structure of ultrathin Fe films on TiO_2(110) studied with soft-x-ray photoelectron spectroscopy and resonant photoemission," *Physical Review B*, vol. 50, no. 19, pp. 14474–14480, 1994.

[90] P. M. Kumar, S. Badrinarayanan, and M. Sastry, "Nanocrystalline TiO_2 studied by optical, FTIR and X-ray photoelectron spectroscopy: correlation to presence of surface states," *Thin Solid Films*, vol. 358, no. 1-2, pp. 122–130, 2000.

[91] E. L. Bullock, L. Patthey, and S. G. Steinemann, "Clean and hydroxylated rutile TiO_2(110) surfaces studied by X-ray photoelectron spectroscopy," *Surface Science*, vol. 352-354, pp. 504–510, 1996. Proceedings of the 15th European Conference on Surface Science.

[92] H. Perron, J. Vandenborre, C. Domain, R. Drot, J. Roques, E. Simoni, J.-J. Ehrhardt, and H. Catalette, "Combined investigation of water sorption on TiO_2 rutile (110) single crystal face: XPS vs. periodic DFT," *Surface Science*, vol. 601, no. 2, pp. 518–527, 2007.

[93] G. Hopfengärtner, D. Borgmann, I. Rademacher, G. Wedler, E. Hums, and G. Spitznagel, "XPS studies of oxidic model catalysts: Internal standards and oxidation numbers," *Journal of Electron Spectroscopy and Related Phenomena*, vol. 63, no. 2, pp. 91–116, 1993.

[94] M. Oku, K. Wagatsuma, and S. Kohiki, "Ti 2p and Ti 3p X-ray photoelectron spectra for TiO_2, $SrTiO_3$ and $BaTiO_3$," *Physical Chemistry Chemical Physics*, vol. 1, p. 5327, 1999.

[95] L. Fleming, C. Fulton, G. Lucovsky, J. Rowe, M. Ulrich, and J. Lüning, "Local bonding analysis of the valence and conduction band features of TiO_2," *Journal of Applied Physics*, vol. 102, p. 033707, 2007.

[96] M. Batzill, E. Morales, and U. Diebold, "Influence of Nitrogen Doping on the Defect Formation and Surface Properties of TiO_2 Rutile and Anatase," *Physical Review Letters*, vol. 96, no. 2, p. 026103, 2006.

[97] J. Richter, A. Henningsson, B. Sanyal, P. Karlsson, M. Andersson, P. Uvdal, H. Siegbahn, O. Eriksson, and A. Sandell, "Phase separation and charge localization in UHV-lithiated anatase TiO_2 nanoparticles," *Physical Review B*, vol. 71, no. 23, p. 235419, 2005.

[98] R. Brydson, H. Sauer, W. Engel, J. Thomas, E. Zeitler, N. Kosugi, and H. Kuroda, "Electron energy loss and x-ray absorption spectroscopy of rutile and anatase: a test of structural sensitivity," *Journal of Physics: Condensed Matter*, vol. 1, p. 797, 1989.

[99] R. Ruus, A. Kikas, A. Saar, A. Ausmees, E. Nõmmiste, J. Aarik, A. Aidla, T. Uustare, and I. Martinson, "Ti 2p and O 1s X-ray absorption of TiO_2 polymorphs," *Solid State Communications*, vol. 104, no. 4, pp. 199–203, 1997.

[100] Z. Wu, G. Ouvrard, P. Gressier, and C. Natoli, "Ti and O K edges for titanium oxides by multiple scattering calculations: Comparison to XAS and EELS spectra," *Physical Review B*, vol. 55, pp. 10382–10391, 1997.

[101] J. Yeh and I. Lindau, "Atomic subshell photoionization cross sections and asymmetry parameters: $1 \leq Z \leq 103$," *Atomic Data and Nuclear Data Tables*, vol. 32, no. 1, pp. 1 – 155, 1985.

[102] O. Seifarth, *Properties of Chromium, Cobalt and Nickel Nanoparticels embedded into ordered Block Copolymers and Conducting Polymers.* PhD thesis, BTU Cottbus, 2006.

[103] C. Stagarescu, X. Su, D. Eastman, K. Altmann, F. Himpsel, and A. Gupta, "Orbital character of O-2p unoccupied states near the Fermi level in CrO_2," *Physical Review B*, vol. 61, pp. R9233–R9236, 2000.

[104] N. Hollmann, Z. Hu, M. Valldor, A. Maignan, A. Tanaka, H. H. Hsieh, H.-J. Lin, C. T. Chen, and L. H. Tjeng, "Electronic and magnetic properties of the kagome systems $YBaCo_4O_7$ and $YBaCo_3MO_7$ (M = Al, Fe)," *Physical Review B*, vol. 80, no. 8, p. 085111, 2009.

[105] M. Hugenschmidt, L. Gamble, and C. Campbell, "The interaction of H_2O with a $TiO_2(110)$ surface," *Surface Science*, vol. 302, pp. 329–340, 1994.

[106] J. Barth, F. Gerken, and C. Kunz, "Experimental study of the 3p-3d intershell interaction in Ca, Sc, Ti, V, and Cr metals," *Physical Review B*, vol. 31, p. 2022, 1985.

[107] K. Okada and A. Kotani, "Theory of core level X-ray photoemission and photoabsorption in Ti compounds," *Journal of Electron Spectroscopy and Related Phenomena*, vol. 62, p. 131, 1993.

[108] U. Diebold, J. Pan, and T. Madey, "Ultrathin metal films on $TiO_2(110)$: metal overlayer spreading and surface reactivity," *Surface Science*, vol. 287-288, pp. 896–900, 1993.

[109] N. McIntyre and M. Cook, "X-ray photoelectron studies on some oxides and hydroxides of cobalt, nickel, and copper," *Analytical Chemistry*, vol. 47, no. 13, pp. 2208–2213, 1975.

[110] T. Barr, "An ESCA study of the termination of the passivation of elemental metals," *The Journal of Physical Chemistry*, vol. 82, no. 16, pp. 1801–1810, 1978.

[111] B. Tan, K. Klabunde, and P. Sherwood, "XPS studies of solvated metal atom dispersed (SMAD) catalysts. Evidence for layered cobalt-manganese particles on alumina and silica," *Journal of the American Chemical Society*, vol. 113, no. 3, pp. 855–861, 1991.

List of abbreviations

CIS	Constant Initial State
(s)CK	(super)-Coster-Kronig
CT	Charge Transfer
CTM	Charge Transfer Multiplet
D_{4h}	Tetragonal Symmetry
DFT	Density Functional Theory
EELS	Electron Energy Loss Spectroscopy
HIKE XPS	High Kinetic Energy XPS
LEED	Low Energy Electron Diffraction
LEIS	Low Energy Ion Scattering
ML	Monolayer
O_h	Octahedral Symmetry
(p)DOS	(partial) Density of States
PES	Photoelectron (or Photoemission) Spectroscopy
PIX	Photo-ionization Cross-Section
ResPES	Resonant Photoelectron (or Photoemission) Spectroscopy
SMSI	Strong Metal Support Interaction
SO_3	Spherical Symmetry
SR-PES	Synchrotron Radiation Photoelectron (or Photoemission) Spectroscopy
STM	Scanning Tunnelling Microscopy
STS	Scanning Tunnelling Spectroscopy
T_d	Tetrahedral Symmetry
TEM	Transmission Electron Microscopy
TEY	Total Electron Yield
U_{dd}	Coulomb Repulsion between d electrons
U_{pd}	Coulomb Attraction between core hole and d electrons i.e. core hole potential
UPS	Ultraviolet Photoelectron Spectroscopy
VBM	Valence Band Maximum
XAS	X-ray Absorption Spectroscopy
XES	X-ray Emission Spectroscopy

XLD	X-ray Linear Dichroism
XPS	X-ray Photoelectron Spectroscopy
XRD	X-ray Diffraction

Publications and conference contributions of the author related to this thesis

Own publications

S. Müller, G. Seibold, and D. Schmeißer, "Preparation and Characterization of TiO_2 thin films and Cr and Co doped TiO_2 thin films," in H.T. Vierhaus (Eds.): *Computer Science Reports 03/07: DEDIS NANO DAYS*, pp. 7–11, BTU Cottbus (2007), ISSN: 1437-7969

S. Müller and D. Schmeißer, "Properties of Cr deposited on TiO_2 thin films," *BESSY Annual Report 2007*, pp. 433–434

S. Müller and D. Schmeißer, "CT states in TiO_2," *BESSY annual report 2008*, in press

Conference contributions

S. Müller and D. Schmeißer, "The initial stages of Chromium growth on Titanium Dioxide – Investigations using synchrotron radiation," Talk O 33.8, DPG Spring Meeting 2007, Regensburg, Germany

S. Müller and D. Schmeißer, "Cr adsorption on TiO_2 surfaces," Poster ID 166, VUV XV, 2007, Berlin, Germany

S. Müller and D. Schmeißer, "Direct Observation of d^2L^2 Charge Transfer States in TiO_2 thin films by Resonant Photoelectron Spectroscopy," Talk O 32.3, DPG Spring Meeting 2008, Berlin, Germany

S. Müller and D. Schmeißer, "Deposition of reactive and non-reactive metals on titanium dioxide – chromium and cobalt," Talk, 2008 International Students and Young Scientists Workshop "Photonics and Microsystems", Wrocław and Szklarska Poręba, Poland

S. Müller and D. Schmeißer, "The initial stage of Cobalt deposition on TiO_2," Poster SR-P5, ECOSS 25, 2008, Liverpool, United Kingdom

S. Müller and D. Schmeißer, "Investigation of ultra-thin Chromium layers on Titanium Dioxide by resonant photoemission," Talk O 3.5, DPG Spring Meeting 2009, Dresden, Germany

S. Müller and D. Schmeißer, "Synchrotron radiation spectroscopy studies of ultrathin chromium films on titanium dioxide," Talk Session "Measurement Technology", 2009 International Students and Young Scientists Workshop "Photonics and Microsystems", Wernigerode, Germany

Publications (collaborations)

O. Seifarth, J. Dabrowski, P. Zaumseil, S. Müller, D. Schmeißer, H.-J. Müssig, T. Schroeder, "On the band gaps and electronic structure of thin single crystalline praseodymium oxide layers on Si(111)," *Journal of Vacuum Science and Technology B*, vol. 27, no. 1, pp. 271–276, 2009

J. Domaradzki, D. Kaczmarek, A. Borkowska, D. Schmeißer, S. Müller, R. Wasielewski, A. Ciszewski, D. Wojcieszak, "Influence of annealing on the structure and stoichiometry of europium-doped titanium dioxide thin films," *Vacuum*, vol. 82, pp. 1007–1012

Curriculum Vitae

since June 2007	Ph.D. student in BTU Cottbus International Graduate School
February 2007 to May 2007	Scientific Assistant and Ph.D. student, Chair of Applied Physics, BTU
April 2006 to January 2007	Diplom Student, Chair of Applied Physics, BTU Cottbus
September 2005 to February 2006	Internship at Robert Bosch GmbH, GS/ENA4, Stuttgart, Laser-assisted ignition in combustion engines
October 2001 to January 2007	Regular study course of Physics, BTU Cottbus, finished with the degree of Diplom-Physiker
July 2000 to April 2001	Military Service
June 2000	Abitur at "Carl-Anwandter-Gymnasium" in Calau

Acknowledgement

I would like to express my gratefulness to Prof. Dieter Schmeißer, who supervised my work. I benefited from small and big advices, frequent discussions and useful hints that pushed me from time to time into the proper direction.
Additionally, I want to thank Prof. Christian Pettenkofer and Prof. Andreas Klein for their readiness to act as referees.
In the early stage, I also benefited very much from useful hints given to me by Dr. Olaf Seifarth and Dr. Patrick Hoffmann, who also gave excellent support at the beamline at BESSY II.
I thank Dr. Massimo Tallarida for his support, as well as the frequent discussion at and around the beamline.
I thank my colleagues Marcel Michling, Daniel Friedrich, Matthias Richter and Stephan Schmidt for providing a nice working atmosphere in Cottbus and at BESSY. The frequent discussions about a broad range of topics also made some long trip to BESSY and back a little bit shorter.
Thanks to Karla Kersten and Susanne Masch for their support with administrative affairs.
Thanks also to Guido Beuckert for his technical support.
I also acknowledge the nice working atmosphere provided by the members of our group: Karsten Henkel, Konstantin Karavaev, Jolanta Klocek, Krzysztof Andrzej Kolanek, Matthias Kraatz, Klaus Müller, Ioanna Paloumpa, Carola Schwiertz, Krzysztof Kachel, Shine Philip, Łukasz Starzyk, Jakub Wyrodek, Marcus Herlitschke, Matthias Städter, and of course the people I already mentioned.
I thank the BTU International Graduate School for the financial support.

I am very grateful for the support I received from my parents during the last years. Without this, my studies in Cottbus would not have been possible in such a way.

Special Thanks also goes to Żaneta. She knows why.

Erklärung

Hiermit versichere ich, dass ich die vorliegende Arbeit selbständig und ohne unerlaubte Hilfsmittel angefertigt habe. Alle verwendeten Quellen habe ich angegeben.

Cottbus, Dezember 2009